

Inclusion of Dynamical Effects in Calculation of EPR Parameters

Dissertation zur Erlangung des naturwissenschaftlichen Doktorgrades der
Julius-Maximilians Universität Würzburg

vorgelegt von
James Asher
aus Bath

Würzburg 2006

Eingereicht am:

bei der Fakultät für Chemie und Pharmazie

1. Gutachter:

2. Gutachter:

1. Prüfer:

2. Prüfer:

3. Prüfer:

des Öffentlichen Promotionskolloquiums

Tag des Öffentlichen Promotionskolloquiums:

Doktorurkunde ausgehändigt am:

Acknowledgements

This thesis owes most to Martin Kaupp, my doctoral supervisor, for his guidance, teaching of all matters quantum chemical, and provision of highly interesting research for me to do. Thankyou Martin for being generally helpful, patient and a pretty cool boss.

I thank the members of our research group, past and present: Michal Straka, Hilke Bahmann, Christian Remenyi, Alexander Patrakov, Seb Riedel, Sylwia Kacprzak, Alexei Arbuznikov, Sandra Schinzel, Roman Reviakin, Irina Malkin and Ilaria Ciofini; and also the guests our workgroup regularly entertains: Vladimir and Olga Malkin, Kathrin Götz and J-C. Tremblay. I thank you for discussions, technical assistance, correction of my german, friendship, games of chess, and the numerous cakes that have passed through our coffee room over the years.

For similar reasons of assistance and bakery products I thank also our neighbours, Carsten Strohmann and his group - Daniel Schildbach, Dominic Auer, Katja Strohfeldt and Jan Hörnig.

I thank Dominik Marx and his group for the several instructive weeks I spent learning about CP-MD with them. I thank Nikos Doltsinis especially for instruction and guidance in the ways of Molecular Dynamics.

I gratefully acknowledge funding received from the DFG-sponsored Graduate College "Electron Density: Theory and Experiment"; and the generous budget provided by the Leibniz Rechenzentrum (LRZ), München, for running MD simulations on their SR-8000 supercomputer (project code: h0731).

Finally, I thank my family and friends - my parents, my brother, Mathew Sebastian, Tom Calver and Marinella Berova - for support, advice and occasional whiskey.

Contents

1	Introduction	9
1.1	Theoretical calculation of EPR parameters	9
1.2	Approximate dynamical corrections	10
1.3	Explicit treatment of dynamics	11
1.4	Objectives of this work	11
2	Theoretical background	13
2.1	Density Functional Theory	13
2.1.1	Density-only approaches	14
2.1.2	Kohn-Sham theory	14
2.1.3	Exchange and correlation in Kohn-Sham	15
2.1.4	DFT vs. wavefunction methods	16
2.2	g -Tensor calculation	17
2.3	Hyperfine coupling calculation	18
2.4	Molecular Dynamics	19
2.4.1	Periodic boundaries and basis sets	21
2.4.2	Temperature control	22
3	Silasesquioxane-trapped H Atoms	25
3.1	Introduction	25
3.1.1	Importance of Silasesquioxanes	25
3.1.2	Trapped atoms	26
3.2	Computational Details	27
3.3	Results	28
3.3.1	g -Tensors: Theory vs. Experiment	28
3.3.2	HFCs and Dynamical Effects	29
3.3.3	Atomic contributions to g -shifts	31
3.3.4	Spin density and g -values	32
3.3.5	Excitation analysis of $\Delta g_{SO/OZ}$	33
3.3.6	Parameter Dependence on DFT Functional	36

4	Benzosemiquinone Molecular Dynamics	41
4.1	Importance of Benzosemiquinones	41
4.2	Computational Details	42
4.2.1	Molecular Dynamics	42
4.2.2	Solvation Analysis	43
4.3	H-Bonding Analysis	44
4.3.1	H-Bonding to carbonyl	44
4.3.2	T-stacked H-Bonding	50
4.3.3	Geometrical Properties	51
4.3.4	Reliability of the MD simulations: Caveats	55
5	Dynamical EPR Parameters of Benzosemiquinone	59
5.1	Semiquinone EPR	59
5.1.1	Theoretical analysis of semiquinone EPR	59
5.2	Computational Details	62
5.3	g -Tensor calculations	64
5.3.1	The effect of the C-O bond length	66
5.3.2	On the z component	69
5.4	Hyperfine Coupling	71
5.4.1	Solvation effects on HFCs	74
5.4.2	HFCs and H-bond configurations	75
5.4.3	Structural solvation effects	76
5.4.4	Tensor axes and orientation	78
5.4.5	Comparison with experiment and static calculations	78
5.4.6	Solvent proton HFCs	81
5.5	Further work	86
6	Ubisemiquinone Molecular Dynamics	89
6.1	On Ubisemiquinone	89
6.2	Computational details	90
6.3	Hydrogen bonding	91
6.3.1	H-bonds to oxygen	91
6.3.2	H-bonds to carbon	95
6.3.3	H-bond directionality	96
6.4	Geometry	98
6.4.1	Conformation	98
6.4.2	Bond lengths and angles	101
6.5	Further simulation	102

7	Dynamical EPR Parameters of Ubisemiquinone	103
7.1	Introduction	103
7.2	Computational details	103
7.3	g -Tensor calculations	104
7.3.1	Comparison with other studies	107
7.4	HFC calculations	109
7.4.1	Side-chain HFCs	111
7.4.2	Solvent HFCs	114
7.5	Further Work	116
8	Summary	117
9	Zusammenfassung	123
	Bibliography	128
	Curriculum Vitae	137
	List of Publications	139

Chapter 1

Introduction

1.1 Theoretical calculation of EPR parameters

Electronic Paramagnetic Resonance (EPR)^a is a branch of Magnetic Resonance (MR) spectroscopy concerned with transitions between electronic spin states. EPR is a standard technique for investigating paramagnetic species in any branch of science, with applications ranging from detecting the presence of radicals in cigarette smoke¹ to investigating the catalytic mechanisms of a metalloenzyme.²

The two spin states, α and β , of an unpaired electron are degenerate in the absence of a magnetic field. When a magnetic field is applied, the interaction of the field with the magnetic moment of the electron induces an energy difference proportional to the field strength. This is called the electronic Zeeman interaction, and is parameterised by the electronic g -tensor. Additional structure in EPR spectra appears from "hyperfine" interactions between the electronic and nuclear spins, parameterised by the hyperfine coupling (HFC) tensor. HFCs serve as a useful indicator of the spin density distribution of a molecule: in the non-relativistic limit, the isotropic component is proportional to the spin density at the nucleus, and the anisotropic contribution represents dipolar interaction between the nuclear spin and the delocalised spin density. For paramagnetic systems of spin multiplicity greater than 2, i.e. with more than one unpaired electron, additional structure appears due to nondegeneracy of different spin states even in the absence of magnetic field; this is called Zero Field Splitting, or ZFS. This thesis is concerned only with doublet species, and so ZFS will not be further discussed; theoretical

^aAlso termed Electron Spin Resonance, or ESR.

approaches to HFCs and the electronic g -tensor will be discussed in Chapter 2.

Computational chemistry is increasingly being used to calculate these parameters, as well as those important in Nuclear Magnetic Resonance (NMR) spectroscopy (which concerns itself with nuclear spin transitions). In cases where a particular species has not been well characterised, or signals cannot be easily assigned, simulation of the MR parameters can be very useful in interpreting the spectrum. It is not uncommon to see experimental EPR papers presenting computational data as an interpretational tool for this reason. *In silico* calculations also allow thorough, systematic investigation of how MR parameters vary with conformational and environmental effects. (See ref. 3 for a thorough overview of MR parameter calculation.)

Usually when spectroscopic parameters (or, indeed, most properties of chemical interest) are computed for a system, the assumption is made that nuclear motion is unimportant. The properties are usually calculated from a single static structure - or a set of structures, compared to determine the effects of certain factors - which are derived from computational optimisation to the lowest-energy structure. (Experimental, e.g. x-ray crystallographic, structures can also be used if available.) This approach is necessarily an approximation, and amounts to calculating the properties of the system at absolute zero; solvent/solute interactions are treated as if the solvent molecules sit, frozen, at the minimum of the local potential well. But the system of interest is normally studied at higher temperatures, where vibrational, conformational and intermolecular motion cause continuous distortion from the equilibrium geometry. In liquids, the presence of solvent molecules at positions other than the energy minima, rotation of molecules, transition between solvation shells, and formation and breaking of hydrogen bonds, are all ignored in the static *ansatz*. In many cases, this approximation is not a drastic one, and important insights can generally be obtained from static calculations. However, there are cases where dynamical effects are important and need to be considered in the calculations.

1.2 Approximate dynamical corrections

In many paramagnetic systems, EPR parameters are heavily dependent on one structural parameter in particular. A rough indication of the dynamical effects can thus be gotten from determining how dynamics affect the mean value of this parameter (usually increasing it, in the case of bond lengths), and what the average (RMS) displacement from that mean is. This can be done by using empirical structural parameters in the calculation, instead of

calculating them *ab initio*. (This can also correct for other deficiencies in the calculation, such as lack of a solvation sphere or deficiencies in the *ab initio* generation of structural parameters.) Alternatively, such corrections can be done by mapping out the potential energy well of the structural parameter by a series of constrained optimisations. On this basis one can model dynamical corrections to the structural parameter(s) at a given temperature by, e.g., fitting a Simple Harmonic Oscillator (SHO) model.

1.3 Explicit treatment of dynamics

The most accurate manner of accounting for dynamics is to model them explicitly, taking the system of interest and calculating its motion iteratively over a series of small increments in time. When done within the Born-Oppenheimer (BO) approximation, i.e. assuming point-like classical nuclei, this is called molecular dynamics (MD).^b By allowing free motion of all atoms, the dynamical effects of all degrees of freedom can be included and analysed - although isolating the effects of different structural parameters is no longer as straightforward. Furthermore, property calculations can either be performed on an average structure calculated from the simulated trajectory, or be performed repeatedly on different snapshots and averaged. Unfortunately, MD is computationally expensive at the *ab initio* level; while at the empirical molecular mechanics (MM) level, it is incapable of dealing with bond breaking or formation, or of any interaction not explicitly anticipated and parameterised. MD will be further discussed in Chapter 2.

1.4 Objectives of this work

In this thesis I present computational studies of the EPR parameters of for certain paramagnetic systems in which dynamical effects are significant. In Chapter 3 we look at silasesquioxane-trapped hydrogen atoms and their anomalously positive g -shifts. In this system, the most important degrees of freedom are those of the trapped hydrogen atom, which vibrates within the potential well in the centre of the cage. Hence the effects of thermal motion on g -tensors and ^1H hyperfine coupling constants could be modelled reasonably well by applying an SHO model to the hydrogen atom motion to derive corrections to the EPR parameters.

^bFor most chemical purposes, the BO approximation of classical nuclei gives good enough dynamics. Quantum nuclear dynamics is possible, but more involved.

In Chapters 4-7 I look at semiquinone radical anions, an important class of bioradicals. The g -tensors and HFCs of these species are heavily dependent on not only structural parameters but also the intramolecular environment. The dynamics in such a system would be highly complex, and hence not reducible to simple, *ad hoc* dynamical corrections - especially the dynamics of the solvation sphere, which are of great interest. Therefore we opted to use *ab initio* molecular dynamics to model the prototypical benzosemiquinone (Chapters 4 and 5) and the ubiquitous, and biologically very important, ubisemiquinone (Chapters 6 and 7) in aqueous solution, and to calculate EPR parameters from the MD trajectory. MD has previously found application in calculating and giving insight into the HFCs of nitrosyl^{4,5} and methyl radicals.^{6,7} Our MD studies, however, represent the first attempt to apply MD to the calculation of g -tensors. In Chapter 8, I summarise the results of our work.

Chapter 2

Theoretical background

In this chapter, we present a short summary of the fundamental principles behind the computational techniques used in this thesis: density functional theory (DFT), quantum mechanical calculation of EPR parameters, and Car-Parrinello molecular dynamics (CP-MD). Necessarily this is only a very brief overview aimed at those readers who are unfamiliar with the topics. DFT is treated extensively in the books on the subject by Parr and Yang⁸ and Koch and Holthausen,⁹ and most quantum chemical textbooks have a chapter devoted to it. For comprehensive coverage of the calculation of EPR parameters, we recommend the recent book by Kaupp, Bühl and Malkin³ (see particularly Part D). For molecular dynamics we direct the reader to the book of Allen and Tildesley,¹⁰ and a detailed treatment of *ab initio* molecular dynamics is provided by Marx and Hutter in ref. 11.

2.1 Density Functional Theory

Density functional theory, or DFT, is an alternative method to wavefunction-based approaches, such as Hartree-Fock (HF) and configuration interaction (CI), for calculating the electronic structure of a system. It is based on the theorems of Hohenberg and Kohn, who proved that the electrons of a system feel an external potential that is uniquely determined by the electron density (to within addition of a constant).¹² This implies the existence of some functional which maps the energy to the density. If this functional were known exactly, it could be used in place of the operator-based formalism of wavefunction-based approaches to calculate the electronic structure. Unfortunately, the exact universal functional is not known, but several approximations to it exist.

2.1.1 Density-only approaches

Given that the potential is a functional of the density and not of the wavefunction, it should not matter whether the wavefunction is composed of a single determinant or many (with the exception of broken-symmetry multiplet states, where multiple determinants are necessary to describe the spin properties), or whether a wavefunction is involved at all. Thomas-Fermi (TF) theory, the earliest approach to DFT (predating the work of Hohenberg and Kohn), worked with the electron density as the sole variable and contained no reference to the electronic wavefunction.^{13,14} Unfortunately, the approximations needed to construct the energy functional in TF were somewhat drastic, particularly regarding kinetic energy; the results included describing molecules as higher in energy than the separated atoms.¹⁵ More sophisticated functionals have been developed on the TF basis, but still have quite severe accuracy problems. (See chapter 6 of ref. 8 for an overview.)

2.1.2 Kohn-Sham theory

Kohn-Sham (KS) theory¹⁶ is an alternative approach that explicitly constructs the electron density from a single-determinantal wavefunction. The orbitals of the KS wavefunction are optimised within the external potential provided by the total electron density, without direct reference to each other. Unlike in HF (or post-HF methods), where the electron-electron interaction is treated by operators that relate the orbitals to each other directly, the interaction is indirect: the electrons move in a common potential that derives from the total electron density. For this reason the KS wavefunction is formally referred to as that of a *non-interacting reference system*: it is not the real wavefunction, but a model - intended merely to give the same electron density as the real system, and therefore the same energy under application of the universal functional.

The energy of the system may be described as the sum of two parts: kinetic (T) and potential (U) energy:

$$E[\rho] = T[\rho] + U[\rho] \quad (2.1)$$

KS theory splits the kinetic energy into two terms: the kinetic energy of a system of non-interacting electrons, and a correction for the fact that the electrons do interact. The potential energy may be divided into electron-nuclear (U_{Ne}) and electron-electron (U_{ee}) terms:

$$E_{KS}[\rho] = T_s[\rho] + \Delta T[\rho] + U_{Ne}[\rho] + U_{ee}[\rho] \quad (2.2)$$

The motivation for expressing the kinetic energy term thus is that no way of determining the exact kinetic energy from the density is known. However, the non-interacting kinetic energy term T_s of a given density can be calculated as follows: generate a single-determinantal wavefunction that fits the electron density exactly, and apply the quantum mechanical kinetic energy operator. As the KS method constructs the density from a single determinant in the first place, this part of the functional is easy to compute exactly. The ease of calculating the kinetic energy is one of the chief advantages of KS theory.

U_{Ne} may be expressed exactly as the electrostatic attraction energy V_{Ne} between nuclei and electrons. The electron-electron interaction energy U_{ee} is entirely electrostatic, and may be split into the classical self-repulsion of the electron cloud V_{ee} and a correction, V_{XC} , the exchange-correlation energy. The former may be calculated exactly, while the latter cannot.

$$E_{KS}[\rho] = T_s[\rho] + \Delta T[\rho] + V_{Ne}[\rho] + V_{ee}[\rho] + V_{XC}[\rho] \quad (2.3)$$

The functional now consists of three exactly-known terms, T_s , V_{Ne} and V_{ee} , and two inexact terms, ΔT and V_{XC} . ΔT is folded into V_{XC} , which is collectively termed the "exchange-correlation functional".

2.1.3 Exchange and correlation in Kohn-Sham

The principal job of the exchange-correlation functional is as a correction to the electrostatic electron/electron energy. The exact V_{ee} term treats the electron density as a diffuse cloud of negative charge. However, the electrons are discrete particles, and the density represents the probability of one electron being present at a particular location at any instant. The effects of this are as follows.

- A diffuse cloud of negative charge feels at each (infinitesimally small) point in space repulsion from the whole of the rest of the cloud, which contains N electrons' worth of negative charge. However, as a particle at a particular point in space, the electron feels repulsion not from N electrons, but from $(N - 1)$. V_{ee} thus contains an unphysical self-interaction of the electron repelling itself, which must be corrected for.
- As fermions, electrons of the same spin have a tendency to avoid one another. This is called fermi correlation, or exchange interaction, and leads to a decrease in electron-electron repulsion.
- The instantaneous positions of electrons are also correlated to avoid each other due to Coulomb repulsion. This is called Coulomb correlation, and likewise leads to a decrease in electron-electron repulsion, called the correlation energy.

The exchange-correlation functional is for convenience usually divided into exchange and correlation parts, which can be combined as desired (the combined functional is then simply termed XC , where X is the exchange and C the correlation functional: e.g. BLYP, which combines the B¹⁷ and LYP¹⁸ functionals). The exchange functional includes fermionic correlation and the self-interaction correction, and is an interaction solely between electrons of the same spin. The correlation functional handles Coulomb correlation. If the functional is constructed with reference to the exchange-correlation hole (the difference between the average density and the instantaneous density seen by an electron located at a particular point), it can be shown that it includes ΔT implicitly. (See section 8.5 of ref. 8.) A variety of exchange-correlation functionals exist, with the simplest being derived from the homogenous electron gas, termed LDA (local density approximation) functionals. These depend purely on the electron density, and the SVWN parameterisation^{19,20} is the most commonly used. More complex functionals depend also on derivatives of the electron density; these are termed GGA (generalised gradient approximation) functionals. Commonly used GGA functionals include the Becke (B)¹⁷ exchange and LYP,¹⁸ P86²¹ and PW91²² correlation functionals. More recent "meta-GGA" approaches include the kinetic energy density as well, for instance in the PKZB functional.^{23,24} One popular approach is that of hybrid functionals, which mix DFT exchange with "exact" Hartree-Fock exchange; examples are the B3²⁵ and BH²⁶ functionals.

As in Hartree-Fock, an analytical solution for the ground state of a system is not available in Kohn-Sham DFT, and hence the electronic structure must be optimised in a self-consistent field (SCF) approach. The orbitals of the wavefunction are constructed using a finite basis set (typically of gaussian functions), and the electron density is calculated from them. The orbitals are then optimised within the potential provided by the electron density; the electron density and potential are then recalculated, and the orbitals reoptimised; and so forth, until from iteration to iteration the orbitals do not change (above a certain threshold). Unlike Hartree-Fock, not all integrals involved are analytically solvable; for some functionals, it is necessary to construct a grid and perform numerical integration.

2.1.4 DFT vs. wavefunction methods

Kohn-Sham DFT is widely used in quantum chemistry and solid-state physics, as its computational cost is comparable to or lower than Hartree-Fock, the simplest *ab initio* wave-mechanics method. Unlike Hartree-Fock, however, it includes correlation effects, which, in wavefunction-based methods, need considerably more expensive treatments to deal with. However, HF and mul-

tideterminantal methods have an obvious hierarchy: the results may in principle be improved indefinitely, by addition of more and more determinants to the wavefunction. If a given DFT functional displays poor performance, however, one cannot simply choose a "better" functional instead - there's no such thing. Some functionals may have more complexity and less severe approximations in their derivation; but the simplest, LDA, sometimes outperforms its more sophisticated brethren. DFT functionals can be judged only by the quality of their performance, which varies according to the property and the system under investigation. Hence, high-level configuration interaction (CI) and coupled cluster (CC) calculations remain necessary as a benchmark by which to judge both DFT and less complex wavefunction-based methods.

2.2 *g*-Tensor calculation

The electronic *g*-tensor is calculated in a perturbation-theoretical manner. This work uses a one-component uncoupled density functional method, in which the *g*-tensor is a 2nd-order property, with magnetic field and spin-orbit (SO) coupling as the perturbations.^{27,28} A 2nd-order magnetic response property is calculated as the derivative of the energy with respect to both perturbations, and contains two parts: one is the expectation value of the 2nd derivative of the Hamiltonian, of form $\langle 0 | \frac{\partial^2 H}{\partial x_1 \partial x_2} | 0 \rangle$, where x_1 and x_2 are the perturbations. The second is a sum-over-states expression connecting ground ($|0\rangle$) and excited ($|n\rangle$) states over the first derivatives of the Hamiltonian, $\frac{\partial H}{\partial x_1}$ and $\frac{\partial H}{\partial x_2}$. These two parts, and the terms contributing to them, are called *diamagnetic* and *paramagnetic* respectively.

The method used in this thesis calculates the following contributions to the *g*-tensor:

$$\mathbf{g} = g_e \mathbf{1} + \Delta \mathbf{g}_{SO/OZ} + \Delta \mathbf{g}_{RMC} + \Delta \mathbf{g}_{GC(1e)} \quad (2.4)$$

The paramagnetic contribution to Δg is given by $\Delta \mathbf{g}_{SO/OZ}$, the spin-orbit/orbital-Zeeman cross term. It can be of either sign, and usually dominates the *g*-tensor. It contains terms for both 1- and 2-electron SO-coupling, of the form:

$$\Delta g_{SO/OZ,uv} = \frac{2g_e \beta_e^3}{\hbar^2 \kappa_0 c^2} \frac{1}{\langle S_Z \rangle} \sum_N Z_N \sum_n \cdot \left[\frac{\langle 0 | \hat{\mathbf{O}}_1 | n \rangle \langle n | \hat{\mathbf{O}}_2 | 0 \rangle}{E_0^{(0)} - E_n^{(0)}} + c.c \right] \quad (2.5)$$

where N represents nuclei, n excited states and u and v the cartesian axes; the sums over i and j are over all orbitals; and "c.c" indicates the complex conjugate of the stated integrals. The integrals for the 1-electron SO coupling term are:

$$\langle 0 | \sum_i \frac{1}{r_{iN}^3} \times (\mathbf{l}_{iN})_u s_{iz} | n \rangle \langle n | \sum_j (\mathbf{l}_{jN})_v | 0 \rangle \quad (2.6)$$

and for the 2-electron SO coupling term:

$$\langle 0 | \sum_{ij} [\mathbf{r}_{ij} \times (\nabla_i - 2\nabla_j)]_u s_{jz} | n \rangle \langle n | \sum_k (\mathbf{r}_k \times \nabla_k)_v | 0 \rangle \quad (2.7)$$

The methodology used in this work applies the Atomic Meanfield Approximation (AMFI),²⁹ to evaluating the SO integrals of the paramagnetic contribution. This approximation is very accurate, and significantly reduces the computational cost involved.

The other two terms are diamagnetic, and generally smaller: the relativistic mass correction term $\Delta \mathbf{g}_{RMC}$ and the 1-electron gauge correction term $\Delta \mathbf{g}_{GC(1e)}$. An additional diamagnetic contribution, the 2-electron gauge correction term, is neglected.

In the case of a finite basis, problems of gauge-dependence arise in calculating the response of an electronic system to a magnetic field: some point in space must be specified as the gauge origin, and the choice of origin can affect the results for some systems. Usually the paramagnetic centre, or the spatial centre of the delocalised spin system is chosen. (Despite the similarity in names, gauge dependence and the diamagnetic gauge correction are unrelated effects.)

2.3 Hyperfine coupling calculation

The hyperfine coupling tensor, or A -tensor, of the nucleus N , may be separated into an isotropic value ${}^N A_{iso}$ and an anisotropic part, ${}^N \mathbf{A}$ or ${}^N \mathbf{T}$. In the nonrelativistic limit, A_{iso} arises from the Fermi contact term, which is directly proportional to the spin density ($\rho_\alpha - \rho_\beta$) at the nucleus in question, and hence easy to calculate. However, the result depends strongly on the quality of the wavefunction at the nucleus, and specifically the treatment of the wavefunction discontinuity termed the nuclear cusp. Accurate simulation of this requires a Gaussian-type orbital (GTO) basis set to possess a lot of high-exponent Gaussians (and also to be flexible enough generally to accommodate spin polarisation, an important contribution to A_{iso} for many systems). However, most chemical properties are insensitive to the quality of the nuclear cusp, and tight Gaussian functions are omitted by most basis sets as a needless expense. As a result, specialised basis sets have been developed for calculating good quality HFC data, such as the double- ζ set

EPR-II³⁰ used in this work. EPR-II is popular for such purposes as it gives good results at relatively low cost. For more accurate work, larger bases are available.

Another approach is to use Slater-type orbital (STO) basis sets, which by their nature are better at describing the nuclear cusp, although computationally more cumbersome than Gaussian functions. These tend to give similar quality results to larger Gaussian bases, with the curious result that different DFT functionals perform best for GTO and STO. Alternative Fermi contact operators have also been developed, which make results less dependent on the quality of the basis set. (See ref. 3, ch. 31.)

In the nonrelativistic limit, the anisotropic HFC tensor ${}^N\mathbf{A}$ describes through-space dipolar coupling between the electronic and nuclear magnetic dipoles. It is considerably less sensitive to the quality of the wavefunction than A_{iso} . The tensor components are calculated as follows:

$${}^N T_{uv} \propto \langle S_z^{-1} \rangle \sum_{\mu\nu} P_{\mu\nu}^{\alpha-\beta} \langle \phi_\mu | r_N^{-5} (r_N^2 \delta_{uv} - 3r_{N,u} r_{N,v}) | \phi_\nu \rangle \quad (2.8)$$

This formalism expresses the dipolar coupling in terms of the spin density matrix, $P_{\mu\nu}^{A-B}$, and the basis functions ϕ . r_N is the distance operator from the nucleus N , and $r_{N,u}$ is the component of same along the u -axis.

2.4 Molecular Dynamics

Molecular Dynamics, or MD, is the term used to describe calculations that simulate (within the point-nucleus approximation) the motion of nuclei over time. This is achieved by treating the simulated time as a series of very small timesteps, and for each timestep calculating the forces on the nuclei and updating their velocities and positions accordingly. Treating time as composed of a set of iterations, rather than continuous, is something of an approximation, but if the timestep τ is small enough, the effects of this approximation will be negligible. However, the smaller τ , the larger the number of iterations required to simulate enough dynamics to draw useful conclusions from.

The cheapest method of performing MD is molecular mechanics MD (MMMD), in which a force field is used to calculate all interactions between nuclei. This method is fast, and hence a useful method for calculation of large biological systems. However, it is limited by the nature of molecular mechanics: it cannot simulate reactions of any kind, and any unparameterised interactions simply cannot take place.

These limitations may be overcome by use of *ab initio* MD, in which the electronic wavefunction is treated explicitly, and the forces on the nuclei derived from it. Such methods are considerably more expensive, and the timespan that may be simulated is orders of magnitude less than that of MMMD (picoseconds, rather than nanoseconds). This is because not only are the forces more time-consuming to calculate, but the electronic structure must be updated each timestep.

The electronic wavefunction may be updated by performing an energy minimisation of it at each timestep. This is called Born-Oppenheimer MD (BOMD), as the electronic wavefunction is being quenched to the Born-Oppenheimer surface every iteration. This has the disadvantage that, every timestep, a full SCF cycle is performed, which is rather time-consuming.

The time-dependant Schrödinger equation may also be used to update the wavefunction each timestep, dictating as it does the wavefunction's rate of change as:

$$i\hbar\dot{\Psi} = \hat{H}\Psi \quad (2.9)$$

This approach is called Ehrenfest MD. It has the advantage of each timestep being far cheaper than for BOMD, as no SCF cycles must be performed. If the electronic wavefunction is optimised at the start of the simulation, and the timestep is small enough, the electronic wavefunction will stay at the ground state for the rest of the simulation (barring any events that might cause excitation). However, for this to happen, the value of τ must be far smaller than for the other methods. BOMD and MMMD need only simulate nuclear motion, which can be treated using a timestep of about 1 fs (depending on the system). The evolution of the electronic wavefunction is much faster, and a timestep of about 0.01 fs is required. Thus, Ehrenfest MD requires orders of magnitude more iterations than BOMD or MMMD to simulate a useful amount of time. As a result, although there are areas where Ehrenfest MD is useful - simulation of collision and electron scattering - it is not very suitable for computational chemistry.

A third approach to performing *ab initio* MD is to artificially slow down electronic motion, thus increasing the size of the timestep that may be used. This is done by use of a modified Lagrangian. In the most widely-used example of this, Car-Parrinello MD (CP-MD),³¹ a fictitious electronic kinetic energy $\frac{1}{2}\mu\langle\dot{\psi}|\dot{\psi}\rangle$ is introduced, with μ being the fictitious mass parameter:

$$L_{CP} = \sum_I \frac{1}{2} M_I \dot{\mathbf{R}}_I^2 + \sum_i \frac{1}{2} \mu \langle \dot{\psi}_i | \dot{\psi}_i \rangle - \langle \Psi_0 | H_e | \Psi_0 \rangle + [constraints] \quad (2.10)$$

Here, the indices i and I represent electrons and nuclei respectively. The

constraints imposed serve to maintain orthonormality, which is unfortunately not otherwise conserved.

The presence of a fictitious energy term is potentially problematic, as it could conceivably exchange energy with the physically meaningful energy terms. However, if μ is chosen appropriately, such that (on the nuclear motion timescale) the electrons adapt to nuclear motion instantly, this should not have a significant effect on the system's properties; and the electronic and nuclear motion will have sufficiently different power spectra to hinder exchange between the real and fictitious kinetic energies. The fictitious inertia of the electrons does have a retardant effect on the nuclear motion, however, causing a decrease in vibrational frequencies.³²

The result is a method that can treat electron dynamics using timesteps on the order of 0.1 fs. It is cheaper than BO-MD (although this is partly due to highly efficient implementation in the CPMD code). A similar method, developed in recent years, is atomic density matrix propagation (ADMP-MD).^{33,34} This similarly slows down the electron dynamics, enabling a larger timestep to be used; it does not, however, affect the vibrational frequencies.³⁵

2.4.1 Periodic boundaries and basis sets

The bulk properties of solid and liquid phases require the calculation to account for the system extending infinitely in every direction. This is commonly done by using periodic boundary conditions: the unit cell is defined, and repeats infinitely in every direction. Therefore if a molecule exits the unit cell in one direction, it re-enters on the other side. Periodic repetition in two directions gives a slab, which is useful for simulating the properties of surfaces, and repetition in one direction is suitable for chain-like systems, such as polymers.

In such situations, planewaves - sine and cosine functions - are a natural and convenient choice of basis set, as they repeat infinitely. A planewave basis function must have, in each direction, a wavelength equal to the box length divided by an integer. Thus the maximum wavelength is limited by the size of the box; in order to get a finite basis set, a minimum wavelength must also be defined. This is typically given as a single maximum frequency in Rydbergs (Ry), applying to all three dimensions. Thus, the basis set is characterised by a single parameter (and, for rigorous comparison, by the size of the unit cell.)

By construction, planewave bases contain the most diffuse functions they can, and are independent of the positions of the nuclei. This means that planewaves do not suffer the problem of a molecule expanding its wavefunction into another molecule's basis, using the latter as very diffuse basis

functions - in other words, making the effective basis set dependent on the molecular environment. This leads to unphysical forces (Pulay forces)³⁶ in MD simulation, and basis set superposition errors (BSSE)³⁷ in reaction energy calculations. However, truncation to a finite basis and resultant loss of high-frequency functions leads to problems describing fine structure and areas of steep gradients in the wave function (which atomic bases can easily be tuned to overcome). This is particularly problematic in the immediate vicinity of nuclei. As a result, planewave bases require use of pseudopotentials, even for hydrogen - both to avoid treating the core orbitals, and to make the wavefunction less steep in the vicinity of the nucleus.

Additionally, planewave wavefunctions suffer from a certain degree of noise, leading to electron density in empty regions and spin density far from a radical. The level of noise may be decreased by raising the frequency cutoff, and is least problematic when the contents of the unit cell are highly periodic, as with crystalline solids. It should also be noted that planewaves imply a cell size and periodic repetition; switching off periodic boundary conditions must be done by applying a correction to screen the contents of the cell from its periodic images.

2.4.2 Temperature control

The temperature of a simulated system can be measured by the nuclear kinetic energy, and thermostatted by slowing or speeding up the nuclei. This is useful, indeed necessary: typically, the initial state of the system will not have an amount of thermal (combined kinetic and potential) energy exactly equalling that of the desired temperature. Furthermore, the kinetic and potential energies may not be in equilibrium relative to each other, and may be unevenly distributed over the system (if, e.g., one molecule starts with an equilibrium structure, and another with all bond lengths displaced from equilibrium). For this reason, it is necessary to run the simulation for a while as an equilibration period, letting the potential and kinetic energies reach a balance. Once the system is well-equilibrated, with thermal energy properly distributed across all dimensions of the potential surface, the "production run" - the part of the simulation intended for analysis and extraction of properties from - can begin.

The simplest type of thermostat available is to rescale the nuclear velocities to the desired temperature whenever the temperature strays outside a specified limit (e.g. ± 50 K). This is a good solution if the system is large enough, but very problematic for small systems. Kinetic and potential energy are constantly interchanging in a statistical equilibrium: the amount of each form is constant over a period of time (and constant in the bulk limit of an

infinite system). But instantaneously, the ratio between kinetic and potential energy fluctuates for a finite system, and the smaller the system the more drastically it does so. The limit of this is a system with a one-dimensional potential well - for instance, a (stationary, non-rotating) diatomic molecule - which has all its thermal energy as potential energy when the bond stretches or contracts as much as it can, and all as kinetic energy at the equilibrium bond length. The temperature (as deduced from nuclear motion) will appear to oscillate between some maximum temperature and absolute zero, a completely pathological situation for a thermostat. In such cases, temperature control can be accomplished by applying a form of dynamical friction, speeding the nuclei up at one point and slowing them down at another, and transferring the energy to/from a fictitious heat bath. This is called Nosé-Hoover thermostating;^{38,39} by chaining several heat baths together (chain thermostating) it is possible to use it to handle the simplest of systems.⁴⁰

Chapter 3

Silasesquioxane-trapped H Atoms⁴¹

3.1 Introduction

Silasesquioxanes (or silsesquioxanes) are oligomeric silicon-oxygen cages of formula $(\text{RSiO}_{1.5})_n$. In these species, the Si atoms form the corners of a polyhedron, with adjacent Si atoms bridged by oxygen and substituents (R) terminating dangling bonds at Si. Silasesquioxane species of $n = 6, 8, 10, 12$ and higher are known (see Figure 3.1 for a depiction). This work is concerned with the cubic, $n = 8$ species, known as octasilasesquioxanes. We will refer to these simply as "silasesquioxanes" in this chapter, as we do not study any of the other systems, and label them RT_8 (apart from $\text{R} = \text{OSiMe}_3$, for which the label QM_8 is also used).

3.1.1 Importance of Silasesquioxanes

The cubic Si_8O_{12} system that defines an octasilasesquioxane is of interest as a model system for the cubic D4R cage found in many zeolites (albeit with a range of atoms, not merely silicon, at the vertices). Studies of silasesquioxanes can thus contribute insight into the D4R sites' properties.⁴² Zeolites are of considerable importance due to their wide range of applications, including as catalysts and molecular sieves. Similarly, silasesquioxanes have also been used as models for silica-mounted catalytic systems.⁴³ Silasesquioxane-based systems can themselves also serve as catalysts, and the potential of silasesquioxane-based nanocomposites is attracting increasing interest.^{44,45} Silasesquioxane resins find applications for their conductive properties, and silasesquioxanes with large organic substituents display liquid crystal phases.⁴⁴

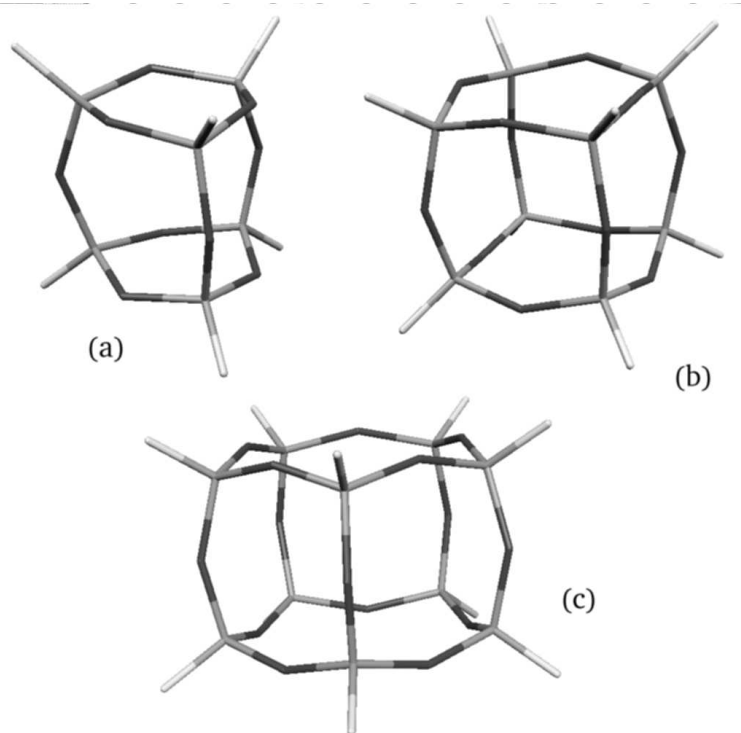


Figure 3.1: The silasesquioxane species $H_nSi_nO_{1.5n}$ for $n =$ (a) 6, (b) 8, (c) 10.

3.1.2 Trapped atoms

The central cavity of the octasilasesquioxane cage is capable of trapping radiolytically-generated hydrogen atoms. The resulting radical systems, denoted $H@RT_8$, are very stable - long-lived enough to study by EPR spectroscopy, even at room temperature and in solution.⁴⁶ Not only that, but even the presence of radical-scavenging species (NO , O_2 and I_2) does not alter the stability of the cage/radical system, whose decay follows simple first-order kinetics. In fact, radical scavengers counter-intuitively *enhance* caged-radical production. This is presumed to be due to preferential scavenging of other radiolytically-created radicals, which prevents recombination with the hydrogen atoms.⁴⁷

The EPR spectra of several $H@RT_8$ systems have been recorded, and display an interesting anomaly. Hydrogen atoms, both free and in solid matrices, generally exhibit negative Δg -values. This is because spin-orbit coupling effects at hydrogen are negligible, and the other contributions to the g -shift are negative overall. Remarkably, however, all $H@RT_8$ species studied display *positive* g -shifts. This suggests that the unpaired electron is significantly delocalised onto the silasesquioxane cage. Hyperfine coupling

data suggests the same thing, as the A_{iso} values are consistently less than that of a free hydrogen atom.

Species of type $F^-@RT_8$ - fluoride anions trapped in silasesquioxane cages - have also been reported.⁴⁸ These result from the presence of fluoride anions during synthesis of the silasesquioxane, so that the RT_8 cage forms around the fluoride ion.

In this chapter I report the results of our theoretical analysis of the EPR properties of the $H@RT_8$ radical system.

3.2 Computational Details

For our analysis of $H@RT_8$, we studied the systems $R = H, Me, Et, OMe, OSiH_3$ (a model for $R = OSiMe_3$), F, Cl, Br and I . We used the Gaussian98⁴⁹ program to perform geometrical structure optimisation at the UHF level, with the 6-31G(d) basis⁵⁰⁻⁵² used for all elements except the halogens, for which we used Effective-Core Potentials (ECPs)⁵³ and DZP valence bases.^{53,54}

For the calculation of EPR properties, the electronic structure calculations were rerun using both HF and DFT methods. The deMon program package^{55,56} was used to perform calculations on all systems using the BP86 density functional^{17,21} and the DZVP basis⁵⁷ (again, with the exception of halogens, for which the same ECPs and DZP valence bases were used as for the structure optimisation). The charge density and exchange correlation potential were fitted using auxiliary bases of sizes 5,4 (Si), 5,2 (C, O), 5,1 (H) and 3,3 (halogens, with the aforementioned ECPs).^a For some systems, similar calculations (*sans* fitting) were performed with Gaussian98, with the same basis sets but different density functionals: the local density functional SVWN5,^{19,20} the hybrid density functionals B3- and BHPW91,^{17,22,25,26,58,59} and Hartree-Fock. Some restricted open-shell (RODFT or ROHF) calculations were also performed to assess the effects of spin polarisation. Mulliken spin densities and Natural Population Analyses (NPA) were taken from these calculations, using the NBO3.0 program from the Gaussian98 package in the case of NPAs. The MOLEKEL program was used for visualisation of spin densities and molecular orbitals.

The g -shifts were calculated either with the deMon g -tensor module⁶⁰ (for electronic structures obtained via deMon) or with the MAG-ReSpect⁶¹ program package (for electronic structures obtained via Gaussian98) according to the methodology outlined in chapter 2. The gauge origin for the g -tensor

^aHere, n, m denotes n s -functions and m spd-shells with shared exponents.

calculation was located at the centre of the cage. For calculation of the Spin-Orbit (SO) matrix elements, SO pseudopotentials were used for halogens⁵³ and the all-electron atomic meanfield (AMFI) approximation for other elements. The paramagnetic $\Delta g_{SO/OZ}$ term was analysed in terms of both individual atomic contributions and contributions from separate excitations. Isotropic hyperfine coupling constants were taken from the Gaussian98 and MAG-ReSpect outputs.

3.3 Results

3.3.1 g-Tensors: Theory vs. Experiment

The calculated g -shift data is summarised in Table 3.1, along with the available experimental data (Δg_{iso} for R = H, Me, Et, OSiMe₃).⁶² For the four experimentally-studied systems, Figure 3.2 shows a plot of calculated against experimental data, with linear regression lines.

It is apparent that our main methodology, UDFT using the BP86 functional and fitting of charge density and exchange-correlation potential, sizeably overestimates the g -shifts. The plot of BP86 results against experimental data has a slope of 1.13 and a large intercept (185 ppm). (For G98+MAG, the slope is 1.19 and the intercept 175 ppm.) We attribute the overestimate of Δg to deficiencies in the BP86 functional's description of the electron density; but we also note that these deficiencies are highly systematic - the individual BP86 data-points do not deviate much from the best-fit line in Figure 3.2. If we correct the BP86 results for this error, the values do not deviate much from experiment, and we can predict experimental values for R = OMe and F (although not for R = Cl, Br and I, for reasons which will be discussed later).

Calculations performed with Gaussian98 - that is, without fitting - give g -shifts which are slightly higher, and hence in worse agreement with experiment. Evidently, fitted calculations benefit from a little error compensation - as do restricted open-shell calculations, which show that eliminating spin polarisation depresses the g -shifts, leading to better agreement with experiment for entirely the wrong reasons. We additionally note that basis set effects are not believed to be significant - test calculations with the larger basis set IGLO-III⁶³ indicate that the error here is on the order of 5 ppm.

We note that the B3PW91 hybrid functional gives better agreement with experimental g -shifts. However, due to the higher computational cost of hybrid functionals, and the qualitative accuracy of the BP86 functional, we will chiefly focus on BP86 results in our analysis of the g -shifts.

Table 3.1: g -shifts (ppm) for H@RT₈

Method	R:	H	Me	Et	OSiH ₃
deMon ^[a]					
	UBP86	1021	897	885	648
G98/MAG ^[b]					
	UBP86	1065	924	906	668
	<i>ROBP86</i>	<i>926</i>	<i>871</i>	<i>865</i>	<i>647</i>
	UB3PW91	808	700		
Exp. ^[c]		740	630	620	410 ^[d]

Method	R:	OMe	F	Cl	Br	I
deMon ^[a]						
	UPB86	693	677	459	-1097	-3472

All results obtained from UHF/6-31G(d) optimised structures. [a] deMon/deMon-EPR results with fitting of charge density and exchange-correlation potential and SO-ECPs for halogen atoms. [b] Gaussian98/MAG-ReSpect results, without fitting. [c] Ref. 62 [d] Experimental data for is R = OSiMe₃

3.3.2 HFCs and Dynamical Effects

It has been noted in experimental studies that the ¹H hyperfine coupling constants of H@RT₈ systems decrease with increasing temperature, whereas the g -values do not (within experimental error). This has been analysed in terms of the dynamics of the trapped hydrogen atom. A spherical harmonic oscillator model was used and values of the force constants were estimated from the observed temperature dependence.⁶² We decided to perform a similar analysis, but approaching from the other direction. By displacing the hydrogen atom from the centre of the cage, we mapped out its potential energy surface and fitted a quadratic potential to it, and calculated the effects of displacement on the EPR parameters. This allows us to estimate the zero-point energy (ZPE) and the root mean square (RMS) displacement at any temperature. From thence, we could estimate the magnitude of dynamical effects on the EPR parameters.

For a one-dimensional quantum harmonic oscillator, the mean-squared displacement is proportional to:

$$\langle X^2 \rangle = \frac{\hbar\omega}{k} \left[\frac{1}{2} + n \right] \quad (3.1)$$

Here k is the force constant; ω is the angular frequency, equal to $\sqrt{k/m}$ (the

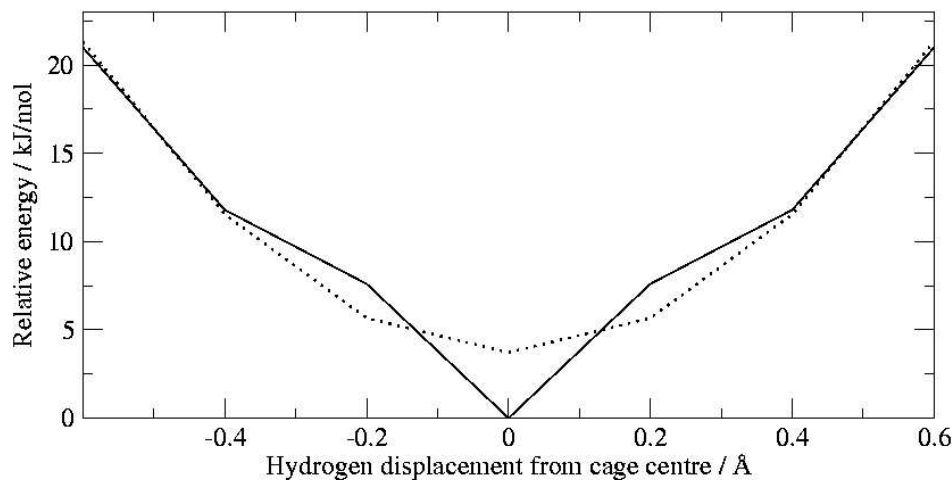


Figure 3.2: Energy curve for displacement of hydrogen from cage centre, averaged over different directions. The dotted line represents harmonic potential fit.

term arises from the classical case, where the displacement of a particle in simple harmonic motion depends sinusoidally on time); and n is the vibrational quantum number. We obtain the temperature average by replacing n with $(e^{\hbar\omega/kT} - 1)^{-1}$, and convert to the 3-dimensional, spherical harmonic oscillator case by multiplying the whole by 3. The potential energy curve for the trapped hydrogen unfortunately bears little resemblance to a quadratic potential. We have fitted a curve to it anyway (see Figure 3.3), but the results obtained should be taken as a rough estimate only.

At 0 K, i.e. at the lowest vibrational level, we obtain a zero-point energy of 3.0 kJ/mol and an RMS displacement of 3.2 Å. (Experimental estimates: 4.6 kJ/mol and 4.2 Å respectively⁶²). The zero-point contribution to the ^1H HFC is -13 MHz, and to the g -value is +31 ppm. Going from 0 K to 300 K, the RMS displacement increases to 4 Å. The ^1H HFC value decreases by 2.7 MHz, which compares well with the experimental attribution of 3-4 MHz to thermal effects.⁶² The g -value increases by about 3 ppm, which is smaller than the experimental uncertainty (the standard deviation is given as 10 ppm⁶²). Thus, our estimates of vibrational effects reproduce the experimental observations that the ^1H HFC is temperature dependent, whereas the g -value (to within experimental error) is not.

Table 3.2: Atomic contributions to H@RT₈ *g*-shifts.

	H	Me	Et	OSiH ₃	OMe	F	Cl	Br	I
Δg_{GC}	118	113	114	115	115	118	116	116	118
Δg_{RMC}	-129	-126	-126	-127	-127	-129	-129	-128	-128
$\Delta g_{SO/OZ}$	1031	909	897	660	705	688	472	-1085	-3463
Atomic contributions:									
12 × O	1094	974	964	794	823	861	919	922	980
8 × Si	-63	-60	-65	-96	-95	-105	-88	-87	-77
8 × R	0	-3	1	-34	-31	-68	-360	-1920	-4366
Δg_{total}	1021	896	885	648	693	677	459	-1098	-3472

All values in ppm. Results are from deMon-EPR calculations (BP86/DZVP).

3.3.3 Atomic contributions to *g*-shifts

The dominant contribution to the *g*-shifts of H@RT₈ systems is the spin-orbit coupling term $\Delta g_{SO/OZ}$ (see Table 3.2 for a breakdown of *g*-shifts into the different contributions). The other terms are nearly constant across all systems and amount to, on average, $\Delta g_{GC} = +116$ ppm and $\Delta g_{RMC} = -127$ ppm; both are relatively small, and cancel each other out. (In this methodology only the 1-electron part of Δg_{GC} is considered. The neglected 2-e⁻ terms are thought to be far smaller - we estimate -50 ppm.) Therefore, our analysis will concentrate on the $\Delta g_{SO/OZ}$ term.

Table 3.2 also shows the breakdown of the spin-orbit coupling term into separate atomic contributions, obtained by turning AMFI-SO coupling on or off at different atoms. It is clear that the observed positive *g*-shifts arise because of significant spin-orbit coupling at the cage oxygens, which is the dominant contribution, rather than the silicons, where the contribution is smaller and less variable.

The substituent contributions themselves are negligible for the systems with light-atom substituents, but this changes if halogenated cages are considered as well. The magnitude of SO coupling increases with atomic number, and for light atoms is small: for R = H, Me, Et, the substituent contribution is miniscule; it becomes an order of magnitude larger when dealing with oxygen (OSiH₃ or OMe) or fluorine, but still small. However, on moving down Group VII from F to I, the substituent contribution jumps dramatically. For R = Cl, the -360 ppm contribution substantially decreases the *g*-shift; for R = Br and I, the -1920 and -4366 ppm contributions outweigh the cage oxygen contributions entirely, and the overall *g*-shift becomes negative. If studies

(either experimental or theoretical) are performed on other H@RT₈ systems with second-row or heavier substituents (e.g. SH, SeH, TeH), we expect to see qualitatively similar trends.

We also note that the g -shifts are not much affected by movement of the hydrogen atom within the cage. We calculated atomic spin-orbit contributions for the H@HT₈ system with the H atom shifted 0.2 Å in the 100 direction, that is, towards a face of the cube. The four oxygen atoms on the edges of that cube face gain greater spin density, and their SO contribution increases by 132 ppm, from 364 to 498 ppm. The reverse occurs with the 4 oxygen atoms on the opposite cube face, whose contribution drops to 265 ppm. The remaining 4 atoms' contribution is almost unchanged, at 361 ppm, as their distance from the H atom hardly changes. Overall, the changes caused by H atom displacement largely cancel out; and the total contribution of the 12 oxygens to $\Delta g_{SO/OZ}$ shows only a modest increase of 30 ppm (from 1093 to 1123 ppm). Similar results are seen for other displacement vectors: displacement of the hydrogen atom has a significant effect on the spin density distribution, but the overall effects of this on the g -shift are small.

3.3.4 Spin density and g -values

The shape of the spin density distribution is depicted in Figure 3.4, which shows the spin-density isosurface ($\rho^{\alpha-\beta} = +0.001$) for H@HT₈. Most of the spin density is located on the trapped hydrogen atom, as expected. Notably, however, p -orbital-shaped spin densities are seen on the oxygen cage atoms. This is due to both delocalisation and spin-polarisation, as may be seen from the Mulliken spin densities in Table 3.3. Restricted open-shell calculations (ROHF/DZVP) find significant spin density at the cage oxygens, indicating delocalisation of the unpaired electron onto the oxygens (the SOMO is approximately the same shape as the spin density isosurface seen in Figure 3.4). Spin polarisation effects may be seen by comparing ROHF to UHF, and in the latter, the spin density at oxygen *increases*. This arises because of spin polarisation of the Si-O bonds - UHF calculations also show negative spin density arising at the silicon atoms.

We would expect that the Mulliken spin densities on oxygen would show the same trends as the oxygen contributions to the g -shift - R = H > Me, Et > OR'. However, this is not the case: for R = OSiH₃, the cage oxygen spin density is actually higher than for R = Me or Et.^b This is curious, because it is not entirely clear what gives rise to the trend in the oxygen spin densities.

^bThe dipolar components of the ¹⁷O hyperfine couplings follow the same trend, so this is unlikely to arise from artefacts in calculating the spin density.

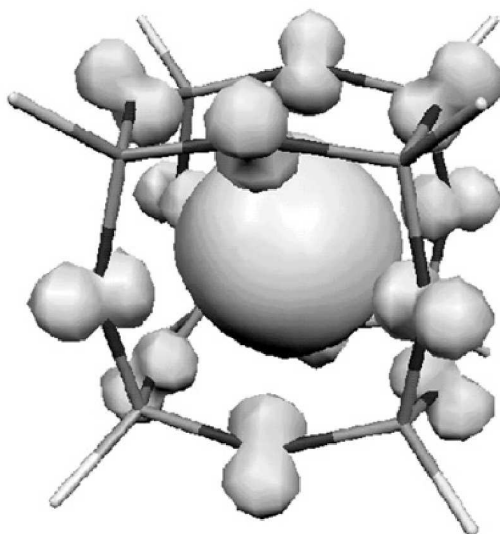


Figure 3.3: Spin density isosurface (+0.001 a.u.) for H@HT₈

The SO contributions from the cage oxygen seem to follow, inversely, the electronegativity of the substituent. The trend is approximate overall (R = H > I > Me, Et > Br > Cl > F > OR'), but holds exactly for the subgroups of halogen- or nonhalogen-substituted cages. Within these subgroups, however, the oxygen spin density initially decreases with substituent electronegativity, but this trend reverses when the substituents become very electronegative (R = H > Me, Et < OR'; R = I > Br < Cl < I).

At high electronegativity, we can point to inductive effects to explain this trend: OR', Cl or F substituents remove electron density from the cage, which then pulls (unpaired) electron density from the hydrogen atom, increasing the spin density on the oxygens. However, we presently have no explanation for the competing effect that causes oxygen spin density to drop from R = H to Me and from R = I to Br. (We note also that spin *polarisation* drops with substituent electronegativity, as we might expect: as the cage becomes more electron-poor, its orbitals become less polarisable. However, as the oxygen spin density trends show up even in ROHF calculations, this does not solve our problem.)

3.3.5 Excitation analysis of $\Delta g_{SO/OZ}$

The equation for SO/OZ coupling contributions to the g -tensor (see Chapter 2, Equations 2.5-2.7) couples occupied with unoccupied orbitals of the same

Table 3.3: Mulliken atomic spin densities.

R:	H	Me	Et	OSiH ₃
<i>H</i>				
BP86	0.876 (0.870) ^[a]	0.885 (0.877)	0.884 (0.873)	0.881 (0.873)
SVWN5	0.838 (0.836)	0.847		
B3PW91	0.910(0.908)	0.915	0.915	0.912
BHPW91	0.941 (0.943)	0.943		
<i>12 × O^[b]</i>				
BP86	0.156 (0.126)	0.145 (0.118)	0.145 (0.117)	0.149 (0.120)
SVWN5	0.166 (0.151)	0.152		
B3PW91	0.129 (0.093)	0.120	0.120	0.125
BHPW91	0.106 (0.061)	0.098		
<i>8 × S_i^[b]</i>				
BP86	-0.035 (0.001)	-0.029 (0.004)	-0.028 (0.008)	-0.030 (0.006)
SVWN5	-0.007 (0.008)	0.001		
B3PW91	-0.041 (-0.002)	-0.035	-0.034	-0.037
BHPW91	-0.047 (-0.005)	-0.044		
<i>8 × R^[b]</i>				
BP86	0.009 (0.003)	-0.001 (0.001)	-0.001 (0.002)	0.000 (0.001)
SVWN5	0.003 (0.005)	0.000		
B3PW91	0.002 (0.001)	0.000	-0.001	0.000
BHPW91	0.000 (0.001)	0.003		

Taken from G98 UBP86/DZVP calculations. Hartree-Fock results are: 0.063 (0.025)^[a] on O, -0.048 (-0.017) on Si. [a] Results in parenthesis refer to restricted open-shell (RO) calculations. Negative values arise as artefacts of the Mulliken analysis. [b] Summed over all equivalent atoms or groups.

spin. Therefore, the contributions it makes may be broken down into three types:

- (A) Excitation from the α -SOMO to virtual orbitals ($\Sigma[\text{SOMO} \rightarrow \mathbf{v}(t_{1g})]$).
- (B) Excitation from doubly-occupied orbitals to the unoccupied β -SOMO ($\Sigma[\mathbf{d}(t_{1g}) \rightarrow \text{SOMO}]$)
- (C) Excitations from doubly-occupied to virtual orbitals ($\Sigma[\mathbf{d} \rightarrow \mathbf{v}]$). (In a restricted-open shell calculation, the α and β orbitals give contributions of equal magnitude but opposite sign, and thus cancel out. In an unrestricted calculation, spin polarisation causes the α and β contributions to differ slightly, and these contributions become non-zero.)

We have performed excitation analysis on the systems $R = \text{H, Me, OSiH}_3$. The results are given in Table 3.4. The trend in the $\Delta g_{SO/OZ}$ couplings chiefly arises from type B couplings, which are large and positive. Type A couplings are small and positive; type C couplings are small and negative.

The symmetry of the H@RT_8 systems is cubic (O_h), or very close to. Therefore, in this case, there are definite symmetry rules determining which excitations can contribute to $\Delta g_{SO/OZ}$. In the sum over states expression for $\Delta g_{SO/OZ}$, the operators involve angular momentum operators, which possess t_{1g} symmetry. In order for the $\langle \psi_k^\beta | H_{SO} | \psi_a^\beta \rangle \langle \psi_a^\beta | l_O | \psi_k^\beta \rangle$ integrals to be non-zero, the product of the two orbitals involved must also possess t_{1g} symmetry. For A and B type couplings, the symmetry of the SOMO (a_{1g} , or fully symmetric) requires the other orbital to possess t_{1g} symmetry, i.e. to be triply degenerate.

In our analysis of B-type contributions, we find that the largest terms consistently arise from excitations from two particular sets of triply-degenerate orbitals. We label these as $1t_{1g}$ and $2t_{1g}$, and list their contributions in Table 3.4, together with the integrals and energy denominator. The $1t_{1g}$ orbitals are lower in energy, -9 eV below the SOMO, and are Si-O bonding in character. The $2t_{1g}$ orbitals are higher in energy, -5 eV below the SOMO, and are nonbonding oxygen lone-pair orbitals. Both sets of orbitals have large, p -orbital-like lobes at the cage oxygens, approximately orthogonal to each other and to the p -like lobes in the SOMO.

Looking at the ROBP86 calculations, we see a sizeable difference between the contributions of the $1t_{1g}$ and $2t_{1g}$ excitations. This difference arises because of the integral numerator being larger, and the energy gap denominator ($\Delta\epsilon$) being smaller, for $2t_{1g}$ than $1t_{1g}$. If we go to the unrestricted framework, however, the difference between the contributions of the two sets of orbitals grows smaller, mostly due to the integral numerators for $1t_{1g}$ increasing, and for $2t_{1g}$ decreasing - the result being that the numerators differ little. Spin polarisation also causes the energy-gap denominator $\Delta\epsilon$ to decrease slightly

Table 3.4: Contributions to $\Delta g_{SO/OZ}$

R:	H	Me	OSiH ₃
$1t_{1g} \rightarrow \text{SOMO}$			
Contribution	301 (150) ^[a]	272 (132)	166 (79)
$ \Delta\epsilon/eV ^{[b]}$	8.54 (8.90)	8.72 (8.81)	8.79 (9.10)
$\langle\psi_k^\beta H_{SO} \psi_a^\beta\rangle\langle\psi_a^\beta l_O \psi_k^\beta\rangle^{[c]}$	94 (49)	87 (43)	54 (26)
$2t_{1g} \rightarrow \text{SOMO}$			
Contribution	586 (692)	480 (664)	394 (590)
$ \Delta\epsilon/eV $	4.53 (4.89)	4.62 (4.71)	4.54 (4.85)
$\langle\psi_k^\beta H_{SO} \psi_a^\beta\rangle\langle\psi_a^\beta l_O \psi_k^\beta\rangle$	98 (125)	82 (115)	66 (105)
$\Sigma[\text{SOMO} \rightarrow \mathbf{v}(t_{1g})]$	357 (102)	379 (108)	163 (26)
$\Sigma[\mathbf{d}(t_{1g}) \rightarrow \text{SOMO}]$	887 (824)	702 (773)	455 (667)
$\Sigma[\mathbf{d} \rightarrow \mathbf{v}]$	-171	-146	-61
Total $\Delta g_{SO/OZ}$	1073 (934)	935 (880)	679 (657)

Values in ppm. Extracted from G98+MAG UBP86 calculations. [a] ROBP96 values are in parenthesis. [b] Kohn-Sham t_{1g}/SOMO energy gap (serves as denominator in Equation 2.5). [c] Spin orbit coupling integrals (numerators in Equation 2.5).

for both $1t_{1g}$ and $2t_{1g}$.

The trend in the $1t_{1g}$ and $2t_{1g}$ contributions matches the overall trend in the g -shift, and arises from the integral numerators $\langle\psi_k^\beta|H_{SO}|\psi_a^\beta\rangle\langle\psi_a^\beta|l_O|\psi_k^\beta\rangle$. The energy denominators do not show the same trend, dropping from R = H to Me then rising for R = OSiH₃. Overall, the type-B contributions, dominated by the $1t_{1g}$ and $2t_{1g}$ excitations, are responsible for the trends in the $\Delta g_{SO/OZ}$ term; although the drop in $\Delta g_{SO/OZ}$ from Me to OSiH₃ arises partly from a drop in the type-A ($\Sigma[\text{SOMO} \rightarrow \mathbf{v}(t_{1g})]$) contribution too.

3.3.6 Parameter Dependence on DFT Functional

As may be seen from Table 3.1, the calculated g -shifts vary significantly with functional used. g -Shifts of radicals generally show some functional dependence because of the slight differences in how the spin density is described, but normally these differences are far smaller for main-group elements (although not for transition metals). In the case of H@HT₈, however, SVWN5 gives over twice the value of BHPW91, and almost twice the experimental value.

In this case, where the g -shift arises mostly from contributions at oxygen,

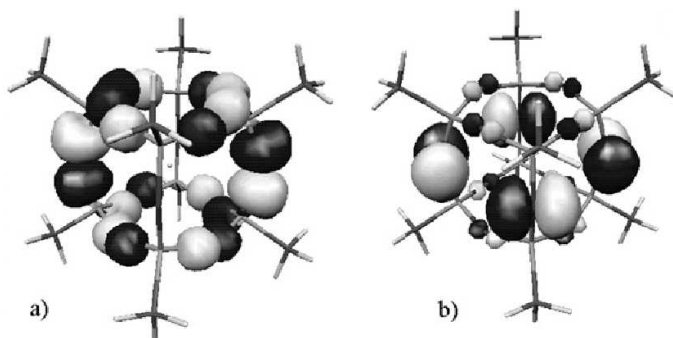


Figure 3.4: Occupied, triply-degenerate orbitals involved in SO coupling: (a) $1t_{1g}$, (b) $2t_{1g}$

we would expect the functional dependence to arise chiefly from the description of the spin polarisation at and spin delocalisation to oxygen. If we compare the g -shifts to the Mulliken spin densities at oxygen, we find they do indeed correlate (see Table 3.3). SVWN5, which locates the most spin density on oxygen and the least on hydrogen (and virtually none on Si), gives the largest g -shifts. The gradient-corrected BP86 functional locates more spin on hydrogen and slightly less on oxygen; it also treats the Si-O bond as being more spin-polarisable, and locates a sizeable amount of *negative* spin on silicon. Moving from pure density functionals to hybrid functionals, more spin becomes located on hydrogen and less on oxygen. Finally, pure Hartree-Fock locates very little spin on oxygen, and sizeably underestimates Δg as a result.

The relationship between spin density at oxygen and the g -shift as the functional changes is not linear, but there is a definite correlation (see Figure 3.5).

Comparison of ROB86 and ROSVWN5 results suggests that the Local Density Approximation (LDA) functional SVWN5 significantly overestimates the delocalisation of the SOMO onto the cage oxygens. In the UDFT case this is partly compensated for by lack of spin polarisation of the Si-O bond - with other functionals, this causes a significant increase in the spin at oxygen, but the effect is almost absent with USVWN5. Moving from UBP86 to hybrid functionals, the delocalisation of the SOMO onto cage oxygens becomes weaker and weaker with more and more exact exchange included, and the g -shifts drop accordingly; although the effect of this is partly cancelled by increasingly strong spin polarisation, which locates positive non-SOMO spin density at oxygen.

The spin density trends also correlate with the calculated hyperfine cou-

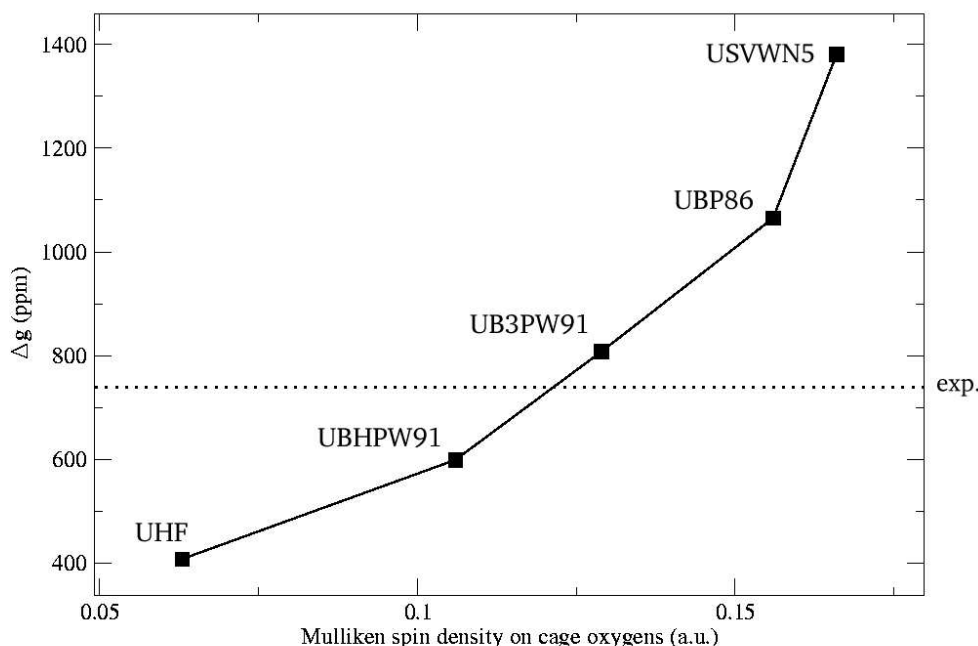


Figure 3.5: Plot of calculated g -shifts and oxygen spin densities for different functionals (DZVP results for H@HT_8)

plings, which are shown (together with experimental HFCs) in Table 3.5. The ^1H HFCs are large and positive, reflecting the sizeable $1s$ spin density at the nucleus, while the ^{29}Si HFCs are small and negative, reflecting the small negative spin density around Si caused by polarisation of the Si-O bond. The ^1H HFCs depend pretty directly on the amount of spin located at hydrogen, and thus vary as $\text{SVWN5} < \text{BP86} < \text{B3PW91} < \text{BHPW91} < \text{HF}$. (Our UHF and UB3PW91 results agree well with prior UHF and B3LYP results calculated.⁶⁴) If the absolute values of the ^1H A_{iso} are regarded, UB3PW91 appears to perform best, although this is an unreliable measure since our calculations were not performed with a suitable basis set for accurate HFC calculations. If the results are taken relative to the A_{iso} of a free hydrogen atom, as calculated by the same functional (i.e. if we examine how trapping affects the A_{iso} value), UBHPW91 is superior (see Table 3.5(b)). Experimentally, $A_{iso}(\text{H@HT}_8)/A_{iso}(\text{vac.})$ is equal to 0.99. USVWN5 gets this ratio to be 0.90; UBP86, 0.94; UB3PW91, 0.96; UBHPW91, 0.98; and UHF, 1.08. The overlarge spin delocalisation away from H by SVWN5 has been remarked upon; what is most curious here is that UHF actually finds the spin at the H nucleus to be *increased* by trapping in a silasesquioxane. The indication is

that there are competing influences on the ^1H A_{iso} : it is decreased by removal of spin to cage oxygens, but apparently increased by compression of the hydrogen $1s$ orbital by the electron density of the cage. This also explains why the experimental A_{iso} is almost unchanged from the vacuum value, despite the delocalisation of significant spin density onto the cage evident from both calculations and the empirical g -shifts.

The hybrid functional B3PW91 performs best in describing the ^{29}Si HFCs, which follow the same trend in magnitude. The A_{iso} values are negative, which, as ^{29}Si has a negative magnetogyric ratio, indicates positive spin density; as this occurs also in RO calculations, this represents spin delocalisation onto Si. However, spin polarisation is also important, decreasing the magnitude of the coupling by about 2 MHz. As B3PW91 also describes ^1H HFCs and the g -shift reasonably well, we conclude that of all the functionals it probably describes the spin density distribution of the system best.

Table 3.5 (a): Hyperfine coupling constants for H@RT₈

	H	Me	Et	OSiH ₃
¹ H:				
SVWN5	1219 (1197)	1226		
BP86	1360 (1339)	1368 (1348)	1369 (1347)	1371 (1351)
B3PW91	1412 (1394)	1419	1420	1419
BHPW91	1433 (1420)	1438		
HF	1569 (1561)			
Exp. ^[a]	1413	1418	1416	1418
²⁹ Si:				
SVWN5	-10.1 (-12.1)	-8.2		
BP86	-7.1 (-9.3)	-5.9 (-8.1)	-5.5 (-7.9)	-1.7 (-4.6)
B3PW91	-4.9 (-7.0)	-4.1	-3.7	-1.1
BHPW91	-3.2 (-5.1)	-2.6		
HF	-1.3 (-3.1)			
Exp. ^[b]		4.6	4.2	1.7 ^[c]

Table 3.5(b): ¹H HFCs: comparison to vacuum values

	SVWN5	BP86	B3PW91	BHPW91	HF	Exp. ^[a]
$A_{iso(vacuum)}$	1354	1447	1468	1467	1458	1420
Unrestricted calculations:						
$A_{iso}(H@HT_8)$	1219	1360	1412	1433	1569	1413
" / $A_{iso(vac)}$	0.90	0.94	0.96	0.98	1.08	0.99
Restricted open-shell calculations:						
$A_{iso}(H@HT_8)$	1197	1339	1394	1420	1561	1413
" / $A_{iso(vac)}$	0.88	0.93	0.95	0.97	1.07	0.99

All values in MHz, taken from G98 calculations with DZVP basis. Restricted open-shell (RO) values are in parenthesis. [a] Extrapolations to 0 K from ref. 62, except vacuum value (ref. 65) [b] Ref. 47

Chapter 4

Benzosemiquinone Molecular Dynamics^{66, 67}

4.1 Importance of Benzosemiquinones

Para-semiquinone radical anions are bioradicals of considerable importance, occurring in all living things.⁶⁸⁻⁷⁰ The Q/Q^{•-} or Q/QH₂ redox couples serve an electron transfer role in respiration and photosynthesis. The precise nature of their interaction with the proteins from and to which they transfer electrons is a subject of much interest, and numerous EPR studies have been performed on the issue.^{71, 72} The interpretation of the EPR data has in turn been assisted by quantum chemical analysis, with computational studies seeking to catalogue the effects of solvent-semiquinone interaction or assess model systems by comparison of calculated with experimental EPR parameters.

Para-benzosemiquinone, C₆H₄O₂^{•-} or BQ^{•-}, does not itself have a prominent role in biological systems. However, it is the most basic semiquinone possible, and thus serves as a prototype for its larger relatives. The important feature, common to all, is the basic C₆O₂^{•-} structural unit: it is this that is oxidised and reduced, and it is the oxygens and π -system of this unit that accept hydrogen bonds, modifying its redox potential and spin density distribution. The study of BQ^{•-} allows analysis of these effects in the absence of side-groups, and understanding its behaviour gives a baseline from which to interpret data regarding larger and more complicated semiquinones, such as the biologically-important plasto- and ubisemiquinones (PQ^{•-} and UQ^{•-} respectively).

We decided to perform molecular dynamics simulations on benzoquinone and -semiquinone, both in the gas phase and in aqueous solution, in the hope of improving our understanding of this important class of bioradicals and,

particularly, treating solvation effects in a more complete manner. Static calculations typically include only the first solvation sphere of the molecule; our simulations, using a larger number of water molecules and periodic boundary conditions, should treat the interaction of the molecule with the bulk solvent more realistically.

4.2 Computational Details

4.2.1 Molecular Dynamics

Car-Parinello MD simulations were performed in all cases using the CPMD code, v. 3.5.2,⁷³ with a unit cell of size 14.0 x 12.0 x 11.8 Å. The gradient-corrected BLYP density functional was used,^{17,18} with a planewave basis (cutoff: 70.0 Rydberg) and norm-conserving pseudopotentials of Troullier-Martins type⁷⁴ (cutoffs: 0.5 a.u. [H], 1.05 a.u. [O], 1.23 a.u. [C]). The MD timestep was 7 a.u. (0.17 fs), and the electronic mass was set to 1000 a.u. The temperature of the simulations was set to 300 K. For the solvated systems, thermostating was accomplished by rescaling the kinetic energy of the nuclei whenever the temperature deviated more than a specified tolerance (± 50 K) from the desired 300 K temperature. For the gas-phase systems, Nosé thermostating had to be employed.^{38,39} The following simulations were performed:

- Benzosemiquinone radical anion (BQ^{•-}) in aqueous solution. 60 water molecules were included in the simulation and periodic boundary conditions were applied. A total of 11.1 ps were simulated. The initial 4.8 ps were discarded as an equilibration period, and 6.3 ps were kept as production run.
- Neutral benzoquinone (BQ) in aqueous solution. 60 water molecules were included, and periodic boundary conditions were applied. The simulation length was 6 ps; the initial 4 ps were discarded as equilibration, and 2 ps were kept as production run.
- Gas-phase BQ^{•-}. Periodic boundary conditions were switched off for this simulation. 7.3 ps were simulated using temperature rescaling. However, due to the small system size, the temperature fluctuated, and a switch to Nosé thermostating was required. An equilibration period of 1.7 ps was simulated using "massive" thermostating (coupling every degree of freedom to a separate thermostat); another 6.8 ps were simulated as a production run, using only a single thermostat for all degrees of freedom.

- Gas-phase BQ. Periodic boundary conditions were switched off. 1.7 ps were simulated using "massive" Nosé thermostating, and 1.5 ps were simulated with a single thermostat and taken as production run.

Certain static calculations were run with Gaussian 03⁷⁵ to assess hydrogen bonding to carbonyl oxygens. These used the BLYP functional and the TZVP basis set,⁷⁶ and will mainly be discussed in the next chapter. Additionally, to obtain the potential energy curve of T-stacking hydrogen bonds, we performed constrained optimisations on a T-stacked BQ^{•-} + H₂O system, at the BP86//DZVP level.^{17,21,57} Without constraints, this system optimises to have both hydrogens pointing down at the ring, i.e. forms 2 T-stacked hydrogen bonds. Therefore we took the optimised structure of T-stacked BQ^{•-} + *N*-methylformamide (NMF)⁷⁷ and replaced NMF with water, keeping the H-bonded proton in the same position. The O-H bond was constrained to remain perpendicular to the plane of the ring and the *z*-coordinate (height above the ring) of the bonding proton was changed; all other degrees of freedom were relaxed. The energy curve was counterpoise-corrected by calculating the basis-set superposition error (BSSE)³⁷ at its minimum point.

4.2.2 Solvation Analysis

For analysis of the solvation sphere of BQ and BQ^{•-}, we applied the following criteria for hydrogen bond recognition:

- Hydrogen bonds to the carbonyl oxygens were recognised if $r[\text{O}\cdots\text{H}] \leq 2.25 \text{ \AA}$ and $\angle(\text{O}\cdots\text{H}-\text{O}) \geq 90^\circ$.
- "T-stacking" hydrogen bonds to the π -system were recognised if $r[\text{O}\cdots\text{H}] \leq 3.0 \text{ \AA}$, $\angle(\text{C}\cdots\text{H}-\text{O}) \geq 120^\circ$ and $\angle(\text{H}\cdots\text{C}\cdots[\text{m}]) \leq 135^\circ$, where [m] is the midpoint of the C₆ ring.

Radial distribution functions (RDFs) of these hydrogen bond types were created by imposing only the angular criteria and dividing by a suitable surface area function. Usually, the function $4\pi r^2$ is used, which assumes the molecule under consideration is spherical. We used this for to-oxygen H-bonds, but derived a surface area of $20 + 13r^a$ for T-stacked hydrogen bonds.

^aWe assumed that for the values of r involved, the surface area at $r \text{ \AA}$ from the C _{π} ring was approximately a circle above and below the C _{π} ring - this gave rise to a constant term - a torus connecting the side of the two circles. This torus, further truncated by the various criteria involved, gave rise to a linear dependence on r .

We additionally plotted the three-dimensional spatial distribution function (SDF) - i.e. the average atomic densities - for BQ^{•-} over the length of the production run, symmetrising over the mirror planes of the BQ^{•-} molecule.

4.3 H-Bonding Analysis

4.3.1 H-Bonding to carbonyl

The principal mode of hydrogen bonding to both BQ and BQ^{•-} is to the carbonyl oxygens. The degree to which H-bonding occurs is a matter of considerable interest, as it influences the geometry (by elongation of the C-O bond)⁷⁸ and has a sizeable effect on the EPR properties (see Chapter 5). As expected, the aqueous simulations show significant hydrogen bonding to both the neutral and the anionic systems. While the exact number of hydrogen bonds found varies with the somewhat arbitrary choice of criteria, distinctly more H-bonding occurs to the anionic system regardless of criteria. With a 2.25 Å distance cutoff, we typically find 2 or 3 hydrogen bonds to each carbonyl oxygen for the anion, and only 1 or 2 for the neutral system.

The RDFs of the two systems are shown in Figure 4.1. The stronger and more extensive H-bonding to the anion can be seen clearly, both by the higher maximum of the anionic RDF (twice as high as that of the neutral system) and by the shorter distance at which the RDF maximum occurs (1.75 Å vs 1.95 Å). These peak distances are in good agreement with other estimates of the equilibrium H-bond lengths. Static cluster calculations obtained distances of 1.98 Å for the neutral system with 2 water molecules H-bonded⁷⁸ and 1.76 Å for the radical anion with 4 water molecules.⁷⁹ Experimental data (²H nuclear quadrupole couplings from Q-band ENDOR studies of 80 K frozen solution) suggest 1.76 ± 0.03 Å for BQ^{•-}.⁸⁰

Both RDFs decline sharply from their equilibrium distance until about 2.2-2.25 Å, and thereafter there is a shallow decline up until a minimum around 2.7 Å, which can be considered the boundary between the first and second solvation spheres. In Table 4.1, we provide the number of hydrogen bonds using both 2.25 and 2.7 Å as distance cutoffs. Within 2.7 Å we find 3.7 and 5.6 hydrogen bonds for BQ and BQ^{•-} respectively, dropping to 2.4 and 4.7 with a 2.25 Å cutoff. This is more than is normally assumed when performing static calculations, which tend to bind 2 or 4 solvent molecules to BQ^{•-}. (This is an understandable assumption for theoretical work, as BQ^{•-} + 5H₂O tends to rearrange such that there are 4 HOH[⋯]BQ^{•-} linkages, and one HOH[⋯]OH₂. We briefly discuss this at the end of this chapter.) Experimental estimates as to the number of hydrogen bonds are difficult to make; frozen

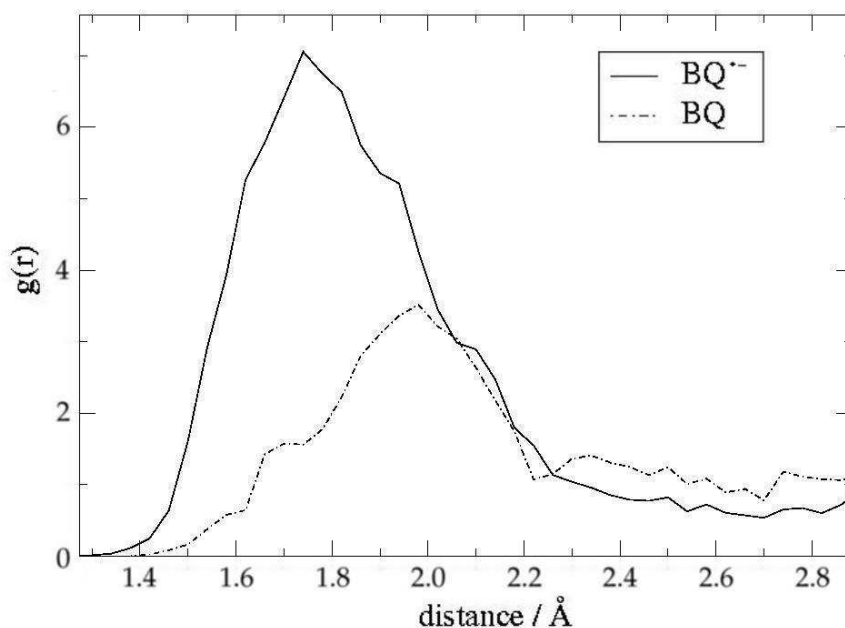


Figure 4.1: Radial distribution functions (RDFs) of water molecules H-bonded to (semi)quinone oxygens.

solution data has been interpreted to suggest 2 or 4 H-bonds to BQ \bullet^- on the basis of HFC data,⁸⁰ which we will discuss in the next chapter.

The comparative frequency of different hydrogen-bonding situations is shown in Tables 4.2 and 4.3, for both BQ and BQ \bullet^- trajectories, with a 2.25 Å cutoff applied for hydrogen bonding to carbonyl oxygens.

As seen in Table 4.2, the anionic semiquinone shows a distinct preference for 4 to 5 hydrogen bonds, although the total H-bonds observed varies between 2 and 7. The neutral benzoquinone system shows considerably less hydrogen bonding, between 1 and 4 H-bonds, with a preference for 2 or 3. In Table 4.3 this is further broken down into specific configurations, labelled as " x/y ". This nomenclature indicates x H-bonds to one end of the molecule and y to the other. Both oxygen atoms are regarded as interchangeable and the greater number is listed first, hence $2/3$ would count as $3/2$.

For the anionic semiquinone, the most frequent H-bonding situations are $3/2$ and $2/2$ - i.e. 2 hydrogen bonds to one end of the molecule, and either 2 or 3 to the other end. For the neutral quinone, the commonest configurations are $2/1$ and $1/1$. This is consistent with the average numbers of hydrogen bonds to carbonyl, which are 2.4 for BQ and 4.7 for BQ \bullet^- . The third most common configuration is $1/0$ for BQ, and $3/3$ for BQ \bullet^- . Remarkably, one

Table 4.1: Average H-bond numbers

System:	Number of H-bonds of type:		
	O \cdots H($\leq 2.7\text{\AA}$)	O \cdots H ($\leq 2.25\text{\AA}$)	C \cdots H ($\leq 3.0\text{\AA}$)
<i>CPMD</i>			
BQ	3.7	2.4	0.4
BQ \bullet -	5.6	4.7	1.1
<i>MM-MD</i> ⁸¹			
BQ	3.4	-	-
BQ \bullet -	6.6	-	-
<i>QM-MM</i> ⁸²			
BQ		3.0 ^[a]	-

[a] O \cdots H($\leq 2.5\text{\AA}$).

Table 4.2: Frequency, correlation with $d[\text{C-O}]$ of H-bond numbers

H-bond number	% occurrence		$d[\text{C-O}]$ ^[a]	
	BQ	BQ \bullet -	BQ	BQ \bullet -
<i>O-H bonds</i>				
1	16.2	-	1.248	-
2	39.3	1.7	1.250	(1.292)
3	36.8	6.4	1.251	1.304
4	7.7	32.2	1.255	1.303
5	-	43.6	-	1.305
6	-	15.1	-	1.308
7	-	1.0	-	(1.309)
<i>T-stacked H-bonds</i>				
0	66.5	23.9	1.250	1.306
1	25.8	50.4	1.252	1.305
2	7.3	17.4	1.252	1.303
3	0.4	8.2	(1.249)	1.299
4	-	0.3	-	(1.302)

[a] Brackets indicate values considered statistically unreliable due to low frequency of the relevant hydrogen bonding situation.

Table 4.3: Frequency of H-bonding configurations

Configuration	% occ. (BQ)	% occ. (BQ ^{•-})
1/0	16.2	-
1/1	34.5	1.6
2/0	4.8	0.0
2/1	36.8	6.4
2/2	1.6	25.2
3/1	6.1	6.9
3/2	-	42.2
3/3	-	15.1
4/1	-	1.4
4/2	-	0.2
4/3	-	0.9

carbonyl oxygen has no hydrogen bonds attached for a total 21 % of the time in the BQ simulation (1/0: 16 %, 2/0: 5 %). In the BQ^{•-} simulation, on the other hand, a 2/0 configuration occurs in only 2 snapshots out of 7400 - a 0.03 % frequency.

The three-dimensional SDF of the solvation sphere around BQ^{•-} is shown in Figures 4.2 and 4.3. Both ENDOR measurements⁸⁰ and structure optimisations of benzosemiquinone consistently show a preference for hydrogen bonds to oxygen to be in the plane of the molecule.^{79,83-86} This preference is reflected in Figure 4.2, where an accumulation of hydrogen density can be seen on either side of the carbonyl oxygen, like a pair of brackets. However, the potential energy surface is very shallow, and a lot of out-of-plane hydrogen bonding does occur. For this reason, at a lower isosurface value, the brackets of H density become rings, which can be seen clearly in Figure 4.3. Also notable is that for strongly out-of-plane H-bonding, the preferred (H··O-C) angle decreases. This is because out-of-plane H-bonds interact more with the π -system at oxygen, which is perpendicular to the C-O bond, rather than the lone pairs, which are at around 120° to it; and this can be seen in Figure 4.3, as the donut-shaped H-density bends in towards the π -system above and below the plane of the ring.

We imposed angular criteria for H-bond recognition to account for the directionality of H-bonds. In the case of T-stacked H-bonds (see below) these criteria are important, but in the case of to-oxygen H-bonds the difference made is negligible. Relaxing the angular criterion and repeating the analysis (with a distance cutoff of 2.7 Å) indicates that it only excludes 0.02 potential hydrogen bonds per snapshot in the case of BQ, and 0.002 per snapshot for BQ^{•-}. Orientation of nearby water molecules towards the carbonyl oxygen is

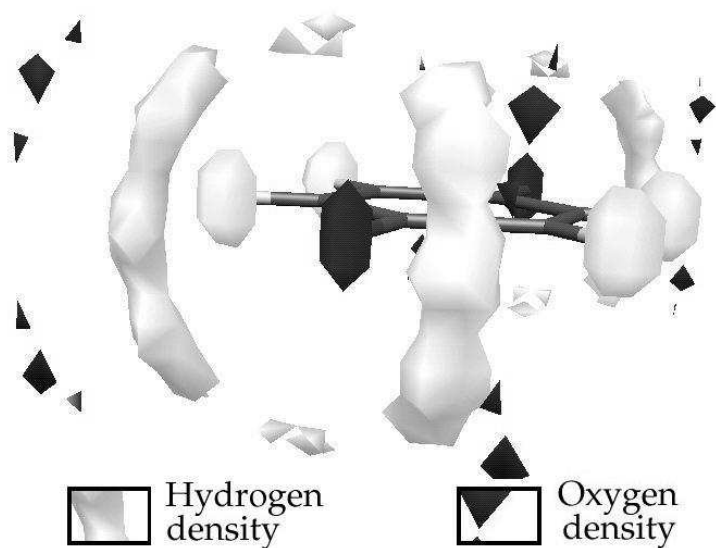


Figure 4.2: Spatial distribution function (SDF) for aqueous benzosemiquinone simulation. Isodensity surface: 0.3 \AA^{-3} .

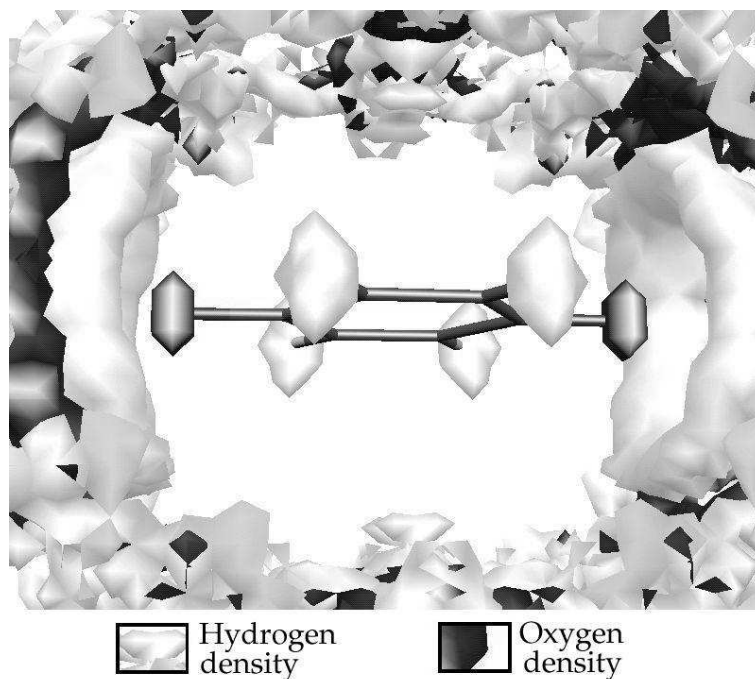


Figure 4.3: Spatial distribution function (SDF) for aqueous benzosemiquinone simulation. Isodensity surface: 0.1 \AA^{-3} .

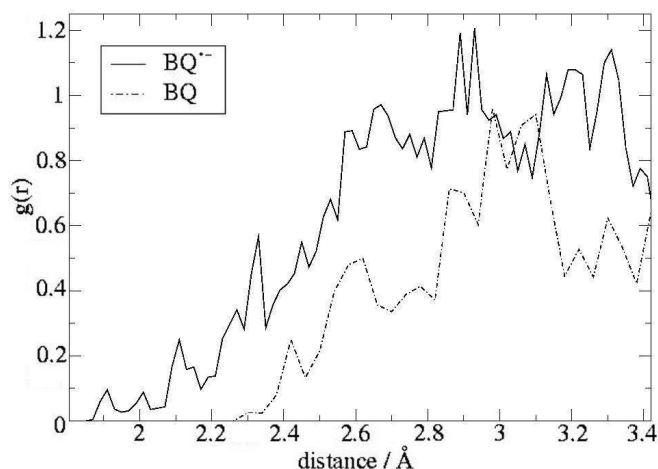


Figure 4.4: Radial distribution functions for water molecules engaging in T-stacking hydrogen bonding.

evidently very strong in both cases, and our counting procedure is essentially identical ($\pm 0.5\%$ or less) to integration of the RDF over the first solvation sphere, as was done in other works. (We discuss orientation of nearby water molecules more in Chapter 6, in comparison with ubisemiquinone.)

Raymond *et al.* performed an MM-MD simulation of aqueous BQ and BQ \bullet^- , and integrated over the first solvation sphere to about 2.7 Å.⁸⁷ Their results are similar to ours, but slightly smaller, for BQ; and for BQ \bullet^- , are significantly *larger* than ours, at 6.6 water molecules - 3.3 hydrogen bonds to each carbonyl oxygen. The RDF peaks for hydrogen bonding are at significantly lower distances than ours - 1.8 and 1.6 Å for BQ and BQ \bullet^- , respectively. We consider our results more reasonable, as our peak H-bond lengths are more in line with previous calculations^{79,85} and frozen ENDOR data.⁸⁰ The QM/MM simulations of Nonella *et al.* on BQ (in which all BQ \cdots H₂O interactions were modelled by a classical forcefield) give an RDF peak distance of 1.9 Å, which is quite close to our value.⁸² They found 3 water molecules within the first solvation sphere, which was taken to extend to 2.5 Å; this matches our simulation well, as we find 3.1 water molecules within 2.5 Å. This suggests QM/MM treats the mainly-electrostatic interactions between solvent and solute reasonably well, and it would be interesting to see the results of a QM/MM simulation on the aqueous BQ \bullet^- anion.

4.3.2 T-stacked H-Bonding

”T-stacked” hydrogen bonding to the π -system of semiquinones was previously proposed to occur on the basis of Raman studies of BQ \bullet^- in protic solvents⁸⁸ and computational analysis of EPR parameters of the Q_K site of Photosystem I.⁷⁷ MM-MD simulations of ubisemiquinone also found evidence of it - an accumulation of hydrogen atom density above and below the π -system,⁸¹ although it was not there described as ”hydrogen bonding”. Inspection of our simulations find that T-stacking hydrogen bonding occurs. Under the criteria mentioned in section 4.2, an average of 1.1 T-stacking hydrogen bonds are found. At any time, the number varies between 0 (quite a common situation - 23.9 % of the time) and 4 (extremely rare). Although the RDFs for this interaction, shown in Figure 4.4, are too noisy to extract much information from,^b we can see that the interaction of the π -system with solvent hydrogens is significantly stronger for BQ \bullet^- than for BQ.

The term ”hydrogen bonding” denotes an interaction with a degree of stability and directionality. We justify our use of the term on the following basis:

Precedent. Stable T-stacked hydrogen bonds have been found in static calculations of semiquinones.⁷⁷

Stability. Hydrogen bonding to the π -system can last for a significant fraction of a picosecond for BQ \bullet^- . The longest lifetime of a T-stacked H-bond in our trajectory was 578 fs.

Directionality. It is possible to quantify the degree of orientation of water molecules towards the π -system (or any other electron-rich system) by expressing the number of hydrogen bonds found as a fraction of the number found without angular criteria - i.e. the fraction of nearby water molecules whose closest hydrogens fit the angular criteria. We plot the degree of orientation against distance in Figure 4.5 for both the neutral and the anionic system. It can be seen that for the anionic system, nearby water molecules are significantly oriented towards the π -system from about 1.8 to 3.0 Å. For the neutral system, the orientation is weaker and only significant up to about 2.7-2.8 Å. (In Chapter 6 we will look further at the directionality of hydrogen bonding.)

Energy. According to previous static calculations, T-stacking hydrogen bonds to semiquinone anions can give an energetic stabilisation of up to 50

^bNoise afflicts the T-stacking RDFs far more than the RDFs for H-bonding to carbonyl oxygens because the interaction involved is far weaker. This makes for RDF structure that is less pronounced (as the peaks are broader) and lower RDF magnitude - both of which, combined, result in any interesting structure in the T-stacking RDF being almost entirely swamped in noise.

Table 4.4: Correlation of T-stacked and to-oxygen H-bond numbers for aqueous BQ \bullet^-

$n(\text{O}\cdots\text{H})$	$n(\pi\cdots\text{H})^{[a]}$
2	(0.51)
3	1.44
4	1.37
5	0.95
6	0.93
7	(0.75)

[a] Brackets indicate values we consider statistically unreliable due to low occurrence of that number of hydrogen bonds.

kJ/mol.⁷⁷ Our test calculations at the BP86//DZVP level found an energy of about 25 kJ/mol in the case of water and benzosemiquinone and an optimum C \cdots distance of 2.45 Å. We show the energy curve in Figure 4.6, superimposed on the T-stacked hydrogen bond RDF.

The T-stacking interaction is difficult to see in the 3-dimensional SDF plot in Figure 4.3. This is because T-stacking hydrogen bonds are few in number, but can come from a greater number of different directions than to-oxygen hydrogen bonds (there being 6 carbon nuclei to 2 oxygens). The density of hydrogen atoms H-bonded to the π -system is thus far more diffuse than the easily-visible donut-like density around the oxygens, and so more subject to noise. However, an accumulation of hydrogen density above and below the ring can be seen.

In Table 4.4, we list the correlation of T-stacked with to-oxygen hydrogen bonds. We see that the more hydrogen bonding there is to oxygen, the fewer T-stacked hydrogen bonds occur - to-oxygen hydrogen bonds stabilise negative charge on oxygen, making the π -system less attractive to hydrogen bonding.

4.3.3 Geometrical Properties

The C-O bond length is a very important geometric parameter. It is responsive to the dielectric constant of the solvent and degree of hydrogen bonding; it correlates, approximately linearly, with the C-O stretching frequencies (which are highly visible in the IR spectrum);⁸⁹ and it has a sizeable effect on the EPR properties of the semiquinone radical, which will be discussed in subsequent chapters. The average C-O bond lengths of our simulations may be seen in Table 4.5.

Unsurprisingly, BQ \bullet^- has longer $d[\text{C-O}]$ than the neutral BQ, both in the

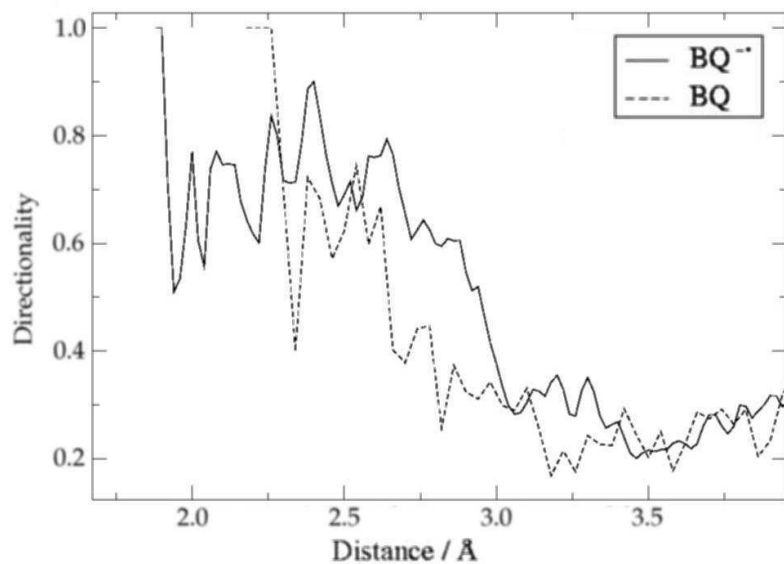


Figure 4.5: Degree of orientation of solvent hydrogens towards the π -system (number of T-stacked hydrogen bonds found at any given distance, as a fraction of the number obtained if the $\angle(\pi \cdots \text{H}-\text{O})$ criterion is relaxed).

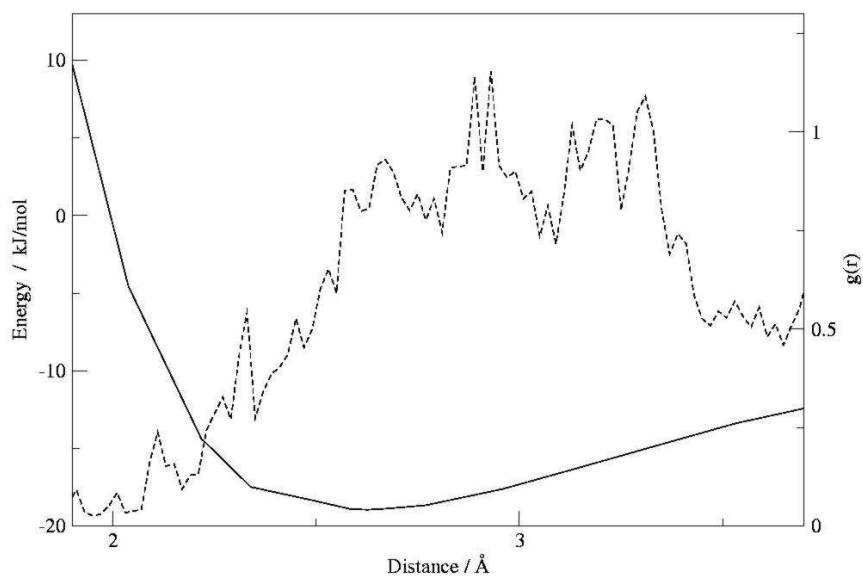


Figure 4.6: Potential energy well for single "T-stacked" hydrogen bond, calculated at BP86//DZVP level with counterpoise correction. See section 4.2 for more details. The T-stacking RDF is given as dotted line.

Table 4.5: Average CPMD trajectory structural parameters

	BQ		BQ ^{•-}	
	Solution	Gas-phase	Solution	Gas-phase
$d[\text{C-O}]/\text{Å}$	1.304	1.288	1.250	1.242
$d[\text{C-C}]/\text{Å}$	1.444	1.461	1.481	1.495
$d[\text{C=C}]/\text{Å}$	1.373	1.380	1.347	1.349

gas-phase and in solution. This is because the dominant mesomer for BQ is that with double C=O bonds, with a slight admixture of charge-separated resonance structures. BQ^{•-}, on the other hand, has a delocalised negative charge and unpaired electron, which - if either are located on an oxygen - result in a mesomer with a single C-O bond. This can also be explained in MO terms: the difference between BQ and BQ^{•-} is a single electron, located in the BQ LUMO (which becomes the SOMO of BQ^{•-}), which is C-O antibonding. The C-O bond is also longer in solution than in the gas-phase for both the neutral and the anionic systems. This is because the solvent, both by providing a polarisable dielectric continuum and by direct hydrogen-bonding to oxygen, stabilises negative charge at oxygen. This necessitates more single-bond character in the C-O bond. (This effect was noted in a previous study⁹⁰ which found that greater solvent polarity lengthens the C-O bond and increases the charge separation across it.) We see this in more detail in Table 4.2, in which the correlation between $d[\text{C-O}]$ and the number of hydrogen bonds is shown. Both for BQ and BQ^{•-}, the correlation is clear: the more hydrogen bonds exist to oxygen at any time, the longer the C-O bonds.

Curiously, T-stacked hydrogen bonds have the *same* effect on the neutral BQ, but the *opposite* effect (shortening the C-O bond) on the anionic BQ^{•-} (Table 4.2). For BQ^{•-}, this can be easily explained in terms of resonance structures. (See Figure 4.7 for resonance structures of BQ^{•-}.) T-stacked hydrogen bonds would encourage location of negative charge at a carbon nucleus. The possible resonance structures in this case have the unpaired electron on either oxygen or a neighbouring carbon, and so have either 1 or 2 C=O double bonds. If the negative charge were located at oxygen instead, however, there would be either 0 or 1 C=O double bonds. Thus, H-bonds to the π -system increase the double-bond character of the C-O bond, causing it to shorten.

It is not entirely clear why, in the case of the neutral system, T-stacked hydrogen bonds have the opposite effect. For the C-O bond to lengthen, the resonance structure with negative charge on carbon and positive charge on oxygen would have to be involved. This seems unlikely, especially given

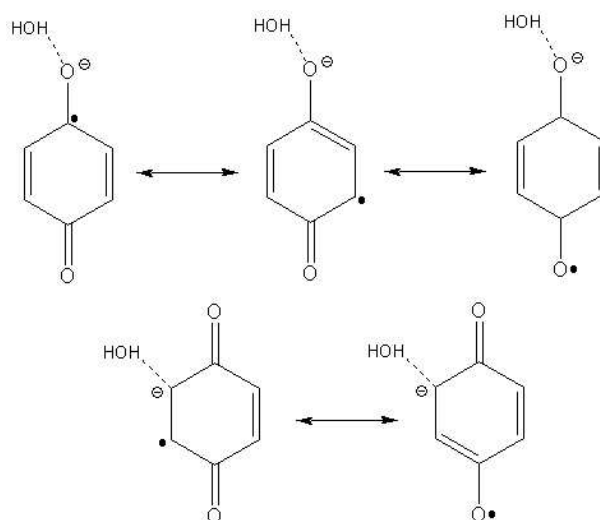


Figure 4.7: Resonance structures of benzosemiquinone radical anion: above, mesomers encouraged by to-oxygen H-bonding; below, mesomers encouraged by T-stacked H-bonding.

the weakness of the T-stacking interaction in the neutral case; the apparent effect is probably statistical noise.

We additionally note that the RMS deviation of $d[\text{C-O}]$ is higher for the solvated BQ system (0.028 Å) than for solvated BQ \bullet^- (0.016 Å). On the one hand, we would expect a higher RMS deviation for the anion because the C-O bond is weaker (having more single bond character); on the other hand, hydrogen bonding to oxygen is far more extensive in the anionic system, which would have a dampening effect on vibrational motion involving oxygen. However, if hydrogen bonding had such an effect, gas-phase BQ \bullet^- would surely show a far larger RMS deviation, whereas in fact it is even smaller (0.011 Å). This effect might be due to incomplete equilibration of the solvated BQ trajectory.

The carbon-carbon bonds are also strongly affected by reduction, although not as much by solvation. The C=C "double bond" ($C_{ortho}-C_{ortho}$) becomes more single bond-like, its length increasing by about 0.03 Å, on reduction from BQ to BQ \bullet^- . At the same time, reduction decreases the length of the C-C "single bond" ($C_{ortho}-C_{ipso}$) by a similar amount, making it more double bond-like. In MO terms, this is because the BQ \bullet^- SOMO is $C_{ortho}-C_{ortho}$ antibonding, but $C_{ortho}C_{ipso}$ bonding. In resonance structures, this is because BQ is dominated by the non-charge-separated structure, whereas for BQ \bullet^- , those mesomers become more important in which $C_{ortho}-C_{ortho}$ single bonds and $C_{ipso}-C_{ortho}$ double bonds occur.

Solvation decreases all carbon-carbon bond lengths, both for BQ and BQ^{•-}. The location of negative charge at a centre corresponds with mesomers with only single bonds to that centre; as solvation stabilises the presence of negative charge at oxygen, rather than any carbon atoms, it causes $d[\text{C-O}]$ to increase and the carbon-carbon bond lengths to decrease. Unfortunately the correlation between C-C bond lengths and specific numbers of hydrogen bonds is not strong enough to show through the statistical noise; however, we expect that in a significantly longer trajectory we would see to-oxygen hydrogen bonding shortening the C-C bonds, and T-stacked hydrogen bonding lengthening them.

For all bond lengths looked at, the change between the gas-phase and solution values is larger for BQ^{•-} than for BQ. This is because one resonance structure dominates the neutral system, which makes it less flexible; whereas the radical anion has a balance of resonance structures, with no one mesomer being significantly more stable than the others.

Experimentally, not much structural data is known for BQ^{•-} in aqueous solution. However, the C-O stretching frequency has an approximately linear relationship to the C-O bond length; the former is known,⁹¹ and has been used to infer from experiment a $d[\text{C-O}]$ value of 1.31 Å for benzosemiquinone.⁸⁹ This is close to our simulation's value of 1.304 Å.

4.3.4 Reliability of the MD simulations: Caveats

The methodology employed here should be sufficient for qualitative analysis of the effects of solvation and dynamics on semiquinone g -tensors. The BLYP/70 Ry level of theory is not expected to be perfect, but should reproduce the various influences and effects well enough to discourse upon. The errors involved in using a BLYP wavefunction to calculate the MD forces are not expected to approach the magnitude of the errors involved in EPR property calculation, in any case.

A more serious problem is the trajectory length. In MM-MD, giant protein structures can be simulated for entire nanoseconds; to the *ab initio* molecular dynamicist, this is an unimaginable luxury (or complete overkill). We believe that 6 ps is sufficient in the case of BQ^{•-}, both gas-phase and in solution, to obtain a good dynamic estimate of the EPR parameters, and we will return to this in the next chapter. Due to budget constraints, however, the neutral BQ system could only be simulated for about 2 ps (its simulation being of lesser priority anyway). The shortness of the simulation length shows itself in the following anomalies.

As mentioned above, the RMS deviation of the C-O bond length is far higher for aqueous BQ than for aqueous BQ^{•-}, which probably arises from

insufficient equilibration of energy among the various vibrational modes. (In particular, it is possible that poor equilibration of very low-frequency librational motion is significant here.) A similar problem arises in the out-of-plane angles of the carbonyl groups (a property that will be brought up in the next chapter).

It is surprising that the 3/1 hydrogen bonding configuration is more common than 2/2, and very surprising that 1/0 is more common than 2/0, for benzoquinone. This is almost certainly due to the simulation not being long enough to properly sample all the possible hydrogen bonding simulations. It is possible that this is also the reason for T-stacked hydrogen bonding apparently increasing the C-O bond length for aqueous BQ.

The neutral BQ simulations are still of value in spite of this, as there are certain trends that show themselves very clearly - the lesser extent of hydrogen bonding to the molecule (both to oxygen and to the π -system), the correlation of C-O bond length with the number of hydrogen bonds, and the marked differences of bond lengths compared to BQ $^{\bullet-}$.

Although the trajectory length problem is less drastic for BQ $^{\bullet-}$, it would be desirable to run a significantly longer simulation to get better data on hydrogen bonding. The correlation of $d[\text{C-O}]$ with the number of hydrogen bonds is imperfect - it decreases from 3 to 4 - and this would, we believe, resolve itself if the simulation was twice the length. Additionally, we would gain more information on the rarer hydrogen bonding configurations, for instance those with 4 water molecules to one oxygen, whose data we must currently regard as too statistically unreliable to discuss.

Addendum: BQ $^{\bullet-}$ +5H₂O Calculation

Attempts to optimise the BQ $^{\bullet-}$ +5H₂O system result in an arrangement with hydrogen bonds from water to BQ $^{\bullet-}$ and 1 water-water H-bond. We have found no local minimum in which 5 hydrogen bonds between water and BQ $^{\bullet-}$ exist. The reason for this is the high lewis-basicity of the water oxygens, which have no hydrogen bonds directed to them - unlike BQ $^{\bullet-}$, which has several. It therefore makes energetic sense to swap a H \cdots BQ $^{\bullet-}$ bond for a H \cdots OH₂. However, when there are only two H-bonds to a carbonyl oxygen, the water molecules are too far away from each other for this to take place, and the carbonyl oxygen sits between them. If there are 3 H-bonds to one carbonyl oxygen, however, the water molecules are close enough to interact and rearrange: the unattached hydrogen of one water swivels and is drawn towards the oxygen lone pair of another water and forms a new hydrogen bond, with the old one to BQ $^{\bullet-}$ breaking.

We obtained an approximate $\text{BQ}^{\bullet-} + 5\text{H}_2\text{O}$ structure not by optimising to an energy minimum but by locating a saddle-point. If the local environment around a carbonyl oxygen has mirror symmetry - e.g. 2 hydrogen bonds roughly in-plane, one perfectly out-of-plane hydrogen bond - the rearrangement of hydrogen bonds cannot take place because it would break symmetry (i.e. with regard to rearrangement, the system perches on a maximum in the potential well, rather than sitting in a minimum). However, the out-of-plane H-bond, or 2 in-plane H-bonds, *could* dissociate without breaking symmetry. As it happened, optimisation yielded 5 stable hydrogen bonds, albeit with the out-of-plane H-bond slightly longer than the others. This indicates that the problem with forming more than 4 H-bonds in static calculations is not that a 5th H-bond is unstable, but that solvent molecules beyond the 1st solvation sphere are omitted. Because the water molecules have no hydrogen bonds to them, their oxygen lone-pairs are too lewis-basic, causing rearrangement of the 5th water- $\text{BQ}^{\bullet-}$ H-bond to a water-water H-bond.

Chapter 5

Dynamical EPR Parameters of Benzosemiquinone^{66, 67, 92}

5.1 Semiquinone EPR

As semiquinone anions are paramagnetic, EPR is a valuable tool for probing their interaction with the surrounding environment.^{71, 72} The EPR parameters of semiquinones - g - and hyperfine coupling-tensors - are highly sensitive to interactions with the solvent, and particularly to the extent of hydrogen bonding to the molecule. This is especially important as the hydrogen bonding situation at the protein binding site also affects the redox potential of the Q/Q^{•-} couple, stabilising the anion (which is more receptive to hydrogen bonds - see Chapter 4).

5.1.1 Theoretical analysis of semiquinone EPR

Interpretation and augmentation of semiquinone EPR by quantum chemical calculations goes back to the 1950s. The discovery of ¹H hyperfine couplings for in-plane hydrogens of organic π -radicals, including semiquinones,⁹³⁻⁹⁹ raised the question of how an unpaired electron could have density at a nucleus in the nodal plane of the SOMO. McConnell¹⁰⁰ and Bersohn¹⁰¹ used molecular orbital (MO) calculations to demonstrate that σ -bonds could be spin-polarised by a nearby unpaired electron. Several papers were devoted to constructing or calibrating an empirical theory of semiquinone hyperfine coupling constants, by way of which atomic π -electron spin densities could be derived from hyperfine coupling constants.¹⁰²⁻¹⁰⁷

In more recent times, the computational resources and techniques available to theoretical chemists have increased, to the point where more sophisticated and expensive approaches have replaced empirical or semiempirical

methods of deriving HFCs. DFT is a very useful tool in this regard, and in particular, the hybrid density functional B3LYP gives good results when combined with the specialised EPR-II basis set.⁸³

Benzosemiquinone, as a comparatively simple, stable member of an important class of organic radicals, has frequently been used as a test case for theoretical g -tensor calculation. The first such case was the work of Hales,¹⁰⁸ using a sum-over-states (SOS) formalism to calculate the "paramagnetic" part of the g -shift from electronic orbitals calculated using the semi-empirical INDO method. (The formalism itself was developed by Stone, who made a semiempirical analysis of hydrocarbon and semiquinone radical g -shifts.¹⁰⁹ Stone's work predicted that the dominant oxygen contribution to the g -shift would be nearly proportional to the spin density at oxygen; this was later demonstrated using $\rho_O^{\alpha-\beta}$ extracted from hyperfine data.¹¹⁰) The theory was later updated to include gauge and relativistic mass corrections,¹¹¹ and again applied to benzosemiquinone using semiempirical electronic structures.^{89,112}

In recent years, non-SOS-based approaches to calculation of the g -tensor have been applied to benzosemiquinone, such as Coupled-Perturbed Kohn Sham (CPKS)¹¹³ and a 2-component perturbational approach;¹¹⁴ while increased computational resources have made it possible to derive the g -tensors of BQ \bullet^- from electronic structures computed either at the DFT level or using wavefunction-based methods. Hartree-Fock (HF) performs significantly *worse* than the best semiempirical calculations, with restricted open-shell (RO) HF (using SOS) underestimating Δg_x and Δg_y ,¹¹⁵ and unrestricted (U) HF calculations (using CPKS) overestimating both components.⁸⁶ Non-relativistic density functional theory, on the other hand, performs reasonably well, with high accuracy in the g_y and g_z components, while the sensitive g_x component is generally overestimated (both SOS^{85,90} and CPKS^{79,86} approaches deliver similar results here). Relativistic 2-component DFT has been performed in an RO framework, and performs similarly apart from overestimating g_x more drastically.¹¹⁶ We collect the results from all these various methods in Table 5.1.

To the best of our knowledge, no post-Hartree Fock approaches to g -tensor calculation have yet been applied to semiquinone radical anions. However, MCSCF calculations have been used to calculate the g -tensor of the similar phenoxy radical, with reasonable accuracy.¹¹⁵

Semiquinone EPR parameter calculations are useful for interpreting experimental results and validating conjectures concerning the *in vivo* environment of a semiquinone anion: theoretical calculation allows comparison of experimental data with simulated model systems and systematic analysis of the effects of specific intermolecular interactions (or conformational effects) on EPR parameters. In this manner, the existence of T-stacking

Table 5.1: Previous results for quantum mechanical static-structure calculation of the BQ^{•-} g -tensor

g -Tensor	Level of theory	System	g -shift / ppm		
	Ψ		Δg_x	Δg_y	Δg_z
SOS ^[a]	INDO ^[b]	Gas-phase	3600	1400	0
		Solvated	4000	1500	0
+ $\Delta g_{GC}, \Delta g_{RMC}$ ^[c]	MNDO/PM3 ^[d]	Gas-phase	4600	3000	-100
		+8MeOH	4300	2900	-200
+ $\Delta g_{GC}, \Delta g_{RMC}$ ^[e]	AM1	Gas-phase	4020	2920	-170
	PM3	Gas-phase	4490	3330	-180
	MNDO	Gas-phase	4230	3260	-200
+ $\Delta g_{GC-1e}, \Delta g_{RMC}$ ^[f]	ROHF	Gas-phase	2100	2200	200
+ $\Delta g_{GC-1e}, \Delta g_{RMC}$ ^[g]	UBP86 ^[h]	Gas-phase	6530	3065	-20
		+PCM	6024	2964	-27
		+4H ₂ O	4889	2935	2
		+4H ₂ O/PCM	4787	2906	-23
CPKS ^[i]	UHF ^[j]	Gas-phase	7150	4770	-150
	UB1LYP	Gas-phase	6740	3540	-180
		+4MeOH	4750	3160	-140
CPKS ^[k]	UB3LYP ^[l]	+4H ₂ O	5200	3200	-100
		+20H ₂ O	4600	3200	-100
DKS ^[m]	DK-ROBP86 ^[n]	Gas-phase	9070	3620	-300
		+4H ₂ O	6700	3430	-260
		+4MeOH	6260	3550	-280
Experimental ^[o]		(H ₂ O)	4180	2980	-20
Experimental ^[b]		(MeOH)	4200	3000	00

[a] Baseline Sum-Over-States method for calculation of paramagnetic component. Refs. 109,117 [b] Ref. 108 [c] Ref. 111 [d] Ref. 89 [e] Modifications to method and applications in ref. 89 [f] Modifications to method and applications in ref. 115 [g] Refs. 27,28 [h] Ref. 90 [i] Coupled-Perturbed Kohn Sham, a non-SOS method. Ref. 113 [j] Ref. 86 [k] CPKS¹¹³ with parameterised 1-electron spin-orbit interactions.¹¹⁸⁻¹²⁰ [l] Ref. 79 [m] Dirac-Kohn-Sham-based perturbational scheme. Ref. 114 [n] Douglas-Kroll (2-component) Restricted Open-shell DFT using the BP86 functional. Ref. 116 [o] Ref. 80

hydrogen bonds to phyllosemiquinone in PS-I was deduced,⁷⁷ and insight into the hydrogen bonding situation of ubisemiquinone in bacterial reaction centre was obtained by extensive and rigorous modelling.¹²¹ The value of computational modelling is also testified to by a number of combined experimental/theoretical papers, which use EPR property calculations to interpret the empirical data they present.^{80,122-125}

5.2 Computational Details

EPR calculations were performed on both solvated and the gas-phase benzosemiquinone radical anion, using structures extracted every 40 snapshots (every 6.8 fs) from the trajectories whose calculation was detailed in Chapter 4. The solvated system poses the question of which water molecules to include in the extracted structure. In order to assess the effects of solvent-solute interactions on the EPR parameters, we defined molecular clusters around BQ^{•-} including all water molecules fulfilling certain conditions (see previous chapter for hydrogen bond criteria):

- **[lone]** indicates BQ^{•-} molecule alone, *sans* solvent molecules.
- **[O[⋯]H]** includes all water molecules hydrogen bonded to carbonyl oxygens. [O(1)[⋯]H] or [O(2)[⋯]H] denote water molecules hydrogen bonded to one *specific* carbonyl oxygen. (Formally, the molecule is symmetric and it should make no difference. In practice, a difference arises because of the finite trajectory length.)
- **[T-stacked]** includes all water molecules engaging in T-stacking hydrogen bonding.
- **[O,C[⋯]H]** includes all water molecules engaging in any hydrogen bonding to BQ^{•-}.
- **[x Å]** includes all water molecules within x Ångstroms. For g -tensors, this is defined as distance from an oxygen or ring carbon only. For HFC calculations, this is defined as distance from carbonyl oxygen only.^a

The electronic structure for each snapshot was calculated at the UDFT level using the TURBOMOLE program package (version 5.6).^{126,127} For g -tensors, the SCF calculation was performed at the UBP86//DZVP level.^{17,21,57}

^aDefining distances from oxygen only results in a smaller number of water molecules included for a given distance. For the case of HFCs, we chose to trade off the difference for a larger distance, to get a more complete solvation sphere for the water molecules H-bonded to carbonyl.

The RI approximation was used to speed up the calculations, with density fitting by an SVP auxiliary basis sets.¹²⁸ (Test calculations indicated that using RI-DFT had a negligible effect on the g -tensors.) Tight SCF convergence criteria were used - energy 10^{-9} a.u., density 0.5×10^{-8} a.u. For hyperfine coupling tensors, the calculation was performed at the UB3LYP//EPR-II level.^{17, 18, 25, 30} The SCF energy convergence criterion was set to 10^{-8} . Some calculations employed a Conductor-like Polarizable Continuum Model (CPCM, or PCM):¹²⁹ this was carried out using the COSMO module of the TURBOMOLE package, using default values for r_{solv} and $\epsilon = 77.8$.

The magnetic resonance parameters were calculated from the converged electronic structures using the MAG (magnetic resonance) module of the program ReSpect.⁶¹ See Chapter 2 for an outline of the theoretical methodology. The gauge origin was located at the midpoint between the carbonyl oxygens for all calculations, although test calculations indicated that gauge-dependence was essentially negligible (on the order of a few ppm).

When we present tensor components for both g - and A -tensors, unless otherwise stated these are the trajectory-averaged values of the individual components, obtained for each snapshot by diagonalising the tensor for that snapshot. We identify the components by magnitude, which is sufficient to distinguish the g -tensor components from one another, and the A_{\parallel} from the two A_{\perp} components. For certain quantities we also compiled the trajectory-averaged tensors, which we transformed at each snapshot to a coordinate system defined by the principal axes of inertia of the BQ \bullet - molecule. The point of this is that the principal axes of the parameter tensors may vary in direction from snapshot to snapshot (as seen from the molecular reference frame); hence, when discussing the instantaneous principal components, we are thinking in a fluctuating frame of reference. However, if we diagonalise the trajectory-averaged tensor, we obtain the average principal components as seen from an unchanging frame of reference, which we have defined to exclude molecular rotation. (This is the frame of reference assumed by experimental tensor data, where molecular rotation is inhibited by the system being in the solid state.)

These two ways of determining the components - averaging the instantaneous values of the components against averaging the tensor, then diagonalising - will differ according to how variable the direction of the instantaneous principal axes is. If the principal axes of a given tensor always point in the same direction, there will be no difference. If two axes always lie in a certain plane but do not always point in exactly the same directions, the diagonalised average tensor will show a smaller difference between their respective components than the average instantaneous values of the two components. (If the two axes rotate freely, or if all three do, the respective components will not

differ at all - as in liquid state MR experiments, where molecular rotation permits only the isotropic values to be extracted.)

5.3 g -Tensor calculations

In order to determine the size of the BQ \bullet -H₂O cluster needed to obtain converged results (i.e. the size at which the g -tensors would not change on inclusion of more water molecules, and could thus be regarded as essentially in bulk solution), we carried out calculations using multiple cluster sizes for about 1.7 ps (250 snapshots). The results are shown in Table 5.2. The 4.5 Å cluster was effectively the limit of computational feasibility, and we calculated g -tensors for it both with and without PCM. The inclusion of PCM decreases the g_x component by 100 ppm, indicating that the polarisable dielectric effects of the bulk solvent beyond 4.5 Å still have a noticeable, but small, effect on the electronic structure. With PCM applied, going from 3.5 Å to 4.0 Å to 4.5 Å clusters shows an asymptotic decrease to some bulk value. Assuming exponential decrease and extrapolating to infinity, we find [4.5 Å+ PCM] to be converged within 10 ppm on all components, and [4.0 Å+ PCM] to be converged within 40 ppm - a deviation smaller than the precision to which the experimental values are given.⁸⁰ (Test calculations on 5.0 Å clusters were performed for a few snapshots, and these deviated negligibly from the 4.5 Å results.) We then calculated g -tensors for the full 6.3 ps trajectory, and present these also in Table 5.2.

As found in previous calculations,^{79,85,86,90,116} the hydrogen bonding situation has a large effect on the g_x component, which is the most sensitive to environmental influences and changes in geometry. The changes in the g_y component are much smaller, but are generally parallel to those in g_x . The g_z component is very small, changes little (it varies only by 130 ppm, compared to hundreds of ppm for g_y and thousands for g_x) and the trends in it do not mirror those in the other two components.

It is known that hydrogen bonding to carbonyl oxygens decreases Δg_x , and specifically the SO/OZ contribution to it, by (a) reducing the spin density on carbonyl oxygens⁹⁰ (which will decrease the integral numerator in the expression for $\Delta g_{SO/OZ}$ - see equations 2.5-2.7) and (b) increasing the HOMO-SOMO energy gap (which forms the denominator in equation 2.5; a similar effect is seen in MCSCF studies of the phenoxyl radical¹³⁰). Inspection of short periods of the trajectory confirms this. Both hydrogen bonding to carbonyl, and the dielectric effect of the solvent, stabilise negative charge at oxygen, pushing spin density onto the C₆ ring (mostly onto the *ipso* carbons, as described in the next section). The HOMO-SOMO gap increases

Table 5.2: calculated *g*-shift tensors (in ppm)

Cluster model	Δg_{iso}	Δg_x	Δg_y	Δg_z
BQ ^{•-} _{aq} (full trajectory):				
[lone]	3803	8000	3335	78
[O(1)⋯H]	3530	7307	3191	93
[O(2)⋯H]	3500	7205	3186	111
[O⋯H]	2959	5651	3045	181
[T-stacked]	3896	8195	3400	94
[O,C⋯H]	3039	5794	3115	208
[4.5 Å]	2779	5159	2992	189
[4.0 Å + PCM]	2757	5123	2976	174
BQ ^{•-} _{aq} (partial trajectory):				
[4.5 Å]	2735	5025	2985	195
[3.5 Å + PCM]	2751	5072	2998	184
[4.0 Å + PCM]	2695	4954	2958	175
[4.5 Å + PCM]	2680	4924	2945	175
[bulk limit] ^[a]	2675	4914	2939	175
Gas-phase BQ ^{•-} :	3357	6755	3240	79
Exp. (± 50 ppm) ^[b]	2380	4180	2980	-20

[a] Extrapolated from [x Å + PCM] results to infinite distance. [b] Experimental data from 90 K frozen aqueous solution.⁸⁰

because the HOMO is lone-pair-like at oxygen, and is stabilised by in-plane hydrogen bonding (and hydrogen bonding tends to be more in-plane than not, as described in the previous chapter).

T-stacking interactions have the opposite effect - they stabilise charge on the C₆ ring, pushing spin density onto the carbonyl oxygens. Furthermore, they stabilise the out-of-plane SOMO, decreasing the HOMO-SOMO gap. Both of these factors lead to an *increase* in g_x . (Out-of-plane hydrogen bonding to carbonyl oxygen also has the effect of decreasing the HOMO-SOMO gap, so that they either increase or do not much decrease g_x .) However, because T-stacking interactions are weaker and fewer in number, their effect on the *g*-tensor is a lot smaller. Comparing the values for the [O(1)⋯H] and [O(2)⋯H] clusters against the [lone] value, hydrogen bonding to only one carbonyl oxygen decreases g_x by about 750 ppm. Hydrogen bonding to both ([O⋯H]) gives a massive decrease, over 2000 ppm. In contrast, T-stacked H-bonds increase g_x by only about 200 ppm. When both hydrogen bond types are combined (the [O,C⋯H] cluster), the dominant effect is that of to-oxygen hydrogen bonding.

Solvation spheres beyond the first have a nonnegligible effect - going from $[\text{O}, \text{C}\cdots\text{H}]$ to $[4.5 \text{ \AA}]$ or $[4.0 \text{ \AA} + \text{PCM}]$, g_x decreases by over 600 ppm. This arises because solvent molecules further out have a dielectric effect on the benzosemiquinone, and also form hydrogen bonds with the water molecules directly H-bonded to $\text{BQ}^{\bullet-}$. These will mostly be hydrogen bonds involving the lone-pairs of the water molecules of the first solvation sphere (which have 2 lone-pairs and only one hydrogen free for H-bonding), and will make the first solvation sphere water molecules more electropositive, increasing the strength of $\text{BQ}^{\bullet-}\cdots\text{H}_2\text{O}$ interactions. Application of PCM can simulate the dielectric effects of a continuous bulk solvent, but not the knock-on effects of discrete hydrogen bonds. Overall, the effect of further solvation spheres is far smaller than that of the first solvation sphere, however; and the $[\text{O}, \text{C}\cdots\text{H}]$ cluster recovers over 75% of the effects of the bulk solvent on the g -tensor.

We have additionally correlated the $[4.0 \text{ \AA} + \text{PCM}]$ g -tensor values with different hydrogen bonding situations, as was done with the C-O bond lengths in the previous chapter. The results are shown in Tables 5.3 and 5.4. The trends clearly reflect the effects already remarked upon: the higher the number of hydrogen bonds to oxygen, the lower Δg_x and Δg_y , whereas T-stacked hydrogen bonds have the opposite effect. In Table 5.4 we also see that asymmetric hydrogen bonding has less effect on the g -tensor than symmetric: the $[4.0 \text{ \AA} + \text{PCM}]$ value of g_x is 65 ppm lower for $[2/2]$ than for $[3/1]$. We saw this also comparing the trajectory averages for the clusters $[\text{O}(1)\cdots\text{H}]$, $[\text{O}(2)\cdots\text{H}]$ and $[\text{O}\cdots\text{H}]$. Hydrogen bonding to one end only decreases g_x by about 750 ppm, but to both ends, decreases g_x by over 2000 ppm - the changes in g_x are nonadditive, with symmetric hydrogen bonding having a 50% larger effect than would be predicted by adding together the effects of bonding asymmetrically to each individual carbonyl oxygen.

5.3.1 The effect of the C-O bond length

The effects talked of above, of hydrogen bonding changing the spin density distribution and hence the g -tensor, constitute the *direct* effects of hydrogen bonding. However, the g -tensor is also influenced by the geometry,¹¹⁵ and in particular the C-O bond length. Hydrogen bonding can therefore have an *indirect* effect on the g -tensor by altering the molecular geometry.

It is known that the C-O bond length strongly affects the g -tensor. We see a striking result of this if we examine the time-variation of the g -shift components: the stretching and contraction of the C-O bond due to vibrational motion shows up in the g_x component (and, more weakly, in g_y) as strong, regular oscillations, of period approximately 30 fs. (This is seen most clearly if we plot the time derivatives of g_x and the average of the to C-O bond

Table 5.3: Variation of Δg with hydrogen bonding situation (total H-bond number).

H-bond number	% occ.	BQ ^{•-} , [4.0 Å + PCM] ^[a] [lone] ^[a]			
		Δg_x	Δg_y	Δg_z	Δg_x
Hydrogen bonds to oxygen					
2	1.7	(5259)	(3050)	(97)	(7596)
3	6.4	5650	3058	150	8062
4	32.2	5277	2970	169	7933
5	43.6	5058	2966	168	8060
6	15.1	4767	2962	212	7995
7	1.0	(4764)	(3100)	(281)	(7926)
T-stacked hydrogen bonds					
0	23.9	4980	2946	172	8013
1	50.4	5069	2973	178	8026
2	17.4	5359	2995	151	8048
3	8.2	5370	3038	197	7845
4	0.3	(5319)	(2877)	(241)	(7681)

[a] Brackets indicate low-frequency hydrogen bonding situations; data for these may be unreliable.

Table 5.4: Variation of Δg with to-oxygen hydrogen bonding situation (H-bond configuration).

H-bond configuration	% occ.	BQ ^{•-} , [4.0 Å + PCM] ^[a]		
		Δg_x	Δg_y	Δg_z
[1/1]	1.6	(5240)	(3050)	(92)
2/0	0.0	(5538)	(3053)	(183)
2/1	6.4	5650	3058	150
2/2	25.2	5263	2961	175
3/1	6.9	5328	3005	145
3/2	42.2	5061	2965	169
3/3	15.1	4761	2964	213
4/1	1.4	(4954)	(3001)	(154)
4/2	0.2	(5628)	(3075)	(162)
4/3	0.9	(4764)	(3100)	(281)

[a] Brackets indicate low-frequency hydrogen bonding situations; data for these may be unreliable.

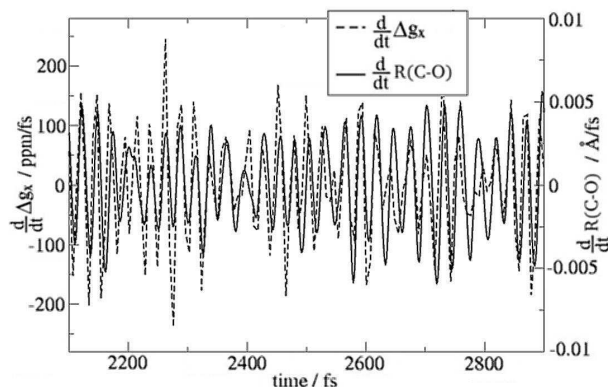


Figure 5.1: Time-derivatives of Δg_x and $d[\text{C-O}]$.

lengths, as in Figure 5.1.) The correlation is positive - the greater $d[\text{C-O}]$, the larger g_x . This is partly because a longer C-O bond encourages resonance structures with either charge or spin located on the oxygen; but the effects also have to do with the orbital energies. The characteristic oscillation also shows up in the energy of the SOMO, but not of the HOMO. This is because the SOMO is C-O antibonding, and thus stabilised by a longer C-O bond, whereas the HOMO is virtually nonbonding across the C-O bond; its character is C_{ipso} - C_{ortho} σ -bonding and lone-pair like at oxygen. Hence, the energy gap between the orbitals decreases on elongation of the C-O bond, increasing the $\Delta g_{SO/OZ}$ contribution to the g -shift (recall Equation 2.5, where this energy gap serves as denominator).

As our simulations show that $\text{BQ}^{\bullet-}$ has a 0.016 Å longer C-O bond in solution than in the gas-phase, we would expect to see the effects of this if we compare the g_x values for gas-phase and [lone] calculations. Indeed, the [lone] value of Δg_x is over 1000 ppm higher than for the gas-phase, and Δg_y is also about 100 ppm higher. However, we would also expect a clear positive correlation between the [lone] Δg_x value and the number of hydrogen bonds to oxygen at a given time, but no such trend is apparent in the data in Table 5.2. We assume that the correlation is obscured by statistical noise, and that a longer trajectory would show the trend plainly.

We would also expect an opposite trend with T-stacked hydrogen bonds - that they would shorten the C-O bond length (which they do - see previous chapter) and hence decrease g_x for the [lone] calculations. However, the data (as shown in Table 5.3) seems to indicate the reverse, implying an *opposite* trend in the relation of $d[\text{C-O}]$ to g_x , which we have no good explanation of.

5.3.2 On the *z* component

The positive values we get for Δg_z are curious. For a planar π -radical, the *g*-tensor component perpendicular to the ring should consist entirely of the "diamagnetic" Δg_{GC} and Δg_{RMC} terms, which together are small and overall negative; there should be no paramagnetic contributions at all. Static calculations tend to give the expected small, negative values,^{85,90} in agreement with experiment;⁸⁰ our dynamic calculations do not, for any cluster definitions.

The obvious implication is that our Δg_z values gain a small SO/OZ contribution by loss of planarity, with bending of the C-O groups out of the plane of the ring being probably most important. That the dynamic system *should* lose planarity is obvious - except at very low temperatures, some thermal energy will go into ring-bending motion; static calculations, essentially done at absolute zero, cannot account for this. The discrepancy with experiment is also explained by this, as tensor data requires a very low temperature.

Inspecting our trajectory, it does seem that the motion of the C-O groups is an important factor, and specifically the "2-bond angle" between the two C-O bond vectors. When this angle is around 180° - that is, the two C-O bonds point in directly opposite directions - we see low values of g_z ; and spikes in Δg_z tend to arise when the 2-bond angle drops, due to both C-O bonds pointing out-of-plane in the same direction (generally up or down in the *z* direction). An example of this is shown in Figure 5.2, in which the 2-bond angle is only 152°, and the hydrogen bonding is strongly out of plane. The [lone] value for Δg_z in this case is 278 ppm; if one-sided hydrogen bonding is included in the calculation, this rises to 354 or 429 ppm. If all hydrogen bonds are included in the calculation, the Δg_z value climbs to a remarkable 782 ppm. We see here that, as with Δg_x , the changes effected by hydrogen bonds to oxygen are nonadditive, with symmetric H-bonding having the most effect. If further solvation shells are included, the value drops somewhat, with the [4.0 Å + PCM] cluster showing $\Delta g_z = 571$ ppm. We assume that the strongly out-of-plane hydrogen bonding helps to distort the ring, in snapshots like this; which possibly explains why, of all the H-bonding configurations, the ones with the largest Δg_z values are [3/3] and [4/3] - configurations which require heavily out-of-plane hydrogen bonding.

To explain the way out-of-plane C-O groups have this effect, we note again that the dominant contribution to $\Delta g_{SO/OZ}$ is spin-orbit coupling around the oxygens, which are the heaviest atoms. Each oxygen is covalently bound only to one other atom, namely the adjacent *ipso*-carbon. Hence, the local electronic structure at oxygen will orient itself relative to that carbon. This means that any response property of the electronic structure around oxy-

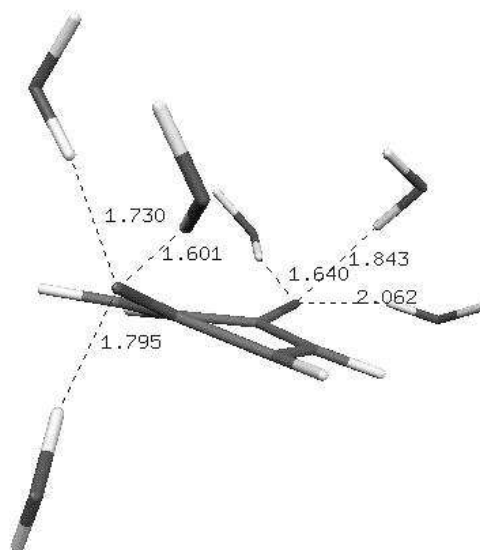


Figure 5.2: A heavily distorted structure with strongly out-of-plane hydrogen bonding and large Δg_z .

gen will share this orientation - including contributions to the g -tensor. In particular, each oxygen's contribution will have its own "local" large (Δg_x) component whose principal axis points along the C-O bond. When the 2-bond angle is 180° , the "local" axes of the two oxygens and their g -tensor contributions will coincide with each other and with the axes of the "global" g -tensor. However, if the C-O groups are bent out of plane, the "local" large (x) axis of each oxygen lies partly along the "local" small (z) axis of the other. This necessarily leads to the "local" Δg_x contributions pointing partly in the "global" z direction.

However, there are clearly other contributions at work. For this snapshot, and for the trajectory on the whole (see Tables 5.2 to 5.4) to-oxygen H-bonding increases Δg_z , compared to the [lone] value, while *decreasing* Δg_x - which does not fit with the idea of positive Δg_z values arising from "local" Δg_x components. We currently have no explanation of what additional effects might be in play here; it will require further close examination to resolve. We note as well that both types of H-bond - T-stacked and to-oxygen - have the effect of increasing Δg_z , while further solvation spheres decrease it; whereas for Δg_x and HFC data (see later) the two H-bond types tend to have opposite effects.

The Δg_z component for the gas-phase anion does not differ particularly from the [lone] value, despite a greater deviation from planarity (the 2-bond

angle averages 163° in the gas-phase and 170° in the liquid state). This can be accounted for, insofar as Δg_z arises from "local" Δg_x contributions, by the fact that the C-O bond is shorter in the gas-phase. This decreases "local" Δg_x contributions compared to [lone] (as seen from the "global" Δg_x value of each).

5.4 Hyperfine Coupling

The calculated HFC constants and largest dipolar coupling components are listed in Tables 5.5 and 5.6, with values presented for a range of cluster criteria. (Note that the x Å distance criterion here refers to distance from O only, rather than from O or C. This was done to provide the water molecules H-bonded to carbonyl oxygen with as large a solvation sphere as possible.) Dipolar coupling occurs through space and has an r^{-3} dependence; for O and C, it is dominated by the spin density near the nucleus in question; for ring H, the spin density around that atom is so small that the dipolar coupling depends on the spin density at the adjacent nucleus. A_{iso} is proportional to the spin density at the nucleus in question. This spin density arises, in the static calculations, entirely from spin polarisation - the SOMO has a node in the plane of the molecule, and has no density at any nucleus. (In the dynamic calculations, the SOMO might have some small density at the nuclei, but spin polarisation remains dominant.) Spin polarisation can be positive or negative. Positive spin polarisation is caused by spin density at the same nucleus, and occurs by way of the 1s and 2s orbitals. Negative spin polarisation is caused by spin density at an adjacent nucleus, and occurs by polarisation of the σ -bond. Spin polarisation's effects on the Mulliken spin densities are small, and generally obscured by other trends in the spin density.

For oxygen, positive spin polarisation is most important, as oxygen has the most spin of any nucleus in the molecule. For the carbon atoms, a balance of effects is seen - when significantly more spin is located at an adjacent nucleus than at the nucleus in question, negative spin polarisation (via C-O or C-C bonds) dominates, and A_{iso} is negative; when the spin at the nucleus in question is close to, or exceeds, that at the adjacent nucleus, A_{iso} becomes positive. For ring hydrogens, where the SOMO has negligible density, only negative spin polarisation (of the C-H bond) is important.

Table 5.5. HFC data (MHz) and Mulliken spin density (SD) data [a.u.] for benzosemiquinone radical anion (hydrogen and oxygen nuclei)

Ring ^1H		A_{iso}	A_{parr}	SD x 10^3
CPMD	Gas-phase	-6.55	5.6	-5.21
	[Lone]	-6.16	5.4	-4.80
	[C \cdots H]	-6.18	5.4	-4.81
	[O \cdots H]	-5.98	5.8	-4.50
	[O,C \cdots H]	-6.01	5.8	-4.53
	[Lone+PCM]	-6.11	5.5	-4.53
	[O \cdots H+PCM]	-5.94	5.8	4.35
	[O,C \cdots H+PCM]	-5.96	5.8	-4.38
	[4.25 Å + PCM]	-5.93	5.9	-4.39
$\sigma(A)^{[a]}$	[4.25 Å + PCM]	0.19		
Static calcs.	Gas-phase ^[b]	-6.7	5.5	
	BQ \bullet^- + 4H ₂ O ^[c]	-6.2	5.9	
	BQ \bullet^- + PCM ^[d]	-6.3		
	BQ \bullet^- + 4H ₂ O + PCM ^[b]	-6.4	5.8	-4.67
	BQ \bullet^- + 5H ₂ O + PCM ^[b]	-6.3	5.8	-4.58
Experimental		-6.6 ^[e]	6.2 ^[f]	
<hr/>				
^{17}O		A_{iso}	A_{parr}	SD
CPMD	Gas-phase	21.35	83.3	0.27
	[Lone]	22.43	88.9	0.29
	[C \cdots H]	22.44	89.1	0.29
	[O \cdots H]	19.86	74.2	0.24
	[O,C \cdots H]	19.95	75.1	0.24
	[Lone+PCM]	21.83	82.2	0.27
	[O \cdots H+PCM]	19.43	71.4	0.23
	[O,C \cdots H+PCM]	19.51	72.0	0.23
	[4.25 Å + PCM]	19.19	70.0	0.22
$\sigma(A)^{[a]}$	[4.25 Å + PCM]	0.18		
Static calcs.	Gas-phase ^[b]	21.5	83.8	
	Gas-phase ^[c]	20.1	82.9	
	Gas-phase ^[d]	18.9		
	BQ \bullet^- + 4H ₂ O ^[c]	21.0	75.4	
	BQ \bullet^- + PCM ^[d]	16.5		
	BQ \bullet^- + 4H ₂ O + PCM ^[b]	20.8	75.1	0.24
	BQ \bullet^- + 5H ₂ O + PCM ^[b]	19.9	71.9	0.23
Experimental		24.4 ^[g]	67 ^[f]	

[a] Standard deviation of the parameter across all equivalent nuclei. See Section 5.5. [b] B3LYP/EPR-II//BLYP/TZVP, own calculations. [c] B3LYP/EPR-II, ref. 131 [d] B3LYP/[631p41]//BPW91/6-31G*, ref. 132 [e] Ref. 105 [f] Frozen isopropanol solution, ref. 123 [g] Ref. 107 [h] Estimated from comparison of frozen ethanol¹⁰⁷ and isopropanol¹³³ solutions.

Table 5.6. HFC and Mulliken spin density (SD) data for benzosemiquinone radical anion (carbon nuclei)

Ring $^{13}\text{C}_{ipso}$		A_{iso}	$A'_{ }$	SD
CPMD	Gas-phase	-8.71	13.0	0.07
	[Lone]	-9.12	12.6	0.06
	[C \cdots H]	-9.73	11.8	0.06
	[O \cdots H]	-1.51	22.3	0.13
	[O,C \cdots H]	-2.13	21.4	0.12
	[Lone+PCM]	-5.54	17.4	0.10
	[O \cdots H+PCM]	0.24	24.6	0.14
	[O,C \cdots H+PCM]	-0.18	24.0	0.14
	[4.25 Å + PCM]	0.91	25.4	0.15
$\sigma(A)^{[a]}$	[4.25 Å + PCM]	0.74		
Static calcs.	Gas-phase ^[b]	-10.2	12.7	
	BQ \bullet^- + 4H ₂ O ^[c]	-4.2	21.1	
	BQ \bullet^- + 4H ₂ O ^[d]	-3.1		
	BQ \bullet^- + PCM ^[e]	0.9		
	BQ \bullet^- + 4H ₂ O + PCM ^[b]	-3.3	22.7	0.13
	BQ \bullet^- + 5H ₂ O + PCM ^[b]	-1.7	24.7	0.14
Experimental		0.7 ^[f]		
Ring $^{13}\text{C}_{ortho}$		A_{iso}	$A'_{ }$	SD x 10 ³
CPMD	Gas-phase	0.67	13.5	85
	[Lone]	0.12	12.7	78
	[C \cdots H]	0.26	12.8	78
	[O \cdots H]	-0.98	12.2	69
	[O,C \cdots H]	-0.83	12.2	70
	[Lone+PCM]	-0.56	12.3	73
	[O \cdots H+PCM]	-1.35	11.9	67
	[O,C \cdots H+PCM]	-1.25	12.0	67
	[4.25 Å + PCM]	-1.38	11.9	66
$\sigma(A)^{[a]}$	[4.25 Å + PCM]	0.50		
Static calcs.	Gas-phase ^[b]	-0.6	13.4	
	Gas-phase ^[c]	-0.3	13.7	
	Gas-phase ^[e]	-0.5		
	BQ \bullet^- + 4H ₂ O ^[c]	-1.1	13.0	
	BQ \bullet^- + 4H ₂ O ^[e]	-1.7		
	BQ \bullet^- + PCM ^[e]	-2.4		
	BQ \bullet^- + 4H ₂ O + PCM ^[b]	-1.9	12.0	71
	BQ \bullet^- + 5H ₂ O + PCM ^[b]	-2.2	11.8	68
Experimental		-2.0 ^[g]		

[a] Standard deviation of the parameter across all equivalent nuclei. See Section 5.5. [b] B3LYP/EPR-II//BLYP/TZVP, own calculations. [c] B3LYP/EPR-II, ref. 131 [d] B3LYP/DP5(d,p), ref. 84 [e] B3LYP/[631p41]//BPW91/6-31G*, ref. 132 [f] Ref. 105 [g] Ref. 107

5.4.1 Solvation effects on HFCs

The effects of solvation on the spin density remarked on earlier in conjunction with the g -tensor can be clearly seen in Tables 5.5 and 5.6. Adding hydrogen bonds to oxygen - going from [lone] to [O...H] - encourages the location of negative charge at oxygen, decreasing the Mulliken spin density there by 0.05; correspondingly, $|A_{iso}|$ drops by 2.6 MHz and $|A'_{||}|$ by 14.7 MHz. The effect of PCM on the naked molecule is similar, but slightly smaller - $|A_{iso}|$ drops by 0.6 MHz and $|A'_{||}|$ by 6.7 MHz; on BQ \bullet^- -H₂O clusters, PCM has a yet smaller effect - 0.44 MHz on $|A_{iso}|$. T-stacked hydrogen bonds, on the other hand, increase the oxygen spin density, and hence HFCs, although the change is very small.

Solvation has the opposite effect on C_{ipso} . Hydrogen bonding pushes spin density off oxygen onto carbon, doubling the spin density at C_{ipso} . A_{iso} , initially very negative due to spin polarisation of the C-O bond, increases drastically as a result. Again, PCM has the same effect, but weaker; T-stacked hydrogen bonding has a very weak effect in the other direction. For the largest calculations, positive spin polarisation is just slightly larger than negative spin polarisation, and the result is a small positive A_{iso} value.

For C_{ortho} , the Mulliken spin density varies little, and the A'_{\perp} values are almost constant. Curiously, it goes *down* with increasing solvation (except for T-stacked hydrogen bonds), which we find surprising - we would expect that the spin density pushed off oxygen by solvation would partly locate itself on C_{ortho} . We assume that the small variations we see arise from trends in spin polarisation of the C_{ipso} - C_{ortho} bonds. This spin polarisation will increase the spin at C_{ipso} and decrease the spin at C_{ortho} , albeit not by very much, and it will only show up in the Mulliken spin density if the shape and overall density of the SOMO at C_{ortho} remains essentially unchanged. The more the unpaired electron (as measurable from the SOMO) is located on C_{ipso} , the stronger the polarisation of the C_{ipso} - C_{ortho} bond and the larger this effect. Additionally, as more of the SOMO becomes located at C_{ipso} , exchange interaction may draw SOMO density from C_{ortho} to C_{ipso} , in addition to polarising the C-C bonds.

This could be clarified by restricted open-shell calculations, in which spin polarisation does not occur. But given the low variability of A'_{\perp} , we assume the variation in A_{iso} probably arises mostly from changes in negative spin polarisation (of the C_{ipso} - C_{ortho} bond). As a result, the trends are opposite those of C_{ipso} - the more solvation, the greater the negative spin density located at C_{ortho} , and the lower its A_{iso} .

The spin density at hydrogen is negative, and arises from polarisation of the C-H bond. As the spin density at C_{ortho} changes little, the parameters of

the ring hydrogens are also nearly unchanging. Hydrogen bonds to oxygen and PCM decrease the spin density at C_{ortho} , and as a result, the spin density and A_{iso} at hydrogen decrease in magnitude (i.e. increase, as they are both negative). The A'_{\perp} value *increases* with solvation, which is curious. We presume that this reflects increased through-space interaction with the spin density around C_{ipso} .

For all nuclei, the most important solvation effects are those of the first solvation sphere. Taking [lone] and [4.25 Å + PCM] as reference (and assuming the latter to be fully converged with respect to size), the [O,C \cdots H] cluster recovers 63 to 77% of the total solvation effects. [O,C \cdots H + PCM] recovers 87-91%. Thus, treating the first solvation sphere explicitly and using PCM to model the effects of further solvation spheres underestimates solvent effects by about 10%. Except for C_{ipso} , this is in each case an error smaller than the difference between [4.25 Å + PCM] and the experimental value.

5.4.2 HFCs and H-bond configurations

Correlation of HFCs (taken from the [4.25 Å + PCM] calculations) with hydrogen bond configurations is shown in Table 5.7. For asymmetric hydrogen bonding situations, we label the side of the molecule with more hydrogen bonds to as (1) (O(1), $C_{ipso}(1)$, $C_{ortho}(1)$) and the other side as (2) (O(2), $C_{ipso}(2)$, $C_{ortho}(2)$).

We can explain the variation of HFCs with H-bond configurations in resonance structure terms (see Figure 4.7 in the previous chapter). H-bonding to an oxygen atom encourages the location of negative charge there, and discourages the location of the unpaired electron there. This displaces spin to the adjacent C_{ipso} , the opposite O and the opposite C_{ortho} centres, and also discourages the location of spin to the nearest C_{ortho} and the opposite C_{ipso} .

This can be clearly seen in Table 5.7. Taking as an example [2,2] and [3,2] - that is, taking a symmetric configuration and adding an extra hydrogen bond to one end - the A_{iso} and A'_{\perp} values go down for the oxygen with the extra hydrogen bond (O(1)), and increase for the other (O(2)), reflecting the shift of spin from one to the other. However, the increase for O(2) is not as large as the decrease for O(1), as some of the spin has shifted to the carbon ring instead of to the other oxygen. As a result, the average A_{iso} over both oxygens goes down on the addition of a hydrogen bond to either one of them. The same is seen across all configurations, with the exception of comparing [2,1] and [3,1] (an anomaly we attribute to statistical noise). The A'_{\parallel} values follow the same trends as A_{iso} . We note that a recent study on H-bonding configurations of ubisemiquinone model complexes found similar results.¹²¹ The asymmetry in the A_{iso} values increases, as we would expect it to, with the

asymmetry of the hydrogen bonding configuration: a 1 H-bond asymmetry ([2,1], [3,2]) gives a 2 MHz difference in A_{iso} ; a 2 H-bond asymmetry ([3,1]), a 3.2 MHz difference; 3 H-bonds ([4,1]), a 4 MHz difference.

For C_{ipso} , the trends are opposite. For the nearest carbon to the extra hydrogen bond ($C_{ipso}(1)$, for [2,2] vs. [3,2]) A_{iso} increases due to increased spin, and for the other ($C_{ipso}(2)$) A_{iso} decreases, but not as much; the average C_{ipso} A_{iso} value increases, as spin shifts overall from the oxygens to the carbons. As a result, the average A_{iso} increases with more hydrogen bonding. For C_{ortho} , however, A_{iso} is seemingly independent of the number of hydrogen bonds, and dependent only on the asymmetry - it varies as $[x,x] > [x+1,x] > [x+2,x]$, with equally asymmetrical configurations having the same values (compare [2,2] and [3,3], [2,1] and [3,2]). To judge by the $A'_{||}$ values, however, there appears to be a slight decrease spin density at C_{ortho} with increasing H-bonding, which fits with our earlier observations on the data in Table 5.6.

In Table 5.8 we correlate HFC data with number of T-stacked hydrogen bonds for [4.25 Å + PCM]. The effects are in line with those noted earlier - T-stacked hydrogen bonding has the opposite effect of H-bonding to carbonyl oxygen, increasing the spin at oxygen and (slightly) at C_{ortho} while decreasing the spin at C_{ipso} .

5.4.3 Structural solvation effects

As with g -tensors, the effects of solvation on the structure of the molecule can have an indirect effect on the HFC data. These can be assessed by comparing the gas-phase and [lone] values of any parameter. As mentioned earlier, solvation lengthens the C-O bond length, favouring resonance structures with spin or negative charge located on oxygen, while shortening the C-C bonds. As a result, the Mulliken spin density for oxygen is higher for [lone] (0.29) than for the gas-phase simulation (0.27), and the A_{iso} and $A'_{||}$ values are also higher. The spin densities for carbons are lower for [lone] than for the gas phase, leading to lower A_{iso} and $A'_{||}$ values for [lone]. Ring hydrogens have higher (less negative) values for A_{iso} , $A'_{||}$ and Mulliken spin density, as less spin on C_{ortho} leads to weaker spin polarisation of the C-H bond.

For oxygen and C_{ipso} , as for the g -tensor, the direct and indirect effects are opposite. For C_{ortho} and ring hydrogens, however, the effects reinforce each other, as both the structural and electronic effects of solvation cause a decrease in the spin density at C_{ortho} (and hence less spin polarisation of the C-H bond).

Table 5.7. Variation of HFCs with O...H configurations. Data taken from [4.25 Å + PCM] calculations.

¹⁷ O						
Configuration	$A'_{ }(1)$	$A'_{ }(2)$	$A_{iso}(1)$	$A_{iso}(2)$	ΔA_{iso}	Avg. A_{iso}
1,1	(75.3)		(20.4)			(20.4)
2,1	68.7	77.0	18.6	20.5	1.9	19.6
2,2	70.8		19.5			19.5
3,1	62.6	77.3	17.7	20.9	3.2	19.7
3,2	64.9	74.2	18.1	20.1	2.0	19.1
3,3	67.6		18.7			18.7
4,1	(58.9)	(81.7)	(16.9)	(20.9)	(4.0)	(18.9)
¹³ C _{ipso}						
Configuration	$A'_{ }(1)$	$A'_{ }(2)$	$A_{iso}(1)$	$A_{iso}(2)$	ΔA_{iso}	Avg. A_{iso}
1,1	(21.28)		(3.04)			(-3.04)
2,1	26.72	19.66	2.86	-5.17	8.0	-1.19
2,2	24.48		-0.13			-0.13
3,1	30.78	17.86	7.90	-6.70	14.6	0.60
3,2	28.89	22.69	4.65	-2.04	6.7	1.31
3,3	27.33		-2.86			2.86
4,1	(33.35)	(17.84)	(8.67)	(-6.76)	(15.4)	(0.95)
¹³ C _{ortho}						
Configuration	$A'_{ }(1)$	$A'_{ }(2)$	$A_{iso}(1)$	$A_{iso}(2)$	ΔA_{iso}	Avg. A_{iso}
1,1	12.40		-0.97			-0.97
2,1	9.28	14.74	-3.87	1.13	5.0	-1.37
2,2	12.03		-1.46			-1.46
3,1	7.07	16.96	-5.55	3.34	8.9	-1.10
3,2	9.23	14.49	-3.74	0.99	4.7	-1.37
3,3	11.71		-1.46			-1.46
4,1	5.76	18.1	-7.09	2.65	9.7	-2.22

[a] Data is bracketed due to infrequency of this H-bonding situation, and hence statistical unreliability.

Table 5.8. Dependence of HFCs on the number of T-stacked hydrogen bonds. Data taken from [4.25 Å + PCM] calculations.

H-bond number	¹⁷ O		¹³ C _{ipso}		¹³ C _{ortho}	
	A_{iso}	$A'_{ }$	A_{iso}	$A'_{ }$	A_{iso}	$A'_{ }$
0	19.0	69.0	16.9	26.3	-1.59	11.9
1	19.1	69.6	1.30	25.7	-1.35	11.9
2	19.4	71.2	-0.37	24.2	-1.35	12.0
3 ^[a]	19.6	(72.2)	(-1.35)	(23.2)	(-1.30)	(12.1)

[a] Data is bracketed due to infrequency of this H-bonding situation, and hence statistical unreliability.

Table 5.9. Principal components and axes of trajectory-averaged dipolar coupling tensors. Data taken from [4.25 Å + PCM] calculations.

Nucleus	A'_{\parallel}		$A'_{\perp}(1)$		$A'_{\perp}(2)$	
^1H	5.7	[H-C]	-2.5	z	-3.3	[a]
$^{17}\text{O}^{[b]}$	67.3	z	-33.3	y	-34.0	x
$^{13}\text{C}_{ipso}$	24.5	z	-10.9	x	-13.6	y
$^{13}\text{C}_{ortho}$	11.2	z	-5.4	[$\text{C}_{ipso}\text{-C}_{ortho}$]	-5.8	[c]

[a] In the plane of the molecule, perpendicular to the C-H bond. [b] The sign for ^{17}O HFC data is reversed here. [c] In the plane of the molecule, perpendicular to the $\text{C}_{ortho}\text{-C}_{ipso}$ bond.

5.4.4 Tensor axes and orientation

Table 5.9 lists and describes the principal components of the trajectory-averaged dipolar coupling tensors. The difference between these and the trajectory-averaged principal components of the dipolar tensors (given in Tables 5.5 and 5.6) is small. The difference, principally caused by vibrational motion, is to reduce A'_{\parallel} by 3-6%, a larger decrease than seen for the g -tensor. We note that for the O and C atoms, the A'_{\parallel} coupling is in the direction of the z axis in each case - that is, the dipolar coupling is dominated by interaction with the p_z lobe of spin density at that nucleus. For ring hydrogens, on the other hand, the A'_{\parallel} coupling is in the direction of the C-H bond - the spin at hydrogen is negligible, so dipolar coupling is dominated by interaction with the spin at the closest atom, C_{ortho} . Of the two perpendicular components, the less negative ($A'_{\perp}(1)$) is along the direction in which more dipolar coupling occurs. For C_{ipso} this points in the direction of oxygen, reflecting dipolar coupling between the C_{ipso} nucleus and the oxygen p_z lobe of the SOMO; similarly, for C_{ortho} it points toward C_{ipso} . Curiously, however, this component is in the y direction for oxygen, which indicates that coupling with the spin-polarisation of the lone-pairs is more important than coupling with the spin density at C_{ipso} . For hydrogen, this component points in the z direction, presumably because coupling with the C_{ortho} p_z spin density has a z component to it.

5.4.5 Comparison with experiment and static calculations

Experimental isotropic values are available for all nuclei. However, to the best of our knowledge, there are no dipolar coupling data available for $\text{BQ}^{\bullet-}$ in aqueous solution. For ring hydrogen we compare with the isopropanol so-

lution value of A'_{\parallel} ;¹²³ for oxygen, we estimate A'_{\parallel} by comparing ethanolic¹⁰⁷ and isopropanolic solution data.¹³³

To assess the effects of dynamics on HFC data, we compare the results of static calculations with the data from our calculations for clusters containing the same interactions. As static calculations typically have 4 water molecules, this means either $[\text{O}\cdots\text{H}]$ or $[\text{O}\cdots\text{H} + \text{PCM}]$. Differences between static and dynamic data will arise due to vibrational motion of the BQ \bullet - molecule and intermolecular motion, including exchange of water molecules between the first and second solvation spheres. We expect vibrational motion to have a greater effect on the gas phase molecule than in aqueous solution, as hydrogen bonding will dampen vibrations involving the carbonyl group.

¹H HFCs

The proton A_{iso} values are slightly overestimated by our methods (see Table 5.5). Our final value is -5.9 MHz, higher than the experimental value of -6.6 MHz. The implication is that the B3LYP/EPR-II methodology underestimates either the polarisability of the C-H bond or the amount of spin on C_{ortho} . We note that we underestimate A'_{\parallel} as well (compared to frozen isopropanol data), which would be expected from locating too little spin on C_{ortho} ; however, we actually overestimate A_{iso} for C_{ortho} . The issue could be resolved if protic solution values for A'_{\parallel} of C_{ortho} were available, but sadly we know of none.

Comparing $[\text{O}\cdots\text{H} + \text{PCM}]$ to static calculations including PCM, we see that inclusion of dynamics decreases the magnitude of A_{iso} - while, however, not affecting the dipolar coupling as significantly. It would seem that vibrational motion of the C-H bond leaves the distance from the spin density around C_{ortho} unchanged, while decreasing the bond polarisability. As neglecting dynamics underestimates A_{iso} , whereas the B3LYP/EPR-II method overestimates it, static calculations benefit from error compensation and are closer to experiment than our dynamics-based method.

The frozen isopropanol dipolar tensor components for ring hydrogen are +2.0 MHz in the z direction and +5.8 and -3.3 MHz in the xy plane;¹²³ our (trajectory-averaged tensor - see Table 5.9) values are -2.5, +5.7 and -3.3 MHz respectively. The difference is small, and within the experimental error of the W-band data (although not of the X-band data, which is similar). We expect the HFC data for ¹H to be very similar in water and in ⁱPrOH on the basis of previous computational studies,⁸⁵ and the similarity of the A_{iso} values (-6.6¹⁰⁵ and -6.7 MHz¹³³ respectively). However, the difference in solvent could conceivably alter the structure and dynamics of the solvation sphere, as isopropanol forms only one hydrogen bond, which is stronger and

shorter than water's, and is sterically far bulkier.

¹⁷O HFCs

Oxygen A_{iso} values (Table 5.5) are consistently underestimated compared to experiment, and the underestimate is worse the larger the solvation sphere. Our best data ([4.25 Å + PCM]) underestimates it by about 20%. This indicates, again, systematic error on behalf of the B3LYP/EPR-II method. For the gas-phase, there is little difference (0.2 MHz) between the static and dynamic calculations. For the solution state, [O \cdots H + PCM] gives a lower value than for both our [BQ \bullet^- + x H₂O + PCM] calculations (by 1.4 MHz for $x = 4$, 0.3 MHz for $x = 5$). This means that static calculations benefit again from error cancellation, albeit only slightly.

The A'_{\parallel} value, in contrast, appears to be slightly overestimated by our methodology (with the caveat that no aqueous data is available, and we estimated the experimental value from comparison of ethanolic¹⁰⁷ and isopropanolic¹³³ data). This is a strong indicator that the amount of spin density around oxygen is estimated reasonably well, and that the underestimate of A_{iso} is due to B3LYP treating spin polarisation of the s -shells of oxygen inaccurately.

¹³C_{ipso} HFCs

The A_{iso} value for C_{ipso} (Table 5.6) is the most sensitive of the HFC parameters discussed in this chapter, and our methodology gives a very accurate estimation of it - our final value is +0.9 MHz, only slightly exceeding the experimental +0.7 MHz. (We note, however, that our C_{ipso} hyperfine data does not appear converged with trajectory length, and our data indicate that a longer trajectory would probably give a slightly higher A_{iso} value - see section 5.5.) Static calculations, on the other hand, universally underestimate A_{iso} . This seems partly due to insufficient treatment of the solvation sphere - static calculations typically include only the first solvation sphere, or in one case a PCM without explicit treatment of solvent molecules.¹³² Our calculations show that including only water molecules H-bonded to carbonyl oxygen, without PCM, underestimates A_{iso} by about 2.4 MHz. If PCM is included, however, the underestimate drops to 0.7 MHz.

Dynamical effects also appear to play a role. For the gas-phase anion, static calculations underestimate A_{iso} by 1.5 MHz, and the difference increases for the solvated system: [O \cdots H + PCM] gives $A_{iso} = +0.24$ MHz, whereas equivalent static calculations (with PCM) give values of -3.3 and -1.7 MHz (with 4 and 5 water molecules respectively).

$^{13}\text{C}_{ortho}$ HFCs

The A_{iso} values for C_{ortho} nuclei are obtained to reasonably good accuracy in the simulations: our best calculations give -1.4 MHz, compared to -2.0 MHz from experiment.¹⁰⁷ The slight overestimate we attribute to DFT errors; although the average C_{ortho} A_{iso} may not be too well converged with respect to trajectory length (see section 5.5). The best static calculations perform better, however, with less than half the deviation from experiment. Unlike other nuclei, for C_{ortho} an insufficient solvation sphere and lack of dynamics give errors in the opposite direction for A_{iso} . Omitting dynamics causes underestimation of A_{iso} : compare the gas-phase values of +0.67 MHz (dynamic) and -0.58 MHz (static) and the solvation state values of -1.35 MHz ($[\text{O}\cdots\text{H} + \text{PCM}]$) and -1.9 and -2.2 MHz (static $[\text{BQ}^{\bullet-} + x\text{H}_2\text{O} + \text{PCM}]$ with $x = 4$ and 5, respectively). Lack of a solvation sphere causes overestimation of A_{iso} : going from [lone] to $[\text{O}\cdots\text{H}]$ to $[\text{O}\cdots\text{H} + \text{PCM}]$ to $[4.25 \text{ \AA} + \text{PCM}]$, A_{iso} consistently decreases.

5.4.6 Solvent proton HFCs

Presenting hyperfine data for solvent nuclei is not straightforward, as the water molecules in solution do not adopt fixed positions and there is, on average, a non-integer number of H-bonded solvent nuclei. Averages over all H-bonded water molecules are dependent on an arbitrary choice of H-bond detection criteria. It is more useful to use graphical methods, such as scatter plots of HFC data against $r[\text{O}\cdots\text{H}]$, or relative frequency plots of A values. However, a numerical average may be obtained by taking the average value a parameter for hydrogen bonds of length c. 1.75 \AA (\pm a small interval). For comparison to experiment, we refer to an ENDOR study performed in frozen solution at 80 K.⁸⁰ The temperature difference between this and the system modelled by our simulation (liquid aqueous solution at 300 K) will need to be borne in mind.

The A_{iso} values ($[4.25 \text{ \AA} + \text{PCM}]$ cluster) of solvent protons H-bonded to carbonyl oxygen are shown, plotted against $r[\text{O}\cdots\text{H}]$, in Figure 5.3; curves are fitted as a function of distance, for all data and for only strongly in-plane or out-of-plane H-bonded protons. Most values are negative, due to spin polarisation of the electron density involved in the hydrogen bond. The shorter the hydrogen bond, the stronger this effect. We see that strongly out of plane solvent protons have more negative A_{iso} values than in plane protons, an effect noted in previous static calculations, which found almost purely dipolar coupling ($A_{iso} = 0 \text{ MHz}$) for in-plane protons. The principal reason for this is that the SOMO has a p_z shape at oxygen, i.e. points out

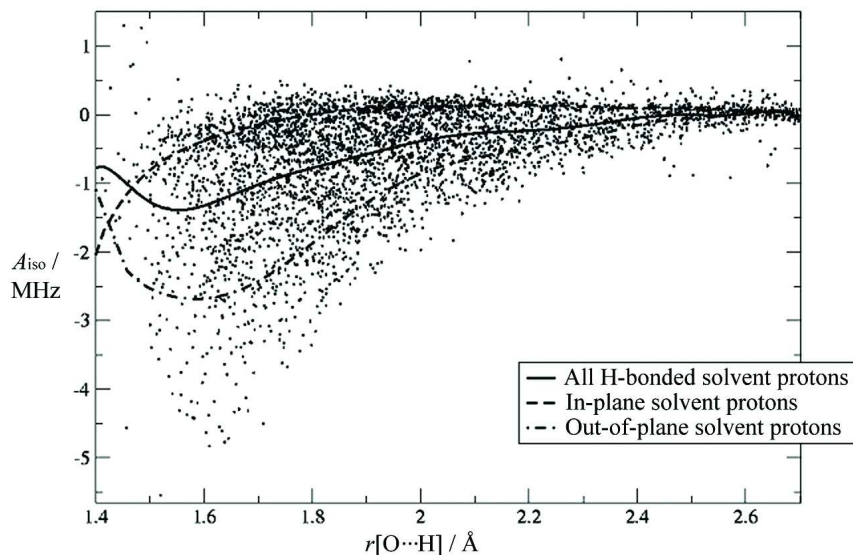


Figure 5.3: H-bonded solvent proton A_{iso} against distance, with curves fitted (10th order regression) for all solvent protons; for all strongly in-plane solvent protons; for all strongly out-of-plane solvent protons. Data taken from [4.25 Å + PCM] calculation.

of plane. Therefore, solvent protons will be closer to the spin density if they approach from out of plane than in plane, and will experience stronger spin polarisation effects.

At very short distances, more positive values start appearing for out-of-plane protons, and the fitted curve in Figure 5.3, although not going over 0 MHz, does rise a little. As this does not happen for in-plane protons, this is probably due to spin delocalisation onto the proton. (Spin delocalisation onto in-plane protons is symmetry-forbidden, as the SOMO has a node in the plane of the molecule.) In-plane protons do have positive values at some distances, however - the fitted curve goes over 0 MHz at about 1.8 Å, indicating that spin polarisation has competing effects, which locate negative spin density on solvent protons at shorter distances and positive spin density at longer distances.

Our results do not match experiment too well. The H-bonded protons have $A_{iso} = +0.3$ in frozen solution, whereas the fitted curve for our in-plane proton data has a negative value at the peak of the radial distribution function, and more out-of-plane protons have even more negative HFCs. This

may be either problem with the balance of spin polarisation effects in the DFT methodology, or due to the fact that our simulated system is a more dynamic system than the experimental frozen solution. In static calculations, the B3LYP/EPR-II methodology gives $A_{iso} = +0.3 (\pm 0.1)$ MHz (from our calculations with PCM and 4 or 5 water molecules and previous studies on $BQ^{\bullet-} + 4H_2O$ clusters^{79,131}) - in very good agreement with experiment. (Evidently, dynamics decreases the HFC coupling, which we would expect - the higher the temperature, the more likely hydrogen bonds are to be out of plane, causing them to have more negative A_{iso} values.) It is possible that static calculations benefit from error calculation, but also that static calculations are simply a better approximation to 90 K frozen solution. The experimental dipolar coupling data (see below) seems consistent with more than 4 hydrogen bonds if we assume a reasonably static arrangement of 4 in-plane and 0 or 1 out-of-plane H-bonds, which argues in favour of the latter. (However, we also note by inspection of our results that neglect of further solvation spheres tends to decrease A_{iso} , which indicates at least some error cancellation in static calculations; although the properties of a previously-simulated $BQ^{\bullet-} + 20H_2O$ cluster⁷⁹ indicated further solvation spheres to have the opposite effect).

The ENDOR study on frozen solution deduced the hydrogen bonds to be very nearly planar, implying only 4 hydrogen bonds to the carbonyl oxygen. That our simulation finds a significant amount of out-of-plane hydrogen bonding is to be expected given the temperature difference; however, we find an average of 4.7 reasonably close ($r[O\cdots H] < 2.25$ Å) hydrogen bonds. That higher temperature should increase the amount of hydrogen bonding seems counterintuitive. We suggest that in frozen solution, there are simply far more in-plane than out-of-plane hydrogen bonds, making the former identifiable in the ENDOR spectrum and the latter not. Let us assume a mix of [2,2] and [3,2] hydrogen bond configurations in frozen solution. At such low temperature, the hydrogen bonds probably lie very close to the energy minimum, so we can deduce by reference to our $[BQ^{\bullet-}(H_2O)_5 + PCM]$ model that at the oxygen with 3 H-bonds, one is strongly out-of-plane and the other two are roughly in-plane (10 and 21°, in the static calculation).^b The two H-bonds to the other oxygen were virtually planar (<5°). For [2,2], all hydrogen bonds are in plane. Thus $BQ^{\bullet-}$ has 4 in-plane hydrogen bonds at all times, and a fractional average number of out-of-plane hydrogen bonds - 0.7, if frozen solution should happen to have the same number of close to-oxygen

^bAdmittedly, one H-bond was constrained to be strongly out-of-plane by the way the static calculation was performed - i.e. the conformation was imposed, rather than found to be so. However, one H-bond perpendicular to the ring and two almost in plane makes sense for a system where H-bonds have an energy minimum in plane.

H-bonds as our 300 K simulation. If that be the case, then in-plane hydrogen bonds outnumber out-of-plane H-bonds by a factor of 6.

The 4 in-plane hydrogen bonds show up in the ENDOR spectra reasonably clearly, with a weak A_{\parallel} component of +6.0 MHz visible in the g_x and g_y signals and a distinct A_{\perp} component of -3.0 MHz in g_x , g_y and g_z . (See Figure 3 of the ENDOR study.⁸⁰) The 0.7 out-of-plane H-bonds should give splitting signals almost 6 times weaker - too weak to observe, given that the A_{\parallel} component for in-plane protons is itself rather weak. The OOP A_{\parallel} signal should be present mostly in the g_z spectrum, and slightly in g_y ; A'_{\parallel} at the RDF maximum is probably about +10 MHz (according to Figure 5.4) and the isotropic coupling around $A_{iso} = -2$ MHz (Figure 5.3), so we estimate $A_{\parallel} = +8$ MHz. (Previous static calculations suggest a similar value.¹³⁴) For the perpendicular component, the dipolar coupling would be around -5 MHz, so this component would show up in the g_x and g_y spectra with a value of around -7 MHz (previous calculations suggest about -7.5 MHz¹³⁴). Therefore, we would expect a splitting in the range of 7-8 MHz in all three components of the ENDOR spectrum, if the signal-to-noise ratio could be significantly improved. A lack of such signals would indicate that frozen solution has no discernable out-of-plane hydrogen bonding, and hence fewer hydrogen bonds than liquid solution.

The largest component of the dipolar coupling is represented graphically in Figures 5.4 (which plots A'_{\parallel} against distance) and 5.5 (which shows the frequency distribution of A'_{\parallel}). The frequency distribution peaks at +6.1 MHz, very close to the experimental value of +6.0 MHz.⁸⁰ However, if we examine Figure 5.4, we see that around the equilibrium distance of 1.75 Å, A'_{\parallel} takes on values of about 8 MHz (6.5 MHz for in-plane solvent protons, 10.5 MHz for out-of-plane solvent protons). At lower temperatures we expect the H-bond lengths to cluster more tightly around the equilibrium value of 1.75 Å and the out-of-plane dihedral angles to get closer to 0°; so our data would suggest a value of $A'_{\parallel} = 6.5$ MHz as a low temperature limit for the in-plane protons.

Dipolar coupling constants have been used¹³³ to obtain bond lengths, or spin density at oxygen, by applying the point-dipole approximation:

$$A'_{\parallel} = \frac{158.4}{r^3} \rho \quad (5.1)$$

where r is the hydrogen bond length and ρ is the oxygen spin density. The assumption is made here that the spin density at oxygen is located at a point, whereas it actually has the shape of a p_z lobe; this is known to be a potential source of error, causing underestimation of the bond length (or, if the bond length is known, overestimation of the spin density). If we take the [4.25 Å +

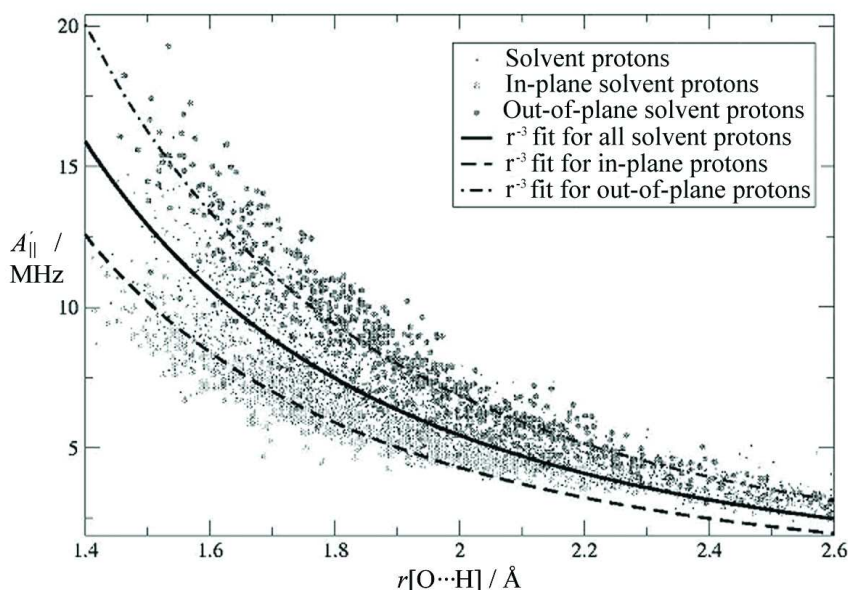


Figure 5.4: H-bonded solvent proton $A'_{||}$ against distance, with curves fitted (r^{-3}) for all solvent protons; for all strongly in-plane solvent protons; for all strongly out-of-plane solvent protons. Data taken from [4.25 Å + PCM] calculations.

PCM] HFC data for all H-bonded solvent protons within 2.7 Å and fit an r^{-3} curve, we obtain a spin density of 0.27, which is too high - the literature value is 0.23,¹³⁵ and our Mulliken spin density is 0.22. If we fit only to in-plane protons, we obtain a more reasonable value of 0.22, although the fit is poor; fitting to out-of-plane protons yields a value of 0.35. (The r^{-3} curves are shown in Figure 5.3.) Out of plane solvent protons give too high a value for the spin density, because (as previously mentioned) they approach from the z direction, and thus are closer to the p_z -shaped spin density lobe on oxygen than protons approaching in-plane. The point-dipole approximation is thus unreliable for out-of-plane solvent protons, but seems to hold well for in-plane protons.

Solvent protons involved in T-stacking interactions number approximately one per snapshot; averaging their HFC data gives $A_{iso} = -0.2$ MHz and $A'_{||} = +3.0$ MHz. No matching hyperfine signals have been observed in experiment, but they would be unidentifiable from the aqueous frozen solution spectra even if present. The $A_{||}$ signal would have a value of +2.8 MHz and be in the direction of the T-stacked H-bond, more or less in the z direction; this would be hard to distinguish from the +3.0 MHz signal of the solvent protons H-bonded to carbonyl oxygen, which are more numerous. In the x and y di-

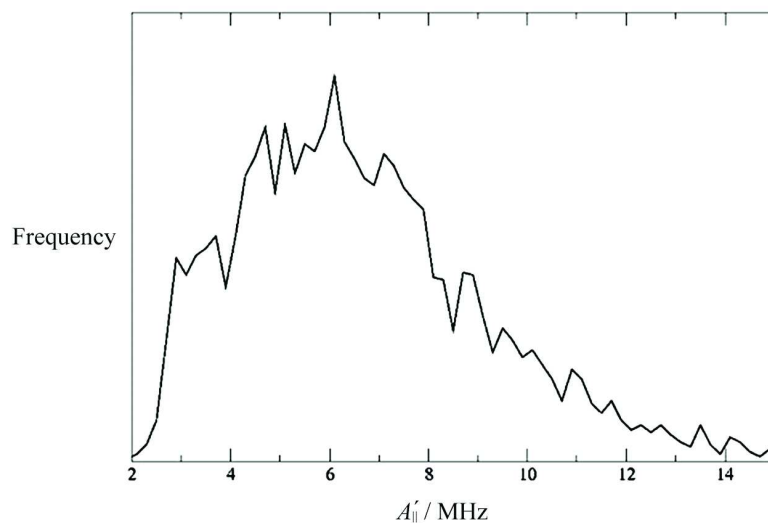


Figure 5.5: Frequency distribution of H-bonded solvent proton $A'_{||}$ against distance. Data taken from [4.25 Å + PCM] calculations.

rections, we calculate the A_{\perp} components as -1.0 and -2.3 MHz respectively ($A'_{\perp} = -0.8$ and -2.1 MHz); these would be lost in the massive peaks arising from general matrix protons.

5.5 Further work

The most important question regarding the accuracy of our EPR data is whether the simulation of aqueous BQ \bullet^{-} is sufficiently long, as all other errors are in principle systematic. For the hyperfine data, one useful measure is to take the standard deviation of a parameter across all formally equivalent nuclei (which, for ^{17}O and C_{ipso} , is equal to the difference between the individual nuclei and the average over both nuclei). Over a long enough trajectory, the difference between the properties of formally equivalent nuclei should become negligible; a standard deviation significantly above zero indicates that the trajectory has not sampled the full phase space of the system, or at least not done so sufficiently rigorously. For the isotropic HFCs, the standard deviation is very small for ^{17}O and ring ^1H (0.2 MHz). For the carbon nuclei, however, $\sigma_{A_{iso}} = 0.5$ and 0.7 MHz for C_{ortho} and C_{ipso} respectively. This is a larger error than we would like, especially for C_{ortho} , whose HFCs are not very sensitive to environmental effects. For C_{ipso} , whose isotropic HFC varies

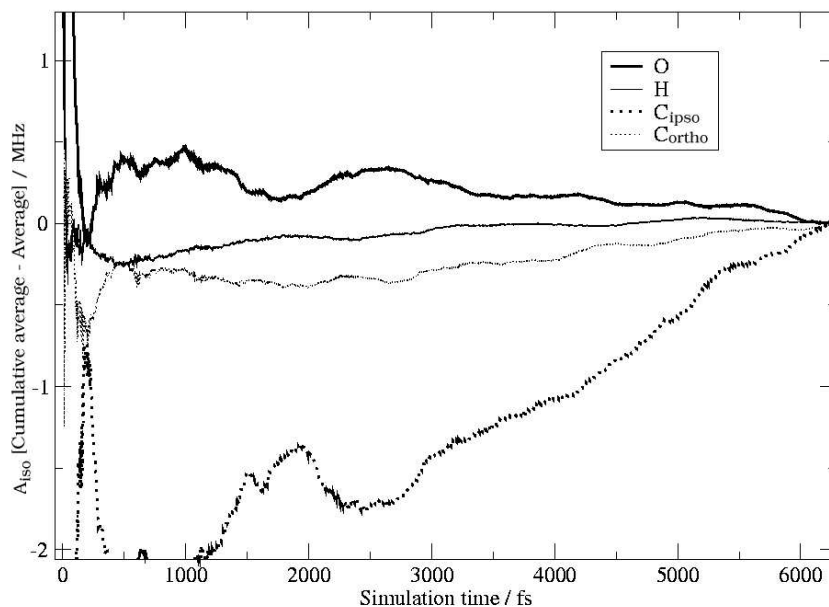


Figure 5.6: Plot against time of cumulative averages of isotropic hyperfine coupling constants ([4.25 Å + PCM] cluster), as deviations from average value.

by 10 MHz between the gas phase and the solution state, this is a less severe error.

Another measure of whether the simulation time is adequate is the cumulative average of various properties. Given a sufficient trajectory length, the cumulative average plotted against time (the average of the property from the beginning of the trajectory up to that point) should converge to more-or-less a straight line, indicating that increasing the trajectory length causes no change in the average value of that property. Small fluctuations are tolerable (an infinite trajectory length would be necessary for the property to be completely unchanged if more snapshots are added), but large fluctuations or significant drifts indicate that a longer simulation would be desirable.

We plot the cumulative averages of the isotropic HFCs in Figure 5.6, as deviations from the average value. It can be seen that there is a slight downward trend in the oxygen A_{iso} ; the C_{ortho} and ring H isotropic HFCs are reasonably constant; but the C_{ipso} isotropic HFC is still on a distinct upward trend. This indicates that our dynamic value of A_{iso} for $^{13}\text{C}_{ipso}$ is probably too small, and a longer trajectory would yield a larger value.

In Figure 5.7 we plot the cumulative average of the Δg_x component. It seems to be levelling off from a slight downward trend at the end of the

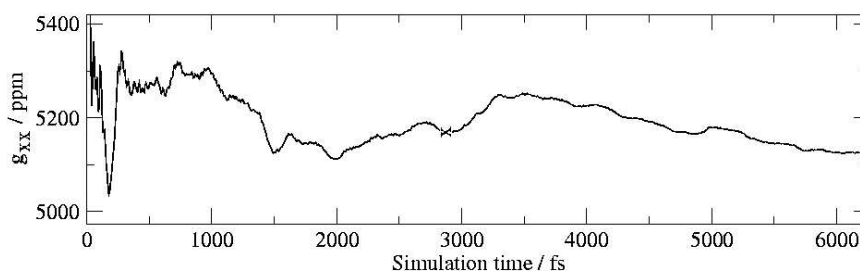


Figure 5.7: Plot of cumulative average of g_{xx} ([4.0 Å + PCM] cluster) against time.

trajectory (which would be expected from the downward trend in the oxygen isotropic HFC, as both depend on the spin density at oxygen).

Further work on aqueous $BQ^{\bullet-}$ could include the lengthening of the MD trajectory, and a low-temperature simulation. A longer trajectory would more exhaustively sample of the phase space of the system and obtain better HFC parameters therefrom; although we expect the improvement to be still only a fraction of a MHz in the case of C_{ipso} . It would be useful to perform lower temperature simulations of aqueous $BQ^{\bullet-}$ to determine how the EPR parameters, HFCs in particular, differ in the frozen compared to the liquid state. A low temperature simulation would enable more informed comparison between calculated and experimental frozen-solution data, which is often acquired at temperatures closer to the absolute zero of a static calculation than the 300 K of our MD simulation.

Chapter 6

Ubisemiquinone Molecular Dynamics

6.1 On Ubisemiquinone

Ubiquinone (UQ) and its reduced form ubisemiquinone (UQ^{•-}) are present in all living things, playing roles as both 1- and 2-electron transfer agents in processes such as respiration and photosynthesis.⁷⁰ Analysis and computational modelling of UQ and UQ^{•-} is a far more complex issue than for the more simple benzo(semi)quinone. The side-groups of UQ^{•-} introduce additional complications not present in BQ^{•-}: lower symmetry, conformational effects, steric hindrance to hydrogen-bonding solvent molecules, and a new type of hydrogen bond (to methoxy oxygen, in addition to hydrogen bonds to carbonyl oxygen and the C_π ring). These all need to be taken into account in discussing magnetic resonance parameters and other properties of UQ^{•-}. The conformation of the methoxy side-chains is a particular challenge, as they need to be considered as a pair - both interact strongly with each other. A set of static calculations can give an idea of the energy difference between the methoxy conformations (a few kJ/mol^{121,136,137}), but this cannot include the effects of vibrational motion - i.e. of temperature - and of the shifting solvation sphere.

These complex dynamics, and the importance of the molecule, make it a prime candidate for MD treatment. This has already been done using hybrid QM/MM methodology for the solvated neutral system,¹³⁸ using classical molecular dynamics for the aqueous neutral and anionic systems⁸¹ and for simulating interactions with protein environments,¹³⁹ and using CP-MD for the gas-phase anion.⁸¹ However, no CP-MD or QM/MM studies have yet been performed on the solvated anion. Therefore, we decided to include the

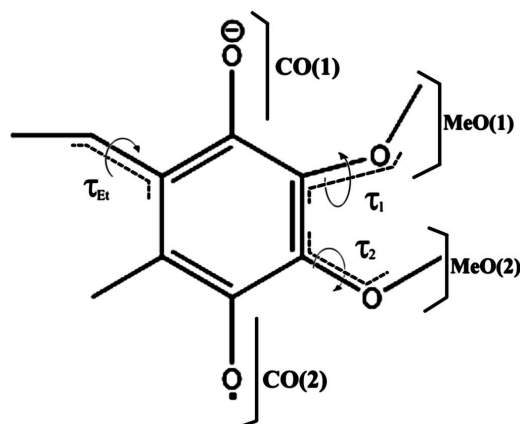


Figure 6.1: The ubisemiquinone simulated (with isoprenoid chain replaced by ethyl) and definitions pertaining thereto.

aqueous $\text{UQ}^{\bullet-}$ in our studies, simulating it at the CP-MD level and employing the methodology developed in the previous two chapters.

6.2 Computational details

The CP-MD run was performed in a similar fashion to the $\text{BQ}^{\bullet-}$ simulation (with the BLYP density functional^{17,18} and a planewave basis with 70 Ry cut-off), using a slightly-trimmed version of ubisemiquinone with the isoprenoid tail replaced by an ethyl group. (The full molecule would be too large to treat in solution at the CP-MD level.) The CPMD code 3.5.2⁷³ was used. A larger box was used (14 x 13 x 16.5 Å), containing the ubisemiquinone molecule and 92 water molecules. The timestep was set to 7 atomic units (0.17 fs), although a short period of the preproduction trajectory was run with 5 a.u. timestep to examine the effect on energy conservation. Trouiller-Martins norm-conserving pseudopotentials⁷⁴ were used. The simulation was run for 7.99 ps in total, of which an initial 5.38 ps were discarded as an equilibration period and the latter 2.61 ps taken as production run.

As this is a somewhat shorter production run than that simulated for $\text{BQ}^{\bullet-}$, we note that the data obtained from our simulation will not be as statistically reliable as for the other semiquinone. We would ideally like a significantly longer simulation for $\text{UQ}^{\bullet-}$, because of the lower symmetry and the need to fully sample the different conformations available. We present these results as preliminary, and hope to be able to perform a longer simulation in the future.

The notation we use in this section for the atoms and groups of UQ^{•-} is as follows: the methoxy group opposite the isoprenoid (or ethyl, in this case) side-chain we term MeO(1), and that opposite the methyl group is MeO(2). The carbonyl groups are labelled similarly, and oxygen atoms are distinguished by superscripts (e.g. O_{CO}(1), O_{MeO}(1)). The torsional angles of the side-chains can be defined either as $D(X_\beta-X_\alpha-C_{ortho}-C_{ipso})$ or $D(X_\beta-X_\alpha-C_{ortho}-C_{ortho})$. We take the latter option, and label them as τ_1 , τ_2 and τ_{Et} for the two methoxy and the ethyl groups respectively. This is illustrated in Figure 6.1 above.

Hydrogen bonding to oxygen and to the carbon ring was analysed using similar criteria to BQ^{•-}. For carbonyl oxygen, the requirements are $r[\text{H}\cdots\text{O}] < 2.25 \text{ \AA}$ and $\angle(\text{O}-\text{H}\cdots\text{O}) < 90^\circ$. For methoxy oxygen, the "loose" criteria are the same as for carbonyl oxygen, and used for analysis of the solvation sphere (e.g. for the graphs shown in Figures 6.3 and 6.4). The "strict" criteria include the requirement that the water molecule involved not already be H-bonded to carbonyl oxygen; this is used for determining the number of hydrogen bonds present, either on average or instantaneously. Similarly for the C _{π} ring, the "loose" criteria are as for benzosemiquinone. The "strict" criteria include the requirement that the water molecule not already be hydrogen-bonded to methoxy or carbonyl oxygen.

6.3 Hydrogen bonding

The frequency (in %) of particular numbers of the different H-bond types, together with the simulation average, is shown in Table 6.1 (strict criteria).

6.3.1 H-bonds to oxygen

Ubisemiquinone can accept hydrogen bonds not only to its carbonyl oxygens, but also (unlike benzosemiquinone) to methoxy oxygens. Unsurprisingly, hydrogen bonding to carbonyl oxygen is the strongest, with an average of 4.6 hydrogen bonds per snapshot. (The instantaneous number of hydrogen bonds to carbonyls varies from 2 to 7, and as with BQ^{•-}, the most common number is 5, followed by 4. The configurational breakdown is also similar, with 3/2 being most common (37%), followed by 2/2 and 3/3 (14%) and 2/1 (13%).) Hydrogen bonds to methoxy oxygens, on the other hand, number a mere 0.9, varying from 0 to 3. (This brings the total number of to-oxygen hydrogen bonds to 5.6.) This is to be expected both on steric and mesomeric grounds: carbonyl oxygens are chemically bonded only in one direction, while methoxy oxygens are bonded in two, which drastically reduces the angles of

Table 6.1: H-bond numbers to UQ^{•-}

H-bond to:	O _{CO}	O _{OMe}	C ₆
Number of H-bonds:	Frequency (%)		
0	-	31	64
1	-	47	25
2	4	20	10
3	14	3	1
4	25	-	-
5	38	-	-
6	15	-	-
7	5	-	-
Simulation average:	4.6	0.9	0.7

approach available to potential hydrogen bond donors. Additionally, O_{CO} are far more negatively charged - if the resonance structures of UQ^{•-} are examined (see Figure 6.2), methoxy oxygens cannot accept negative charge, but can donate it, becoming positively charged (while making the rest of the π -system more negatively charged).

We might expect steric obstruction (from the methoxy, methyl and ethyl groups) to have a slight effect on hydrogen bonding to the carbonyl oxygens as well, and this would be expected to decrease the number of hydrogen bonds compared to BQ^{•-}. However, the difference is very small (4.6 vs. 4.7 hydrogen bonds), and not statistically meaningful. Steric effects do appear to show themselves, though, in the radial distribution function (RDF) of carbonyl oxygens, shown in Figure 6.3. The RDF peak is broader than for BQ^{•-}, and its maximum value at a larger distance - in fact, apart from the magnitude of $g(r)$, it looks more like the RDF for neutral benzoquinone than for the anion. This could be interpreted as indicating weaker hydrogen bonding in ubisemiquinone than benzosemiquinone, but the similar numbers of hydrogen bonds, and the orientation of nearby solvent molecules (see Figure 6.4 and discussion later in this chapter) argue against this. Presumably steric effects, by narrowing the angles of approach to the carbonyl oxygen, force the H-bonded solvent molecules slightly closer together. The steric crowding lengthens the hydrogen bonds and broadens the RDF peak. (The peak RDF value is about 1.95 Å. Fitting a gaussian function to the 1.65-2.05 Å region returned a peak RDF value of 5.4 at 1.89 Å. A longer trajectory is needed to plot a better graph.)

This estimate is larger than those generally provided by other theoretical studies. A previous MM-MD simulation of UQ-Et^{•-} found an RDF peak at 1.77 Å.⁸¹ However, given that they estimated the size of the first solvation

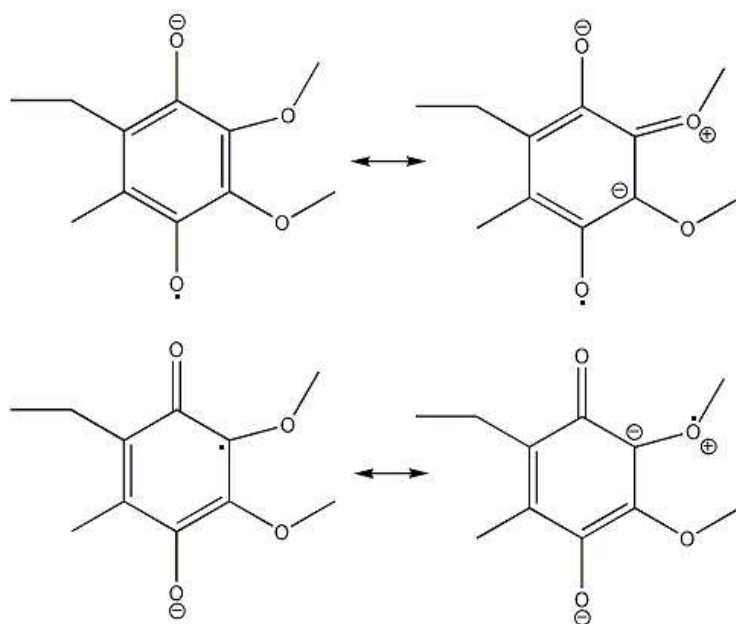


Figure 6.2: Resonance structures of $\text{UQ}^{\bullet-}$: interaction of methoxy groups with the π -system.

sphere at 2.4 water molecules (an unrealistically low value), this is unsurprising: steric crowding will hardly be a factor when only 1.2 water molecules are bound to each oxygen, and H-bond lengths also tend to be smaller the fewer water molecules are bound even in the absence of steric factors.⁷⁹ O'Malley's B3LYP/EPR-II calculations on $\text{UQ}^{\bullet-} \cdot 4\text{CH}_3\text{OH}$ give a hydrogen bond length of 1.79 Å.¹⁴⁰ Kaupp *et al.* found a range of bond lengths from 1.78 to 1.89 Å.⁸⁵ However, calculations on the binding site of quinol oxidase found H-bond lengths (involving water) of 1.76 to 2.12 Å¹²¹ and our own static calculations on $\text{UQ}^{\bullet-} + 5\text{H}_2\text{O}$ (BLYP/6-31G*) return a range of bond lengths from 1.85-2.00 Å. Experimental data for water is unavailable, unfortunately. The value for frozen isopropanol solution is 1.89 Å to $\text{O}_{\text{CO}(1)}$ and 1.94 Å to $\text{O}_{\text{CO}(2)}$,¹³³ in line with our estimate. (The frozen ⁱPrOH solution ENDOR data suggests 1.78 Å hydrogen-bonds to $\text{BQ}^{\bullet-}$, which is not far from the experimental aqueous value of 1.76 ± 0.03 Å⁸⁰ or our simulated aqueous value of 1.75 Å.)

Additionally, the steric differences between the two ends of the molecule should show themselves eventually, over a long enough timescale, as the ethyl group should have a greater steric effect on hydrogen bonding than the methyl group. However, the trajectory length of 2.6 ps is not sufficient to consider the difference we see as significant: the CO(2) group has 0.1 more hydrogen bonds per snapshot than CO(1) - an even smaller difference than for $\text{BQ}^{\bullet-}$,

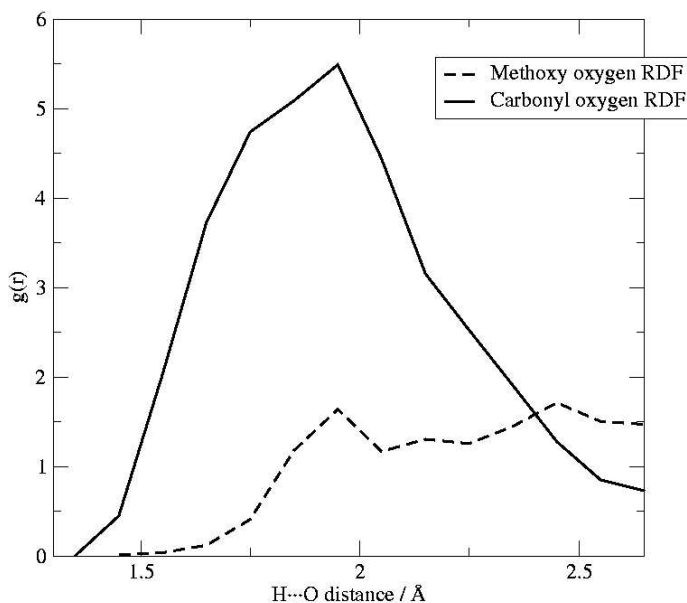


Figure 6.3: Radial distribution functions of nearest solvent hydrogens around $\text{UQ}^{\bullet-}$ oxygens.

which despite being symmetrical and having a longer trajectory displayed a 0.2 H-bonds per snapshot difference between the two carbonyl oxygens.

Solvent hydrogens can potentially fulfil the criteria for hydrogen bonding to both carbonyl and methoxy oxygens, locating them less than 2.25 Å from each. In our BLYP/TZVP static calculation on $\text{UQ}^{\bullet-}+4\text{H}_2\text{O}$, one solvent proton was found hydrogen-bonded to both carbonyl and methoxy oxygens - the H-bond lengths being 2.10 Å to O_{CO} 2.24 Å to O_{MeO} , and the (O-H...O) angles being 142 and 135 ° respectively. We counted such hydrogen bonds as being to carbonyl, and not to methoxy (hence the strict criteria designated in section 6.2), as the H-bonding interaction with carbonyl oxygen is stronger. (Also, as we shall see in the next chapter, the effects of nearby solvent protons in stabilising negative charge at carbonyl oxygen (the principal effect of $\text{H}\cdots\text{O}_{\text{CO}}$ interactions) are significant beyond 2.25 Å distance - such that when considering the g-tensor, most water molecules H-bonded to O_{MeO} (even under "strict" criteria) act as if weakly H-bonded to O_{CO} instead.) As mentioned, the average number of to-methoxy H-bonds is 0.9 under these criteria, with the instantaneous number varying from 0 to 3 in total, and from 0 to 2 per methoxy group; 1 such hydrogen bond overall is the most common situation, however, followed by none. (See Table 6.1.)

For some purposes, it is useful to use the loose criteria of counting H-

bonds to methoxy oxygens without excluding to-carbonyl H-bonds, as they form a major part of the methoxy oxygens' solvation sphere. The O_{MeO} RDF in Figure 6.3 was plotted under the loose criteria. In it, we see the effects of the nearby carbonyl oxygen attracting solvent protons to itself: after a small peak around 1.9-1.95 Å, the RDF drops slightly then climbs again, forming a large, broad peak around 2.5 Å. This latter peak represents the hydrogen bonds clustered around carbonyl oxygen. Under loose criteria, we find a total of 1.1 hydrogen bonds to methoxy oxygens, and the longest-lasting hydrogen bond endures for 335 fs.

A curious feature of our ubisemiquinone simulation is the correlation between the number of hydrogen bonds to carbonyl and the number to methoxy oxygens. The correlation would be expected to be negative, with hydrogen bonds to carbonyl decreasing the capacity of methoxy oxygens to hydrogen-bond - as happened with T-stacked hydrogen bonds in the BQ[•]-simulation, which were discouraged by to-oxygen H-bonding (the T-stacked H-bonds should show the same correlation in this simulation, too). However, the correlation is in fact positive, with carbonyl hydrogen bonding encouraging methoxy hydrogen bonding, and the correlation with T-stacked H-bonds is ambiguous:

Table 6.2: Correlation of numbers of T-stacked and to-methoxy H-bonds with number of to-carbonyl H-bonds (strict criteria)

$n(H\cdots O_{OC})$	$n(H\cdots O_{MeO(1)})$	$n(H\cdots O_{MeO(2)})$	$n(H\cdots C_{\pi})$
2	(0.0) ^[a]	(0.4)	(0.4)
3	0.3	0.4	0.4
4	0.5	0.5	0.5
5	0.5	0.5	0.6
6	0.6	0.6	0.3
7	(0.2)	(0.0)	(0.0)

[a] Brackets indicate statistical unreliability due to the low frequency of the H-bonding situation.

6.3.2 H-bonds to carbon

T-stacking hydrogen bonds are found in our simulation of ubisemiquinone, although there are fewer than in the case of benzosemiquinone. The number of such hydrogen bonds found depends on the criteria: under the loose criteria, 0.7 T-stacking hydrogen bonds are found. Under the strict criteria, excluding solvent molecules H-bonded to methoxy oxygens, 0.5 T-stacking

hydrogen bonds are found. The low number compared to benzoemiquinone can be attributed to the steric obstruction of the side-chains, as well as competition from the methoxy groups, and does not reflect on the strength of the interaction - T-stacking hydrogen bonds appear to be distinctly *stronger* to ubisemiquinone than to benzoemiquinone, as seen in the next subsection.

6.3.3 H-bond directionality

The strength of a particular type of hydrogen bonding can be judged from its directionality - the number of hydrogen bonds found with angular criteria applied, as a fraction of the number of water molecules within range. In Chapter 4 we plotted this property against distance for T-stacked hydrogen bonding, and we consider it a useful measure of determining the strength of different types of hydrogen bonds. In Figure 6.4 we plot, for all types of hydrogen bonds (loose criteria), the directionality against the angular criterion involved, which is essentially a cumulative frequency graph of angular distribution.^a We also consider the "median" angle, which is the O-H-X angular criterion that returns half of all nearby water molecules as hydrogen bonding. (The hydrogen bond numbers used are without proximity checks, in case of to-methoxy H-bonds, and with proximity checks only to carbonyl oxygens, in case of T-stacking H-bonds.)

The more directional a particular type of hydrogen bond is, the greater the angle at which the curve begins to drop off. The strongest interaction is hydrogen bonding to carbonyl oxygen of BQ^{•-} and UQ^{•-} - essentially all nearby water molecules count as H-bonded for angular criteria up to 120°, and the median angle in both cases is about 160° (an almost linear hydrogen bond). Hydrogen bonds to carbonyl oxygen of neutral BQ are slightly less directional, with a median angle of 157°, as less negative charge is located on the carbonyl oxygens. The methoxy oxygens of UQ^{•-} are even less directional (147°) than hydrogen bonds to the neutral system, which fits with the mesomeric location of positive charge on these oxygens shown in Figure 6.2.

Comparing benzoemiquinone and ubisemiquinone, we would expect the latter to display stronger hydrogen bonding to the carbonyl oxygens and the C₆ ring, due to the donation of negative charge by the methoxy groups. In fact, only T-stacking hydrogen bonding appears notably more directional,

^aNormally, cumulative frequency counts all data points *up to* a particular value, rising from 0 to 1 (or 0% to 100%). However, we are displaying the proportion of nearby water molecules for whose closest hydrogen, the O-H-X angle is *more than* a particular value, so we get an inverted cumulative frequency graph running from 1 - the angular criterion being so low that no water molecules can fail to meet it - to 0 - the angular criterion being so high that no water molecules do meet it.

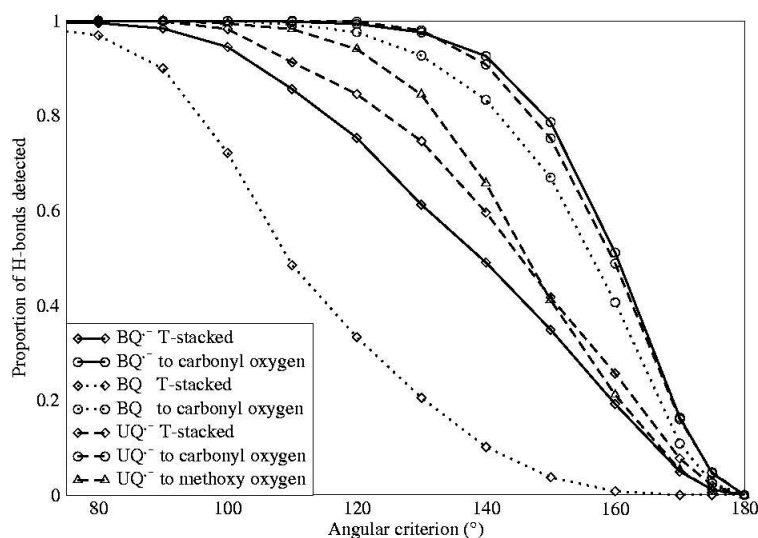


Figure 6.4: Directionality graph. Labels refer to system ($\text{UQ}^{\bullet-}$, $\text{BQ}^{\bullet-}$, BQ) and type of hydrogen bond. See subsection 6.3.3 for details.

with a 7° greater median angle (146° vs. 139°); the curve for hydrogen bonding to carbonyl oxygen is almost identical for both semiquinones. Evidently, the negative charge loaned by the methoxy groups primarily locates itself on the carbon ring.

T-stacking hydrogen bonds are far less directional than hydrogen bonds to carbonyl oxygens, as expected. (The case of T-stacking interactions with neutral benzoquinone is included only for completeness; we concluded in Chapter 4 that this interaction was too weak to merit calling a hydrogen bond, and the data shown in Figure 6.4 confirms this.) However, in the case of $\text{UQ}^{\bullet-}$, hydrogen bonds to methoxy groups and to the carbon ring are of similar directionality and almost the same median angle (147° vs. 146°), but the curves are of slightly different shapes. If the curve is differentiated to show relative frequency of different angles (data not shown) it seems that T-stacking hydrogen bonds are more likely to be very highly directional (160 - 180°), less likely to be moderately directional (125 - 160°) and more likely to be not all that directional at all (90 - 125°). We suppose that to-methoxy hydrogen bonding is a slightly stronger interaction, and that it displays fewer near-linear hydrogen bonds because of the close proximity of the highly-negative carbonyl oxygens, which pull the protons towards them.

6.4 Geometry

6.4.1 Conformation

The orientation of the ethyl group is reasonably constant - it stays perpendicular to the plane of the ring the whole way through the trajectory. The dihedral angle τ_{Et} has an average of 92° , with a standard deviation of $\pm 21^\circ$. (If we define the dihedral angle as $D(C_\alpha-C_\beta-C_{ortho}-C_{ipso})$ instead, we find an average value of $272 \pm 21^\circ$.) This is consistent with the findings of previous works on the subject.⁸⁵

The methoxy group orientations are a more complex matter. The dihedral angles τ_1 and τ_2 are defined, as mentioned, as $D(C_{Me}-O-C_{ortho}-C_{ortho})$. For clarity we omit the sign and merely specify the magnitude and whether the methoxy group is pointing "up" or "down" in the z direction. "Up" is the direction in which the MeO(2) group points (as it remains pointing in the same direction for the whole of the trajectory); the ethyl side-chain happens to point "down", as does MeO(1) for most of the trajectory. The methoxy groups can tilt "inward" ($\tau < 90^\circ$), i.e. towards each other, or "outward" ($\tau > 90^\circ$), away from each other.

Previous computational studies tended to find the methoxy groups both pointing "outwards", typically with torsional angle around 120° . Nonella found a 0.87 kJ/mol difference between conformers with both MeO groups "up" and with one "up" and one "down" (albeit in a model with both methyl and isoprenyl replaced by hydrogen); while a conformer with one group "inwards" and one "outwards" was calculated to be 10 kJ mol⁻¹ higher than either.¹³⁷ One combined experimental/theoretical study suggested a dihedral angle of about 135° by using semiempirical modelling to interpret EPR data. In contrast, a UBP86 study of Kaupp *et al.* found large "outward" orientation in the gas-phase, but a conformation with both groups slightly "inward" when solvent molecules were attached.⁸⁵ Frozen ENDOR data in isopropanol finds the same signal for protons of both methoxy groups, which indicates that rotation of methyl around the O-Me bond is fast, and suggests that the conformation of the methoxy groups is either symmetrical, or asymmetrical and rapidly interconverting (even at low temperature).¹³³

Our simulation finds the methoxy conformation to be generally asymmetrical. For an initial period lasting a little over a picosecond, the methoxy group opposite the ethyl side-chain has a dihedral angle of about 110° - almost perpendicular to the ring. The other methoxy group (opposite the methyl side-group) lies roughly in plane, and points "inwards", towards the first methoxy group - its dihedral angle varies between 0 and 60° in each direction, but it generally swings "down". Then the conformation briefly

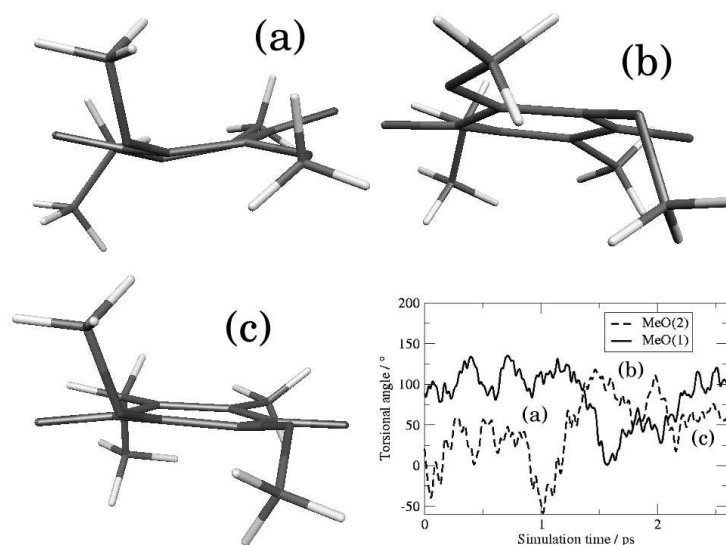


Figure 6.5: Methoxy conformations observed. (a) MeO(1) sticking up above the plane of the ring, MeO(2) roughly in-plane, oscillating above and below. (b) MeO(2) has swung down and outwards, MeO(1) has swung inwards. MeO(2) now more out-of-plane. (c) Similar to (a), but with MeO(2) somewhat more out-of-plane. Inset graph shows time-variation of dihedral angles: in case of MeO(2)) "negative" τ_2 indicates MeO(2) swung upwards above the plane of the ring.

reverses itself, with the first methoxy group tilting "inwards" and the second swinging "outwards". The trajectory then concludes with a reversion to the initial conformation, except for the second methoxy no longer being particularly in-plane, with a dihedral angle of circa 60° . These conformations are depicted in Figure 6.5. In general, the methoxy group opposite ethyl has larger dihedral angles (by 40°) than that of the methoxy group opposite methyl. If the frequency of certain dihedral angles being found is plotted, it is seen that the methoxy group opposite methyl has a preference for dihedral angles of 90° or above (tilted "outwards"), while the other prefers dihedral angles around 50° (tilted "inwards").

It is possible that the differences between the two methoxy groups would disappear on a longer trajectory, and we hope to find out. However, at no point do we see both methoxy groups with a dihedral angle of 120° , let alone 135° . Only for a few femtoseconds do we see both dihedral angles more than 90° , and that only during the change of conformation - where the second methoxy group is swinging out of plane, and the first is beginning to move more in-plane, apparently in response. We cannot say, based on our trajectory, that a conformation with both dihedrals approximately equal

to 120° (or more) is impossible or even uncommon, but only that such a conformation would only be one among several that exist in the aqueous phase.

There seems to be a correlation between the conformation and the number of hydrogen bonds to the methoxy groups. The correlation shows up most clearly if we look at the difference between the two groups for each value. For the 25% of the trajectory where $\tau_2 > \tau_1$, OMe(2) has on average 0.3 hydrogen bonds *less* to it than to OMe(1). For the other 75% where τ_1 is greater, OMe(2) has 0.2 hydrogen bonds more to it than to OMe(1). This could be expected on simple steric grounds: if, say, OMe(2) points "inward" and OMe(1) points "outward" (as in conformation (a) of Figure 6.5), the lone-pairs of OMe(2) will be most accessible, pointing "outward"; while the lone-pairs of OMe(1) will be less accessible - both by virtue of pointing more "inward", and by direct steric obstruction from the methyl of OMe(2). This may be part of the reason for some static calculations showing both methoxy groups to have large τ values - if hydrogen bonding to methoxy is not explicitly considered, the error involved would tend to lead to methoxy groups pointing more "outward". However, the work of Kaupp *et al.*⁸⁵ indicates that such hydrogen bondings tend to *increase* the dihedral angles.^b We do not have a good explanation for this. We also note that, though we do not see any clear signs of this if we plot H-bond numbers against $\tau(2)$, this interrelation between hydrogen bonding and methoxy orientation could conceivably reverse at very low dihedral angles - if the methoxy group is in plane, the conformation is right for the oxygen to become part of the π -system, donating negative charge and becoming less susceptible to hydrogen bonding.

Another thing noted in previous calculations⁸⁵ is that the addition of hydrogen bonding to carbonyl oxygens decreases the dihedral angle τ_1 , pushing both MeO groups "inwards". We find something similar in our simulations - that increased to-carbonyl H-bonding causes the MeO(1) group, the most out-of-plane, to swing "inwards". (The ethyl side-chain shows a similar effect, although not so clearly.) At the same time, τ_2 increases, i.e. the MeO(2) group swings "outwards", possibly as a knock-on effect of steric repulsion from MeO(1). The data are shown in Table 6.3 below.

We might be tempted to ascribe this to steric effects: H-bonding to CO(1) will sterically push MeO(1) "inwards", and MeO(2) will be pushed out and down as a knock-on effect. However, if we look at the correlation with hydrogen bonds to the *individual* CO groups (Table 6.4), we find this is not the case: H-bonding to CO(1) has no clear correlation with either torsional an-

^bIn ref.⁸⁵ the dihedral angles are given as decreasing, but this is due to different definitions.

Table 6.3: Correlation of dihedral angles with number of $\text{H}\cdots\text{O}_{OC}$ hydrogen bonds

$n(\text{H}\cdots\text{O}_{OC})$	τ_1	τ_2	τ_{Et}
2	122	37	98
3	101	25	98
4	82	32	100
5	82	56	92
6	81	64	79
7	79	45	73

Table 6.4: Correlation of dihedral angles with number of hydrogen bonds to individual CO groups:

$n(\text{H}\cdots\text{O}_{OC})$	τ_1	τ_2
<i>To O_{OC}(1):</i>		
1	82	42
2	89	42
3	82	57
4	80	46
<i>To O_{OC}(2):</i>		
0	117	49
1	102	19
2	91	42
3	78	55
4	92	52

gle. On the other hand, H-bonding to CO(2) correlates in the same manner as the total number of $\text{H}\cdots\text{O}_{OC}$ hydrogen bonds with both torsional angles.

It is possible that statistical noise is masking a correlation regarding hydrogen bonds to CO(1), or that the correlation is mere coincidence - that the transition from conformation (a) to conformations (b) and (c) just happen to coincide with that portion of the trajectory where hydrogen bonding to CO(2) is highest. Or it is possible that some unexplained electronic effect is being seen (in which case it is still probable that a similar correlation regarding H-bonds to CO(1) is being masked by noise). In order to explain this, further analysis and a much longer trajectory will be required.

6.4.2 Bond lengths and angles

The important carbonyl C-O bondlength in $\text{UQ}^{\bullet-}$ is 1.30 Å (for both carbonyl groups), the same as for $\text{BQ}^{\bullet-}$. This is to be expected, from the similar extent and strength of hydrogen bonding. The other C-O bondlengths are

for the methoxy groups - $d(\text{O-CH}_3)$ is 1.48 Å in each case, and $d(\text{C}_{ortho}\text{-O})$ is 1.40 (OMe(1)) or 1.41 (OMe(2)) Å. This difference indicates that there is a certain double-bond character to the $\text{C}_{ortho}\text{-O}$ bond, implying delocalisation of a lone-pair into the π -system; but nothing like the double-bond character present in the carbonyl CO bonds.

As expected, the geometry around methoxy oxygen correlates with the corresponding dihedral angle. The methoxy group will be more able to delocalise its lone-pair away and become part of the π -system at lower than at higher dihedral angles, leading to increased sp^2 hybridisation at oxygen. The result is that on average, for $\tau = 0\text{-}45^\circ$, $\angle(\text{C-O-C}) = 121^\circ$ and $d(\text{C-O}) = 1.38$ Å; but for $\tau > 45^\circ$, $\angle(\text{C-O-C}) = 115^\circ$ and $d(\text{C-O}) = 1.40$ Å. The equivalent angle for the methyl side-group, $\angle(\text{CH}_3\text{-CH}_2\text{-C}_{ortho})$, averages 114° . As the OMe(1) group spends more of its time in the $\tau > 45^\circ$ region (85% of the time, as opposed to only 60% for OMe(2)), it is unsurprising that it has both smaller $\angle(\text{C-O-C})$ values (116° vs. 118°) and longer $\text{C}_{ortho}\text{-O}$ bondlengths (1.40 vs. 1.39 Å) than OMe(2).

The $\text{C}_{ortho}\text{-C}_{ipso}$ bondlengths are in the range 1.45-1.46 Å, while both $\text{C}_{ortho}\text{-C}_{ortho}$ bondlengths are equal to 1.39 Å, similarly to the case of $\text{BQ}^{\bullet-}$. The $\text{C}_{ortho}\text{-CH}_3$ and $\text{C}_{ortho}\text{-CH}_2\text{CH}_5$ bondlengths are 1.52 Å each, and the ethyl side-chain's $\text{CH}_2\text{-CH}_3$ bondlength is 1.56 Å.

6.5 Further simulation

It would be highly desirable to simulate several picoseconds more for the purpose of obtaining more statistically reliable results. Details regarding the asymmetry of the molecule are masked by the asymmetry of the conformation dominating our trajectory - which may be the preferred conformation, but our trajectory is too short to say. As mentioned, for the 6.4 ps trajectory of $\text{BQ}^{\bullet-}$, the number of hydrogen bonds to each carbonyl differs by 0.2 - an indicator of statistical noise, given that the molecule is formally symmetrical. We would like a comparable or greater accuracy for our studies of $\text{UQ}^{\bullet-}$. Additionally, the correlation of the number of hydrogen bonds to carbonyl oxygen with the number to methoxy oxygen, and with the orientation of the methoxy groups, is puzzling. Better data is required to confirm it, and more work to explain it.

Chapter 7

Dynamical EPR Parameters of Ubisemiquinone

7.1 Introduction

The vital role that ubisemiquinone plays in photosynthesis has seen it made the subject of numerous EPR studies *in vivo*, and a number of experiments have been published seeking to elucidate the immediate environment of the ubisemiquinone molecule from the g-tensor and HFC data.¹⁴¹⁻¹⁴⁴ We hope, when our trajectory is long enough, to have sufficiently accurate data to apply our insights to the cases of most interest, namely EPR data on the interaction of ubisemiquinone in the binding sites of the various enzyme systems it acts as a cofactor for. In this chapter, we present preliminary EPR data calculated from our MD trajectory and compare them to experimental solution-state data for $\text{UQ}^{\bullet-}$.

7.2 Computational details

EPR property calculations were performed on the first 1.9 ps of the aqueous $\text{UQ}^{\bullet-}$ CP-MD trajectory detailed in the previous chapter. Snapshots were taken every 10.2 fs from the trajectory and single-point electronic structure calculations were performed with the TURBOMOLE program.^{126,127} These were performed at the RI-BP86/DZVP^{17,21,57} level for g-tensor calculations (using an SVP auxiliary basis¹²⁸), and at the B3LYP/EPR-II^{17,18,25,30} level for the hyperfine coupling constants. The electronic structure details were then passed to the MAG/ReSpect program package⁶¹ for property calculation. Some of the calculations (labeled as such) were performed using a polarisable electric continuum (PCM)¹²⁹ to simulate the effect of the bulk

solvent.

Calculations were done on $\text{UQ}^{\bullet-} + \text{H}_2\text{O}$ clusters defined using the following criteria (see previous chapter for hydrogen bond definitions):

- **[lone]** indicates $\text{UQ}^{\bullet-}$ molecule alone, *sans* solvent molecules.
- **[O \cdots H]** includes all water molecules hydrogen bonded to oxygen. Hydrogen bonds only to specific oxygens are denoted by subscripts - $[\text{O}_{\text{CO}}\cdots\text{H}]$ for carbonyl, $[\text{O}_{\text{MeO}}\cdots\text{H}]$ for methoxy (we use the strict criteria defined in Chapter 6). For certain purposes we also consider a second to-methoxy criteria set, labelled $[\text{O}_{\text{MeO}}\cdots\text{H}](2)$, excluding water molecules H-bonded to carbonyl oxygen if the to-carbonyl distance criterion is raised to 2.7 Å.
- **[T-stacked]** includes all water molecules engaging in T-stacking hydrogen bonding (strict criteria).
- **[Total]** includes all water molecules engaging in any hydrogen bonding to $\text{UQ}^{\bullet-}$.
- **[x Å]** denotes a larger cluster including all water molecules within x Ångstroms of a ubisemiquinone oxygen or ring carbon.

7.3 g -Tensor calculations

The first calculations we performed were on the initial 1.0 ps with cluster sizes from [4.0 Å] to [4.75 Å], to examine convergence of the g -shift values with cluster size. Assuming that the x and y components were converging asymptotically on some infinite-water molecules value, we fitted an exponential function to determine the error involved. The results are listed in Table 7.1. We found that the [4.25 Å] value for Δg_x was within 50 ppm of the infinite limit, and [4.0 Å] within 100 ppm, and decided on [4.25 Å] as a reasonable cluster size for the entire trajectory.

Table 7.1: Size convergence of the g -tensor. Tensor components in ppm.

Size (Å)	Δg_x	Δg_y	Δg_z
4.00	4451	3052	172
4.25	4395	3033	180
4.50	4370	3029	166
4.75	4360	3020	162
Infinite limit	4352	3019	-

g-Tensor data for the full 1.9 ps treated is given in Table 7.2. The effects of T-stacking hydrogen bonding are positive, as in the case of BQ^{•-}, but somewhat smaller - +69 ppm compared to +195 ppm in g_x . This is approximately consistent with the fact that there are less than half as many such hydrogen bonds in this case. H \cdots O_{CO} interactions give a change in g_x of -1676 ppm for UQ^{•-}, far smaller than the -2349 ppm change for BQ^{•-}, in spite of the numbers of hydrogen bonds to carbonyl being the same in each case. We attribute this partly to the H-bonds being slightly longer in the case of UQ^{•-} (see discussion of RDF peak in previous chapter) and partly to the greater prevalence of out-of-plane hydrogen bonding, which decreases g_x less. A factor unique to UQ^{•-} is the effect of hydrogen bonding to methoxy oxygens.

Table 7.2: *g*-Tensor results for ubisemiquinone. All values in ppm.

Cluster criterion:	Δg_x	Δg_y	Δg_z	Δg_{iso}
lone	6473	3399	137	3336
lone+PCM	5768	3247	120	3045
T-stacking	6542	3423	144	3369
O _{MeO} \cdots H	6441	3402	141	3328
O _{MeO} \cdots H (2)	6477	3403	139	3339
O _{CO} \cdots H	4797	3081	101	2659
O \cdots H	4776	3083	107	2655
Total	4824	3109	115	2682
Total+PCM	4651	3080	109	2613
4.25Å+PCM	4355	3032	143	2506

We would expect that hydrogen bonding to O_{MeO} would, like T-stacking hydrogen bonding, decrease the negative charge located at the carbonyl oxygens (in the latter case, by localising it at the ring carbons, in the former case by preventing O_{MeO} from donating negative charge to the rest of the π -system). This would allow location of more spin density at carbonyl oxygen, increasing g_x . In fact, we see a combination of effects, and generally H-bonding to O_{MeO} *decreases* g_x and g_{iso} . The main reason for this is that water molecules attached to methoxy oxygens can generally be considered as weakly H-bonded to carbonyl oxygen as well: over 60% would fit the O_{CO} H-bonding criteria if the maximum $r[\text{H}\cdots\text{O}_{CO}]$ distance was extended to 2.7 Å.^a Therefore the effect of to-carbonyl hydrogen bonds - stabilisation of neg-

^a2.7 Å is not only the boundary between solvation spheres, as measured by the carbonyl oxygen RDF, but also the approximate distance between O_{CO} and the nearest O_{MeO}. In this discussion, then, as a rough rule of thumb, we are discussing whether the proton H-bonded to MeO is closer to the carbonyl oxygen than the methoxy oxygen is (whether

ative charge at oxygen, and the concomitant decrease of the g_x component - is shared by to-methoxy H-bonds too; the difference is one of degree: closely H-bonded water molecules have a far larger effect (a 1700 ppm decrease in g_x compared to the lone molecule), whereas the more distant (from O_{CO}) water molecules H-bonded to O_{MeO} decrease g_x by, on average, 32 ppm,^b and no more than 528 ppm at any time.

Previous static calculations, in contrast to our results here, found an increase in g_x on attaching hydrogen bonds to methoxy oxygens;⁸⁵ this is because they locate the H-bonded water (or isopropanol) molecule quite far from the carbonyl oxygen. (See Figure 5 of ref. 85, where the H-bond proton is certainly further than 2.7 Å away.)

As confirmation of this, we note that to-methoxy H-bonding not only causes both increased and decreased g_x at different times, but that increased g_x seems to correlate with distance from the nearest carbonyl oxygen. Inspection of those snapshots where hydrogen bonds to methoxy increase g_x shows the H-bonded water molecule to be far from the carbonyl oxygen. If we rerun the calculations with the criteria listed as $O_{CO}\cdots H(2)$ in Table 7.2 (excluding water molecules close to carbonyl oxygen), we find that g_x and g_y are slightly *increased* over the lone value. We also note that the addition of hydrogen bonds to methoxy makes virtually no difference when hydrogen bonds to carbonyl are already present - compare the values for the $[O_{CO}\cdots H]$ and $[O\cdots H]$ clusters.

(It may be asked why, if the Δg -reduction effects of solvent molecules are still significant at longer distances, this has not been remarked upon in conjunction with T-stacking hydrogen bonding. The answer is that T-stacking H-bonding does not have competing effects in the same way. It pulls negative charge towards the C_6 ring, which necessarily means pulling it away from the carbonyl oxygens; there is a single effect in play. To-methoxy H-bonding, however, both stabilises negative charge at O_{CO} while preventing O_{MeO} from donating more negative charge to the π -system: it has two competing effects.)

If we correlate the numbers of hydrogen bonds with the 4.25 Å+ PCM cluster g-values, we obtain the data shown in Table 7.3.

This data is in line with previous results: a near-consistent drop in Δg_x with increasing hydrogen bonding to carbonyl oxygen (the slight raise from 4 to 5 H-bonds is anomalous; we attribute it to statistical noise due to finite trajectory length), and an increase in Δg_x with T-stacking hydrogen bonding.

$$r[H\cdots O_{CO}] \leq r[O_{MeO}\cdots O_{CO}].$$

^bThe -32 ppm change is an average over all snapshots, including those where no to-methoxy H-bonding was detected and the change is 0 ppm. The average change over all snapshots where to-methoxy H-bonding is present is -48 ppm.

Table 7.3: Correlation of Δg_x with hydrogen bond number

N ^o . H-bonds	Δg_x ^[a] for given number of H-bonds of type:		
	O _{CO} ⋯H	O _{MeO} ⋯H	T-stacking
0	-	4427	4342
1	-	4357	4377
2	(4642)	4228	4372
3	4533	(4098)	(4472)
4	4274	-	-
5	4310	-	-
6	(4227)	-	-

[a] Δg_x data taken from 4.0 Å+ PCM cluster calculations. Brackets indicate data for an infrequently seen number of hydrogen bonds.

The correlation of Δg_x with to-methoxy H-bonding is negative, partly due to the factors detailed above, but partly also due to the fact (mentioned in the previous chapter) that to-methoxy H-bonding happens, in our trajectory, to coincide with to-carbonyl H-bonding. (If we correlate with to-methoxy H-bonding excluding all water molecules within 2.7 Å of carbonyl oxygens, the decrease is less: 4373 ppm for 0 H-bonds, 4350 ppm for 1 H-bond.) We presume that in a longer simulation, the correlation between numbers of hydrogen bonds to methoxy and to carbonyl will disappear, in which case the apparent relation between the former and Δg_x may change.

7.3.1 Comparison with other studies

To the best of our knowledge, no experimental data exists for aqueous UQ^{•-}, either the full molecule or model systems like ours. However, isopropanol data is available, and previous computational studies⁸⁵ have found that the difference is slight: for the UQ^{•-} + 4ROH system, the Δg_x component is 4436 ppm for water and 4320 ppm for ⁱPrOH, a difference of 116 ppm (which narrows to 1 ppm when hydrogen bonds to methoxy oxygen are included). We will compare our results with the ⁱPrOH data for UQ-3^{•-}.¹⁴⁵

As with benzosemiquinone, we overshoot the Δg_x component significantly, at 4355 ppm (experimental: 3900 ppm). This is a known problem and appears to be a systematic error in the DFT functional, correctable by scaling.⁸⁵ The Δg_y component we give as 3032 ppm, which is reasonably close to experiment (2940 ppm). Δg_z we continue to overestimate and get the sign of wrong (143 ppm vs. -220 ppm) for reasons that are unclear; we discussed this effect for BQ^{•-} in Chapter 5. Unlike in the case of BQ^{•-}, however, this

overestimate occurs with static calculations also.⁸⁵

The principal effects of dynamics on benzosemiquinone g-tensors were to increase the g_x component significantly compared to static calculations. We find this again in the case of ubisemiquinone: $\text{UQ}^{\bullet-} + 4\text{H}_2\text{O}$ (static calculation) has $\Delta g_x = 4436$,⁸⁵ whereas our $\text{O}_{\text{OC}}\cdots\text{H}$ cluster has $\Delta g_x = 4797$ ppm. As in the case of $\text{BQ}^{\bullet-}$, it indicates that static calculations benefit from error compensation - an overestimate caused by systematic errors in the BP86 functional is partly compensated by lack of dynamics. What is curious is that both errors seem to be smaller in the case of ubisemiquinone - the difference between experiment and our best dynamical value is about 500 ppm for $\text{UQ}^{\bullet-}$,^c but double that for $\text{BQ}^{\bullet-}$. The dynamical error for the first solvation sphere, on the other hand (approximately the difference between the prior $\text{Q}^{\bullet-} + 4\text{H}_2\text{O}$ simulation and our clusters with H-bonds to carbonyl oxygen) is of opposite sign, but again far smaller for $\text{UQ}^{\bullet-}$ (261 ppm) than for $\text{BQ}^{\bullet-}$ (875 ppm).

It would seem, at a rough guess, that the complexity of ubisemiquinone is leading to further error cancellation: that for both sources of error (assumption of static models and imperfection of the BP86 electronic structure), the errors are opposite for factors concerning the basic C_6O_2 structural unit and for factors concerning the $\text{UQ}^{\bullet-}$ sidechains.

We also note that, as mentioned above, hydrogen bonds to methoxy oxygen decrease g_x in our results, whereas static calculations find the opposite.⁸⁵ There is a balance of effects here, and that balance is clearly altered by dynamics. A static calculation locates H-bonds to O_{MeO} far enough from the carbonyl oxygen to increase g_x . However, on introduction of thermal motion, these H-bonds tend to get closer to the carbonyl oxygen, which pushes the balance of effects in favour of reduction of g_x . This difference is partly due to the fact that the static calculations have both OMe groups out of plane, approximately perpendicular to the ring; whereas simulation tends to have one out of plane and one in plane. Hydrogen bonds to an in-plane OMe group (pointing "inwards") will be much closer to the carbonyl oxygen, as the H-bond will point "outwards" rather than perpendicular to the ring.

^cThis is an extremely rough guess. The difference compared to experimental ⁱPrOH data is 455 ppm; the previous studies mentioned⁸⁵ indicate the difference compared to experimental aqueous data may be about 100 ppm smaller; the incomplete simulation might mean an additional few hundred ppm error either way.

7.4 HFC calculations

The hyperfine coupling constants, and Mulliken spin densities from the HFC calculations, are listed in Tables 7.4 to 7.6. The calculations performed were for the [Lone] and [4.0 + PCM] clusters. Of the dipolar coupling tensor, only the largest, parallel (\parallel) component is shown. We know of no experimental data in aqueous solution, and therefore make comparison against data for methanol, ethanol and isopropanol, in which experiments have been carried out.

Agreement with experiment seems to be passable. The C_{ipso} isotropic HFCs overshoot the alcoholic solution values by 2-3 MHz, most of which probably arises from comparison with the wrong solvent (for $BQ^{\bullet-}$, A_{iso} is larger by about 2 MHz for water than for ethanol). The 0.1 MHz difference between the two C_{ipso} sites is not reproduced by our calculations (we get the difference almost as large, but the wrong way round); although we would not expect our trajectory length to be sufficient for distinguishing such small differences in such a sensitive parameter. As with our $BQ^{\bullet-}$ simulation, this parameter is sizeably increased by the direct effects of solvation, as are the dipolar coupling and the Mulliken spin density.

$C_{ipso}(2)$, curiously, has a lower A_{iso} than $C_{ipso}(1)$, despite having a slightly higher Mulliken spin density and A_{\parallel}' . This is probably because $O_{CO}(2)$ has significantly more spin than $O_{CO}(1)$ (see Table 7.5), so the spin polarisation of the C_{ipso} -O bond (locating negative spin density at C_{ipso}) is stronger for $C_{ipso}(2)$ -O(2) than for $C_{ipso}(1)$ -O(1).

The A_{iso} values of C_{ortho} nuclei are far less sensitive than those of C_{ipso} , as found in previous calculations and Chapter 5 (we note that for $BQ^{\bullet-}$, the aqueous value is only 0.3 MHz less than for ethanol). The two C_{ortho} to which methoxy groups are attached both give rather different data - considerably lower A_{iso} and A_{\parallel} for C_{ortho} -OMe(1) than for C_{ortho} -OMe(2), as a result of the former having approximately half the spin density located at it than the latter. (We note that the difference between the two is almost unaltered by the direct effects of solvation.) This difference appears to arise from the conformation of the methoxy groups, which we discuss shortly. We assume that the HFC parameters would be considerably closer if the trajectory was longer. Solvation causes the spin density to decrease somewhat, in the same manner as seen for $BQ^{\bullet-}$; this acts to lower the A_{iso} value, as does the higher spin density on C_{ipso} in solution.

The A_{iso} values of the two C_{ortho} with organic substituents also differ; according to the experimental methanolic data they should, but only on the order of 0.2 MHz, indicating the 2.6 MHz difference to be due to insufficient trajectory length. The average value for the two nuclei agrees well

Table 7.4: Hyperfine coupling data for ring carbons (All A values in MHz. Mulliken spin densities $\times 10^{-3}$)

Position	A_{iso}	$A_{ }$	SD
$C_{ipso}(1)$			
lone	-3.8	17.6	81.9
4.0Å	5.4	29.2	165.2
exp., $^iPrOH^{146}$	2.7	27.9	
exp., $MeOH^{147}$	1.7		
$C_{ipso}(2)$			
lone	-6.2	17.2	75.6
4.0Å	4.7	30.2	167.9
exp., $^iPrOH^{146}$	3.7	28.5	
exp., $MeOH^{147}$	2.7		
$C_{ipso}(\text{average})$			
lone	-5.0	17.4	78.7
4.0Å	5.1	29.7	166.5
exp., $^iPrOH^{146}$	3.2	28.2	
exp., $MeOH^{147}$	2.2		
$C_{ortho}\text{-OMe}(1)$			
one	-2.9	8.5	47.7
4.0Å	-5.4	8.2	32.9
$C_{ortho}\text{-OMe}(2)$			
lone	0.4	12.6	72.1
4.0Å	-2.0	12.4	63.6
$C_{ortho}\text{-OMe}(\text{average})$			
lone	-1.3	10.5	59.9
4.0Å	-3.7	10.3	48.3
$C_{ortho}\text{-Et}$			
lone	1.5	14.4	91.2
4.0Å	0.0	13.2	73.2
exp., $MeOH^{147}$	(-)1.3		
$C_{ortho}\text{-Me}$			
lone	0.9	14.3	93.0
4.0Å	-2.6	10.9	59.3
exp., $MeOH^{147}$	(-)1.5		
$C_{ortho}\text{-CH}_2R(\text{average})^{[a]}$			
lone	1.2	14.3	92.1
4.0Å	-1.3	12.0	66.3
exp., $MeOH^{147}$	(-)1.4		

[a] I.e. average values of $C_{ortho}\text{-Me}$ and $C_{ortho}\text{-Et}$.

Table 7.5: Hyperfine coupling data for oxygens (All A values in MHz, Mulliken spin densities $\times 10^{-3}$.)

Position	Gas-phase			Aqueous		
	$-A_{iso}$	$-A_{\parallel}$	SD	$-A_{iso}$	$-A_{\parallel}$	SD
$O_{CO}(1)$	19.4	76.5	250.0	16.7	61.0	191.9
$O_{CO}(2)$	21.1	84.5	278.1	18.0	66.2	210.8
$O_{OMe}(1)$	1.9	1.8	2.5	1.9	2.8	5.8
$O_{OMe}(2)$	2.5	4.2	8.8	2.9	6.0	14.5
Average:						
O_{CO}	20.3	80.5	264.1	17.4	63.6	201.4
O_{OMe}	2.2	3.0	5.6	2.4	8.4	10.2

with experiment, however. We additionally note that whereas these two C_{ortho} centres have similar isotropic HFCs to $BQ^{\bullet-}$, the two C_{ortho} adjacent to methoxy groups have significantly lower spin densities and A_{iso} values. We attribute this to the fact that C_{ortho} with methoxy groups attached will be more electron-deficient than those with alkyl groups attached; this will favour resonance structures with negative charge, rather than an unpaired electron, located on them.

The oxygen HFC data are shown in Table 7.5. The isotropic HFCs of the carbonyl oxygens are of the same order of magnitude as our calculated $BQ^{\bullet-}$ values, which were somewhat too low compared to experiment. Presumably the same error would be seen if we had experimental data to compare with for $UQ^{\bullet-}$. More notably, we see an average of -2.2 MHz isotropic coupling, and positive spin density, at O_{OMe} . This indicates that, as shown in Figure 6.1 in the previous chapter, spin delocalisation onto the methoxy groups is significant. The amount of spin delocalised depends (albeit not particularly proportionally) on the amount of spin on the adjacent carbon - the oxygen with most spin is $O_{OMe}(2)$, which is adjacent to the C_{ortho} nucleus with the greater spin.

7.4.1 Side-chain HFCs

The side-chain carbon and hydrogen HFC data are shown in Tables 7.6 and 7.7. There is no formal delocalisation of the unpaired electron onto these nuclei, and spin density is located on them only as a result of spin polarisation and hyperconjugation. The pattern of spin polarisation is that spin density on one atom polarises a covalent bond so as to locate spin density of the opposite sign on an adjacent atom. Therefore, the positive spin density on

the C_{ortho} and O_{MeO} nuclei induces *negative* spin density on methyl carbon and the ethyl α -carbon.^d As a secondary, knock-on effect, positive spin density then becomes located on the α -hydrogens of the ethyl and methyl groups, and the ethyl β -carbon. (This is enhanced by hyperconjugation - see below.) In turn, this causes negative spin density to be located on the ethyl β -hydrogens, although by now the size of the effect is very small.

Spin polarisation is a difficult effect to model computationally, and therefore it is unsurprising that our values do not match experiment as well as the π -system nucleus HFCs. We somewhat overestimate the A_{iso} values of the methyl carbon, compared to the methanol value. The results for our α - ^1H HFCs are passable. Our results for the ethyl group (CH_2CH_3) compare fairly well to the experimental isopropyl ($\text{CH}_2\text{CH}=\text{CR}_2$) values; we even reproduce the difference between them, although overestimated slightly - one HFC is obtained accurately, the other is overshoot. α -proton (a) ($A_{iso} = 2.1$ MHz) is pointing "inwards", toward the methyl group; α -proton (b) ($A_{iso} = 4.8$ MHz) is pointing "outwards". We cannot evaluate the differences regarding the methyl proton HFCs, as they exchange positions frequently during the simulation.

The β -position HFCs from our calculations we list only for completeness; our model molecule ends in a CH_3 at the β position, whereas the full molecule continues with a $[\text{CHC}(\text{Me})\text{CH}_2\text{CH}_2]_n\text{CHCMe}_2$ isoprenyl chain. It is unsurprising, then, that these β proton HFC values differ.

Hyperconjugation appears to have a significant effect on the spin densities of those nuclei located significantly out of the plane of the π -system, as the data for these atoms cannot be explained on the basis of spin polarisation alone. The polarisability of the C_{ortho} - CH_2R bond is such that a given amount of spin at C_{ortho} induces a spin density at C_α a little less than a tenth as large (and of opposite sign). However, the spin density at the terminal β carbon of the ethyl group is almost as large as the spin density at C_α . Similarly, the spin density at the methoxy carbons should be negative due to spin polarisation, but in fact is positive for 62% of the time (and positive, but very small, overall). The methoxy hydrogen spin densities also fluctuate significantly, and are likewise positive overall, and even smaller than the methoxy carbon spin densities. (We overestimate the methoxy proton HFCs by 0.5 MHz, if the ethanolic data is good for comparison.)

A strong indicator that hyperconjugation is involved is the fact that the β -carbon spin density correlates with torsional angle, as shown in Table 7.8.

^dWe here, and in Table 7.7, follow the convention of labelling carbons immediately attached to C_{ortho} as the α -carbon. Carbons attached to α -carbons are β -carbons, etc. Hydrogens take the labelling of the carbon they are attached to.

Table 7.6: Methoxy group hyperfine data (all A values in MHz, Mulliken spin densities $\times 10^{-3}$).

Position	A_{iso}	A_{\parallel}	SD
$C_{OMe}(1)$			
lone	2.1	0.8	0.7
4.0Å	1.0	0.8	0.9
$C_{OMe}(2)$			
lone	2.5	0.8	0.9
4.0Å	1.4	0.8	0.8
$C_{OMe}(\text{average})$			
lone	2.3	0.8	0.8
4.0Å	1.2	0.8	0.9
exp., MeOH ¹⁴⁷	<0.3		
$H_{OMe}(1)$			
lone	0.0	1.8	0.0
4.0Å	0.2	1.8	0.1
$H_{OMe}(2)$			
lone	0.5	1.6	0.3
4.0Å	0.9	1.7	0.4
$H_{OMe}(\text{average})$			
lone	0.3	1.7	0.1
4.0Å	0.6	1.8	0.3
exp., ⁱ PrOH ¹³³	0.1	0.5	

Table 7.7: Alkyl group hyperfine data (all A values in MHz, Mulliken spin densities $\times 10^{-3}$).

Position	A_{iso}	A_{\parallel}	SD
$C_{\alpha}(\text{Et})$			
lone	-3.8	0.7	-6.2
4.0Å	-3.3	0.7	-6.3
$C_{\alpha}(\text{Me})$			
lone	-4.0	0.8	-8.4
4.0Å	-3.0	0.7	-5.3
exp., MeOH ¹⁴⁷	(-)4.8		
$C_{\alpha}(\text{average})$			
lone	-3.9	0.7	-7.3
4.0Å	-3.1	0.7	-5.8
$C_{\beta}(\text{Et})$			
lone	6.2	0.9	2.5
4.0Å	4.8	1.1	4.2
$H_{\alpha}(\text{Et})$			
lone	3.1	2.7	1.3
4.0Å	3.5	2.7	1.4
exp., EtOH ¹⁴⁸	2.8		
exp., ⁱ PrOH ¹³³	2.9		
$H_{\alpha}(\text{Et})(a)$			
4.0Å	2.1	2.1	0.8
exp., EtOH ¹⁴⁸	2.1		
$H_{\alpha}(\text{Et})(b)$			
4.0Å	4.8	3.2	19.0
exp., EtOH ¹⁴⁸	3.1		
$H_{\alpha}(\text{Me})$			
lone	5.5	2.7	2.1
4.0Å	4.9	2.6	1.9
exp., EtOH ¹⁴⁸	5.8		
exp., ⁱ PrOH ¹³³	6.0	2.5	
$H_{\beta}(\text{Et})$			
lone	-0.1	1.8	-0.1
4.0Å	0.0	1.8	-0.1
exp., ⁱ PrOH ¹³³	-0.3		

When in-plane, the methoxy carbons have negative spin density, as expected from spin polarisation effects. The spin density becomes positive, however, as the torsional angle becomes larger. The ethyl group is not at any point really "in-plane"; however, the same correlation is seen, with the highest HFC value when perpendicular to the ring.

Table 7.8: Correlation of C_β HFCs with torsional angle (A_{iso} in MHz)

$\tau^{[a]}$	$A_{iso} (C_\beta)$		
	MeO(1)	MeO(2)	Et
0-15°	-1.8	-1.8	
15-45°	0.2	-0.1	1.6
45-75°	0.7	2.2	4.2
75-90°	1.8	1.9	4.4

[a] As our interest here is solely in how perpendicular to the plane a particular group is, we have here taken the absolute values of τ and taken $\tau > 90^\circ$ as $(180 - \tau)$.

7.4.2 Solvent HFCs

The solvent HFC data of $BQ^{\bullet-}$ is very similar for isopropanol¹³³ and for water,⁸⁰ with only 0.1 MHz difference between the A_{iso} and dipolar tensor component values. We assume, then, that iPrOH data can thus be used to assess calculated solvent HFCs for $UQ^{\bullet-}$ also.

In the case of $UQ^{\bullet-}$, solvent protons H-bonded to carbonyl oxygen have $A_{iso} = 1.1$ MHz and $A'_{||} = 4.7$ MHz. In the case of $BQ^{\bullet-}$, these numbers are, respectively, 0.2 and 5.9 MHz.¹³³ This is an interesting result: for $UQ^{\bullet-}$, dipolar coupling between the unpaired electron and solvent protons is weaker, but the amount of spin delocalised onto the solvent protons is apparently greater. Weaker dipolar coupling may arise because the RDF maximum is at a longer distance and the spin at carbonyl oxygen is smaller on $UQ^{\bullet-}$ (compare Tables 5.5, 7.5). The greater spin delocalised onto solvent protons of $UQ^{\bullet-}$ is probably because $UQ^{\bullet-}$ has more out-of-plane hydrogen bonding, and spin delocalisation can *only* occur onto out-of-plane protons due to the symmetry of the SOMO.

Unfortunately, our calculations are not useful here, as they fail to show any significant difference between the two semiquinones. This is seen in Figure 7.1, in which A_{iso} values are plotted against $r[O\cdots H]$ for nearby solvent protons. The *highest* A_{iso} value seen in the case of $UQ^{\bullet-}$ is 0.7 MHz, falling short of the experimental isopropanol value. The running average is below

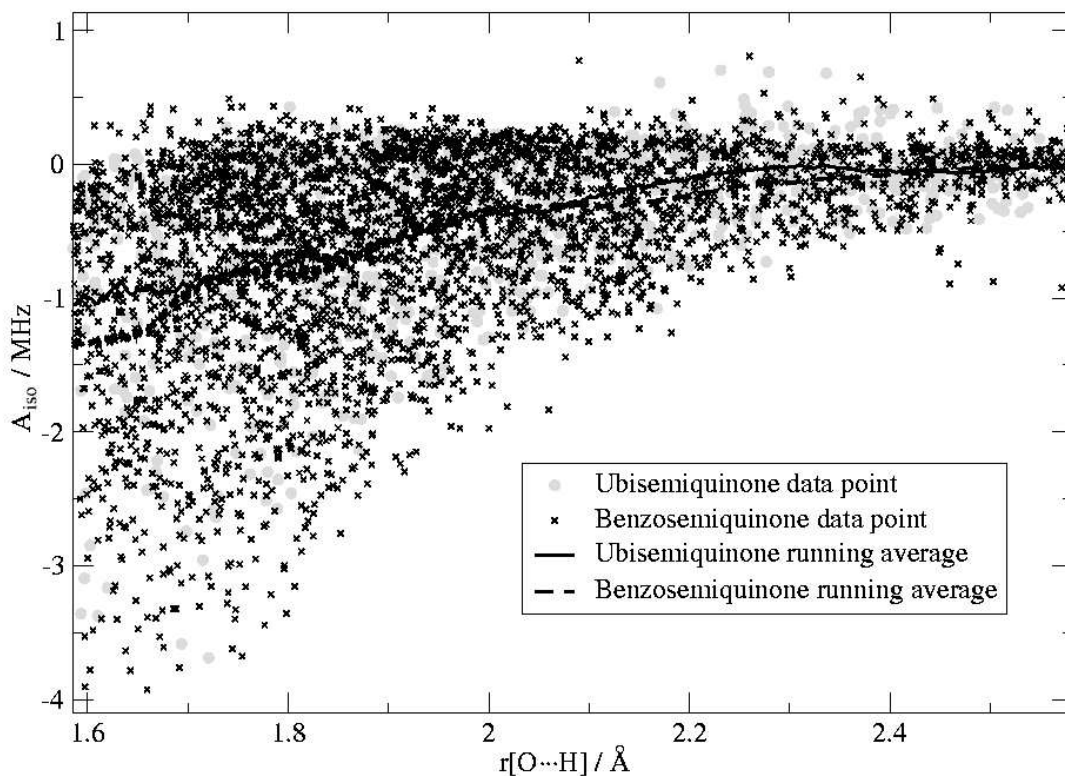


Figure 7.1: Plot of solvent proton isotropic HFCs against distance for $\text{BQ}^{\bullet-}$ and $\text{UQ}^{\bullet-}$.

zero for the region in which most hydrogen bonding occurs, and the experimental difference between the two semiquinones is not reproduced at all.

We presume, as with benzosemiquinone, that the error lies with the DFT methodology used. The A_{iso} values involved are small, and the balance between spin delocalisation and spin polarisation difficult to strike, so a certain lack of accuracy is unsurprising. However, that the qualitative difference between the two systems should not be reproduced is disappointing.

Happily, our dipolar coupling values are more accurate. In Figure 7.2, we show frequency graphs for the large component of the dipolar HFC coupling tensor for $\text{BQ}^{\bullet-}$ and $\text{UQ}^{\bullet-}$. It can be seen that the $\text{BQ}^{\bullet-}$ frequency distribution appears to peak at about 6 MHz (experimental values: 5.9 MHz ($i\text{PrOH}$)¹³³ and 6.0 MHz (water)⁸⁰). For $\text{UQ}^{\bullet-}$, the precise location of the peak is unclear, due to insufficient data; however, it appears to be around 4–4.6 MHz (experimental value: 4.7 MHz in $i\text{PrOH}$).¹³³ The difference between

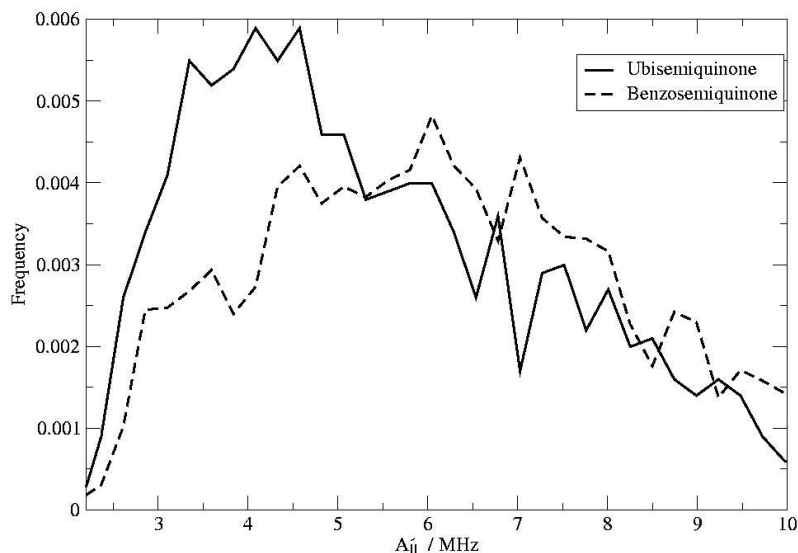


Figure 7.2: Frequency plot of solvent proton $A_{||}'$ for $\text{BQ}^{\bullet-}$ and $\text{UQ}^{\bullet-}$.

$\text{BQ}^{\bullet-}$ and $\text{UQ}^{\bullet-}$ is reproduced very accurately.

We additionally note that the average HFC values for protons involved in T-stacking hydrogen bonding (loose criteria; i.e. 0.7 per snapshot) are: $A_{iso} = -1.3$ MHz, with the A components equalling 2.9, -0.9 and -2.0 MHz. These values are within 0.2 MHz of those found for benzosemiquinone.

7.5 Further Work

As mentioned in the previous chapter, we hope to simulate a much longer trajectory in order to cover as much of the conformational phase space as possible, and to reduce the level of statistical uncertainty in our results. In particular, we would like to analyse the EPR data with respect to H-bonding configurations, as recently done with static calculations to analyse the H-bonding situation of $\text{UQ}^{\bullet-}$ in quinol oxidase.¹²¹ Such studies provide detailed and potentially highly useful insight into the dependence of EPR parameters on hydrogen bonding. Unfortunately, we would need a much longer trajectory to be able to offer good quality data here.

Chapter 8

Summary

Electron Paramagnetic Resonance (EPR) spectroscopy is an important method for detecting and investigating paramagnetic species. The electronic g -tensor and hyperfine coupling are highly sensitive to changes in the spin density of the system, and are hence very useful for characterising a radical and building up a picture of its spin density distribution. The technique has a wide variety of applications across various fields, from tracking radicals in solid state physics to characterising paramagnetic metalloenzyme reaction centres in bioinorganic chemistry.

Computational simulation of EPR parameters is a very useful tool for interpreting EPR spectra, and likely to increase in importance as ever more computational power and improved theoretical methods become available. Density Functional Theory (DFT)-based approaches are widely used for this purpose, as DFT allows electronic structure to be calculated with inclusion of correlation effects, without the computational cost of post-Hartree Fock methods. Property calculations on the Kohn-Sham orbitals can then yield g -, hyperfine or zero-field splitting tensors, as well as a range of other magnetic resonance parameters obtainable via DFT.³

One approximation often made in theoretical studies is that the properties of a system can be obtained from a static calculation, i.e. a calculation using a single structure, normally optimised to lie at an energy minimum. This amounts to calculating the properties of the system at absolute zero. This is generally not too drastic an approximation, and gives useful insight into the system under examination. However, there exist many cases where thermal motion is important, and some alternative approach, or at least correction, needs to be applied. This can be as simple as identifying the most important degree of freedom and making *ad hoc* corrections - mapping the potential energy well and making an informed estimate of the effects of thermal motion - or as complex as molecular dynamics, which explicitly simulates the motion

of a system over time.

In this thesis I present EPR parameter calculations for radical systems in which the effects of thermal motion are important, using DFT-based methodologies to obtain the hyperfine coupling (HFC) tensor and the electronic g -tensor. The effects of dynamics on the structure and EPR parameters of the systems studied have been assessed.

In chapter 3, I present our work on hydrogen atoms trapped in silasesquioxane cages ($\text{H@R}_8\text{Si}_8\text{O}_{12}$, or H@RT_8). These systems have positive g -shifts,⁴⁶ indicating delocalisation of spin onto the cage, as sizeable spin-orbit coupling cannot occur at hydrogen. We calculated and analysed the g -shifts and H and Si HFC constants for several H@RT_8 systems. We reproduced the positive g -shifts and their trends. Analysis showed that some spin density is delocalised onto cage oxygen p -orbitals, where spin-orbit coupling gives rise to positive Δg . Excitation analysis revealed that the largest contributions were from excitations of two triply-degenerate sets of $\beta - t_{1g}$ orbitals to the unoccupied β -SOMO. Both t_{1g} orbital groups are p -like at oxygen. These excitations dominate the $\Delta g_{SO/OZ}$ term and mirror the trends in that term. Atomic analysis of $\Delta g_{SO/OZ}$ revealed that the dominant oxygen contributions seem to decrease with increasing electronegativity of the R group, although the reason for this was not entirely clear. Substituent contributions are negative, and small for first-row elements. For halogenated H@RT_8 , substituent contributions become significant when heavier elements are involved, with overall negative Δg_{iso} predicted for $\text{R} = \text{Br}, \text{I}$. Calculations were performed using several DFT functionals.

The dynamics of the H@RT_8 system were examined by calculating the potential energy well of the trapped hydrogen atom and fitting a harmonic oscillator model. From this we estimated the effects of thermal motion on the EPR parameters when going from 0 to 300 K. The g -tensor changes by less than the experimental error, matching the empirical observation of its independence on temperature.⁶² The effect on the isotropic HFC of the central hydrogen is to decrease it by 2.7 MHz, close to the experimental decrease of 3-4 MHz.⁶²

In chapter 4, I report the performance of Car-Parrinello Molecular Dynamics (CP-MD)³¹ on benzosemiquinone radical anion and neutral benzoquinone, both in gas phase and in aqueous solution, at 300 K. We found that hydrogen bonding to benzosemiquinone oxygens is more extensive in our 300 K simulated system than is generally assumed in static calculations - 4.7 hydrogen bonds (with $r[\text{O}\cdots\text{H}] < 2.25 \text{ \AA}$), rather than the 2-4 H-bonds generally assumed in quantum chemical studies.^{85,90,79,83,131,134,84} We also found that significant amounts of "T-stacked" hydrogen bonding to the π -system occur, with an average of 1.1 such hydrogen bond identifiable per snapshot. We

further analysed the frequency of certain hydrogen bonding situations occurring: the most common numbers of hydrogen bonds to oxygen are 4 and 5, and the most common H-bond configuration is 2 H-bonds to one oxygen and 2 or 3 to the other. The most common number of T-stacked H-bonds is 1.

In the neutral BQ system, by contrast, hydrogen bonding is weaker, with an average of 2.4 H-bonds to carbonyl oxygen; the most frequent situations are 2 or 3 hydrogen bonds to oxygen, with 1 hydrogen bond to one oxygen and 1 or 2 to the other. The most common number of T-stacked H-bonds identified is 0, and the T-stacking interaction appears too weak to be considered a proper hydrogen bond. Radial distribution functions (RDFs) of to-oxygen H-bonding protons show BQ to have a far smaller maximum value of $g(r)$, and the RDF peaks at a higher value - 1.9 Å for BQ, compared to 1.75 Å for BQ^{•-}. (These distances match prior computational studies and experimental data⁸⁰ well.)

The influence of solvation and oxidation state on the geometry was also examined. Reduction from BQ to BQ^{•-} leads to a lengthening of the C-O and C_{ortho}-C_{ortho} double bonds (each of which gains more single-bond character) and a shortening of the C_{ipso}-C_{ortho} single bonds (which gain more double-bond character). This could be easily explained in resonance structure terms, and also from the shape of the BQ^{•-} SOMO. For both BQ and BQ^{•-}, solvation lengthens the C-O bond and shortens all C-C bonds; the change in bondlengths is greater in the case of the anion.

Chapter 5 presents EPR data calculated from our MD simulation by running property calculations on snapshots taken from the MD trajectory at regular intervals. As with static calculations using the same methodology,^{85,90} the largest (g_x) component is still overestimated by several hundred ppm; inclusion of dynamics makes the error worse, indicating that static calculations benefit from error cancellation. The bulk of the error is attributed to deficiencies in the DFT functional used. The g_y component is estimated accurately; g_z is larger than the low-temperature experimental values (and static calculations), due to dynamical factors which are significant at 300 K - deviation of the C-O groups from planarity being possibly the most important. The dependence of the g-tensor on C-O bondlength is clearly seen in the time-evolution of the principal components of Δg : C-O bond stretching vibrations show up as strong oscillations in Δg_x , and weaker oscillations in Δg_y . Solvent effects on the g-tensor were analysed, and it was found that over 75% of the effect of the bulk solvent was recoverable by including only the first solvation shell in the calculation. These solvent effects occur not only directly, due to influence of hydrogen bonding and dielectric continuum on the BQ^{•-} MOs, but also indirectly, due to influence of solvation on the geometry, particularly the C-O bond length.

Hyperfine coupling data, both isotropic and dipolar, was calculated and presented for all nuclei of $\text{BQ}^{\bullet-}$. Analysis of the effects of solvation on HFCs and Mulliken spin density provided a fuller picture of how the spin density distribution is affected by interaction with the solvent. Agreement with experiment was found to be reasonably good. Hyperfine data was also calculated and compiled for the hydrogen atoms of nearby solvent molecules. The isotropic HFCs were underestimated, indicating that the DFT functional used was not getting the balance right between spin polarisation and spin delocalisation effects. Dipolar hyperfine coupling data was closer to experiment, however, and by relating experimental dipolar data to our own, we put forward a possible explanation of why ENDOR experiments find only 4 hydrogen bonds to oxygen, whereas our simulations find more. We additionally note that, according to our calculations, the hyperfine coupling signals of T-stacked H-bonding protons would be in places overlaid by far stronger ^1H signals. We fitted dipolar data to a point-dipole model, and found that this model works well for in-plane hydrogen bonding. For out-of-plane H-bonding, it causes a substantial overestimate of the spin density on oxygen.

In chapter 6 we present analysis of CP-MD simulations performed on aqueous ubisemiquinone radical anion (with the isoprenyl group truncated to ethyl) at 300 K. Due to computational cost, we could not obtain as long a simulation length as we would like, and hope to extend the simulation.

The hydrogen bonding situation for $\text{UQ}^{\bullet-}$ is more complex than for $\text{BQ}^{\bullet-}$. The number of hydrogen bonds to carbonyl oxygens is 4.6 - about the same as for benzoquinone. Hydrogen bonds to the C_6 ring are fewer in number (0.7 or 0.5, depending on criteria), due to steric obstruction from the side groups. Additionally, hydrogen bonding to the methoxy groups is present, with an average of 0.9 such H-bonds being found at any time. Due to steric interaction with the side-chain, hydrogen bonds to carbonyl are longer than for $\text{BQ}^{\bullet-}$ - the RDF peak for such protons is broader and has a maximum value at around 1.9-1.95 Å.

By studying the variation of hydrogen bonds found with angular criteria, we plotted the directionality of all hydrogen bond types, for $\text{UQ}^{\bullet-}$, $\text{BQ}^{\bullet-}$ and neutral BQ. By showing how strongly nearby hydrogens are oriented towards the H-bond acceptors involved, this presents an additional way of judging hydrogen bond strengths. Hydrogen bonds to carbonyl are approximately the same strength for both $\text{BQ}^{\bullet-}$ and $\text{UQ}^{\bullet-}$, and somewhat weaker for neutral BQ. H-bonds to the methoxy groups of $\text{UQ}^{\bullet-}$ are weaker still. T-stacked hydrogen bonds to $\text{UQ}^{\bullet-}$ are *stronger* than to $\text{BQ}^{\bullet-}$ (due to methoxy groups donating negative charge to the ring), and seem about as strong as H-bonds to methoxy groups. T-stacking interactions with neutral BQ are very weak.

Orientation-wise, the two methoxy side groups do not behave the same,

with the MeO group opposite Et being on average significantly more out of plane than the other; this may reflect the short trajectory length, however. Hydrogen bonding to an MeO group seems to be correlated with that group being more in plane and pointing towards the other methoxy group. Some correlation is seen between methoxy conformations and hydrogen bonds to carbonyl, but not of the kind expected; further work will be required to clarify this. The ethyl group is aligned perpendicular to the plane of the ring.

In chapter 7 we present g -tensors and hyperfine coupling constants calculated for aqueous $\text{UQ}^{\bullet-}$, in the same manner as for $\text{BQ}^{\bullet-}$. The effects of H-bonding to carbonyl oxygens and the C_6 ring on the g -shifts were the same as for $\text{BQ}^{\bullet-}$. Hydrogen bonding to methoxy oxygens has competing effects, the balance of which depends on how close the water molecule is to the nearest carbonyl group. If far from the carbonyl group (about 3 Å), the effect is to increase Δg_x , similar to T-stacked hydrogen bonds; but closer, the water molecule has the effect of stabilising negative charge at carbonyl oxygen, decreasing Δg_x . As with $\text{BQ}^{\bullet-}$, the Δg_x value is overestimated by several hundred ppm compared to experiment.

The calculated isotropic hyperfine coupling constants do not match experimental data as well as for $\text{BQ}^{\bullet-}$, although the trajectory length is insufficient to make them very reliable. Agreement with dipolar coupling data is generally good, however. Analysis of the side-chain HFCs and spin densities shows significant hyperconjugation of the SOMO with the side group orbitals. This leads to larger positive spin densities at γ -carbons than would be expected merely from spin polarisation - but only when these groups are significantly out-of-plane; the effect is negligible in-plane. For solvent proton HFCs, A_{iso} is once again generally underestimated; and the experimental differences in solvent proton A_{iso} values for $\text{UQ}^{\bullet-}$ and $\text{BQ}^{\bullet-}$ ¹³³ are not reproduced by our calculations, which find no significant differences between the two semiquinones.

In summary, g -tensors and hyperfine coupling data have been calculated and analysed for several paramagnetic systems with inclusion of dynamics both in an *ad hoc* manner and with full inclusion of dynamics, using MD. Our work was the first to apply MD techniques to calculating the electronic g -tensor. We hope to extend our simulation of ubisemiquinone and extract more information from it; after this, the techniques developed may be applied to other semiquinones, or larger protein systems. Our results in chapter 4 indicated that QM/MM may be a good substitute for fully *ab initio* MD for aqueous semiquinones, and further comparison may be worthwhile.

As mentioned in Chapter 1, MD has previously been used to calculate HFCs for other radicals,⁵⁻⁷ although the field is in an early stage due to

the computational costs involved. Since our publication^{66,67} of the g -tensor analysis of $\text{BQ}^{\bullet-}$ presented in Chapter 5, the group of V. Barone *et al.* has extended the methodology to g -tensors, further demonstrating the utility of the MD-EPR technique.⁴

Chapter 9

Zusammenfassung

Elektronische Spin Resonanz (Electron Paramagnetic Resonance, EPR) Spektroskopie ist eine wichtige Methode zur Untersuchung paramagnetischer Systeme. Die Hyperfeinkopplungskonstante und der elektronische g -Tensor sind sehr empfindlich gegenüber Veränderungen der Spindichte eines Systems und deshalb sehr nützlich zur Charakterisierung eines Radikals und Abbildung seiner Spindichte. So lässt sich die elektronische Spin Resonanz in sehr unterschiedlichen Forschungsgebieten einsetzen beispielsweise als Nachweismethode für Radikale in der Festkörperphysik und zur Charakterisierung paramagnetischer Metalloenzymreaktionszentren in der bioanorganischen Chemie.

Die theoretische Berechnung von EPR Parametern stellt darüber hinaus eine sehr hilfreiche Methode zur Interpretation von EPR Spektren dar, die aufgrund der zukünftig zur Verfügung stehenden Rechnerleistung und theoretischen Techniken weiter an Bedeutung gewinnen wird. In diesem Zusammenhang finden Dichtefunktionaltheorie (DFT) basierte Methoden häufig Anwendung, da sie gegenüber post-Hartree-Fock Methoden zum einen Korrelationseffekte berücksichtigen und sich zum anderen mit sehr viel geringerem rechnerischem Aufwand nutzen lassen. Anhand der durch DFT-Simulation erhaltenen Kohn-Sham-Orbitale lassen sich dann magnetische Eigenschaften wie g -Tensoren und Hyperfein- und Nullfeldkopplung ("Zero-Field Splitting", ZFS) zur Charakterisierung eines Systems berechnen.³

Eine häufig verwendete Näherung der Quantenchemie ist die Berechnung der Systemeigenschaften nur durch statische Rechnungen, d.h. basierend auf einer einzelnen, zur niedrigsten Energie hin optimierten Struktur. Dies ist gleichbedeutend mit einer Berechnung bei 0 K, was gewöhnlich zur Charakterisierung völlig genügt und einen ausreichend genauen Einblick in die Eigenschaften des Systems ermöglicht. In Fällen, in denen die thermische Bewegungen jedoch eine Rolle spielt, muss eine andere Methode benutzen oder zusätzliche Korrekturen vorgenommen werden. Als einfachste Korrekturmög-

lichkeit lässt sich das harmonische Oszillatormodell auf die wichtigsten Freiheitsgrade anwenden. Die Energiekurven der Freiheitsgrade werden berechnet, eine x^2 Kurve dazu angepasst und die typische Abweichung vom Gleichgewicht bei einer gewünschten Temperatur abgeschätzt. Die beste Methode (innerhalb der Born-Oppenheimer Näherung) stellt jedoch die Molekulardynamik dar, in der man explizit die Kernbewegungen simuliert.

In dieser Arbeit stelle ich EPR-Parameterrechnungen für paramagnetische Systeme vor, in denen die Effekte thermischer Bewegungen von Bedeutung sind. Zudem wird der Einfluss der Kerndynamik auf die geometrische Struktur und die Parameter der Radikale untersucht unter Verwendung einer DFT-basierten Methode zur Berechnung der HFC- und g -Tensoren.

In Kapitel drei, präsentiere ich unsere Arbeiten zu in Silasesquioxankäfig gefangenen Wasserstoffatomen ($\text{H@R}_8\text{Si}_8\text{O}_{12}$, oder H@RT_8). Diese Systeme zeigen im Experiment unerwartet positive g -Verschiebungen,⁴⁶ die gleichzusetzen sind mit einer signifikanten Delokalisierung der Spindichte zu den Sauerstoffatomen des Silasesquioxans hin. Wir haben die g -Werte und die Hyperfeinkopplungen für Wasserstoff- und Siliziumatome berechnet und für einige H@RT_8 Systeme analysiert. Unsere Rechnungen konnten sowohl die positiven g -Verschiebungen als auch ihre Richtungen korrekt wiedergeben. Die Analyse zeigt, dass die Spindichte über die p -Orbitale der Käfigsauerstoffatome delokalisiert ist, an denen die Spinbahnkopplung dann eine positive g -Verschiebung ergibt.

Durch Analyse der Anregungen können wir zeigen, dass die größten Beiträge der g -Verschiebung auf Anregung von zwei dreifach-entarteten Orbitalen in das unbesetzte β -SOMO zurückzuführen sind. Beiden β - t_{1g} Orbitalgruppen weisen p -Charakter am Sauerstoff auf. Diese Anregungen dominieren den gesamten $\Delta g_{SO/OZ}$ Beitrag und spiegeln die Tendenzen des gesamten $\Delta g_{SO/OZ}$ -Terms wider. Den größten Beitrag weisen hierbei die Sauerstoffatome auf, wobei dieser mit höherer Elektronegativität abnimmt. Der Grund dafür ist bislang unklar. Substituentenbeiträge sind negativ und (für Elemente der ersten Reihe des Periodensystems) sehr klein. Für halogenierte H@RT_8 Systeme aber werden die Beiträge der Substituenten wichtiger für schwere Elemente und für $\text{R} = \text{Br}$ oder I sagen wir voraus, dass die gesamte g -Verschiebung negativ ist.

Die Dynamik der H@RT_8 Systeme wurde durch Berechnung der Potentialkurve des eingeschlossenen H-Atoms und anschließende Anpassung an ein SHO Modell untersucht. Auf diese Weise haben wir die Effekte thermischer Bewegungen abgeschätzt. Zwischen 0 und 300 K verändert sich der g -Wert weniger als der Fehler der experimentellen Werte, in Übereinstimmung mit empirischen Studien zur Temperaturunabhängigkeit der g -Verschiebung.⁶² Die Auswirkung auf die isotrope HFC des zentralen Sauerstoffatoms ist eine

Verringerung um 2.7 MHz - vergleichbar mit der empirischen Abnahme um 3-4 MHz. Für Berechnungen der g - und HFC-Werte wurden verschiedene DFT-Funktionale verwendet; Hybridfunktionale haben sich als geeignetste Methode erwiesen.

Im vierten Kapitel werden Car-Parrinello Molekular-dynamik-Simulationen (CPMD)³¹ für Benzochinon und das paramagnetische Benzosemichinonanion beschrieben, beide in wässriger Lösung sowie in der Gasphase bei 300 K. Laut unseren Rechnungen liegen mehr Wasserstoffbrückenbindungen in unserer simulierten 300 K Lösung vor als normalerweise in statischen Rechnungen vorausgesetzt wird: im Durchschnitt 4.7 H-Brückenbindungen (für $r[\text{O}\cdots\text{H}] < 2.25 \text{ \AA}$), wo quantenchemische Studien nur zwei oder vier annehmen.^{79, 83-85, 90, 131, 134} Auffällig sind zudem die "T-stacked" H-Brücken zum π -System, im Schnitt treten 1.1 dieser H-Brücken auf. Zudem haben wir die Häufigkeiten besonderer H-Brückenbindungen über den simulierten Zeitraum untersucht: für O \cdots H Wechselwirkungen werden gewöhnlich vier oder fünf H-Brückenbindungen beobachtet, zwei zu einem Sauerstoffatom und zwei oder drei zu dem jeweils anderen; darüber hinaus tritt meist nur eine "T-stacking" H-Brückenbindung auf.

Im Gegensatz dazu sind Wasserstoffbrücken im neutralen BQ-System mit nur 2.4 H-Brückenbindungen zum Sauerstoffatom im Durchschnitt seltener. Meist lassen sich nur zwei oder drei H-Brücken zu den Sauerstoffatomen finden. Identifizierbare "T-stacking" Wasserstoffbrücken kommen selten vor und die Wechselwirkung scheint in diesen Fällen zu schwach, um als echte Brückenbindung klassifiziert zu werden. Die radialen Verteilungsfunktionen (Radial Distribution Functions, oder RDFs) der gebundenen Protonen zeigen ein viel kleineres Maximum der RDF für BQ als für BQ \bullet - und jenes Maximum der RDF liegt bei einem höheren Abstand (1.9 \AA) als für BQ \bullet - (1.75 \AA). Diese Abstände stimmen mit früheren theoretischen und experimentellen Untersuchungen⁸⁰ gut überein.

Wir haben auch den Einfluss von Lösungsumgebung und Oxidationszustand auf die Struktur untersucht. Reduktion von BQ nach BQ \bullet - verlängert die C-O- und C_{ortho}-C_{ortho}- Doppelbindungen (höherer Einzelbindungscharakter) und verkürzt die C_{ipso}-C_{ortho}- Einzelbindungen (die Doppelbindungen ähnlicher werden). Diese Beobachtungen lassen sich durch Resonanzstrukturen und die Gestalt des SOMOs leicht erklären (die Veränderung der Bindungslänge wird durch den bindende bzw. antibindende Charakter des SOMOs bestimmt). In Lösung wird für BQ und BQ \bullet - die C-O-Bindung verlängert und alle C-C-Bindungen verkürzt. Die Veränderung ist jedoch im Fall des Anions größer.

Im fünften Kapitel werden mithilfe von MD-Simulation berechnete EPR Daten präsentiert, welche aus in regelmäßigen Abständen aufgenommenen

Schnappschüssen erhalten wurden. Nach derselben Methode wie für statische Rechnungen^{85,90} wird die größte Komponente des g -Tensors, Δg_x , um einige hundert ppm überschätzt. Die Abweichung ist jedoch größer für unsere dynamisch-berechneten Werte, was bedeutet, daß bei statischen Rechnungen offensichtlich Fehler kompensiert werden. Wir glauben, dass diese Fehler meistens durch Ungenauigkeiten des Dichtefunktional entstehen. Die Δg_y Komponente wird relativ exakt wiedergegeben; Δg_z ist größer als vergleichbare berechnete Werte sowie die experimentellen Werte (insbesondere die Verzerrung der C-O Gruppen aus der Ebene des Moleküls heraus).

Die Abhängigkeit des g -Tensors vom C-O-Bindungsabstand ist eindeutig sichtbar in der Zeitentwicklung des g -Tensors: C-O-Schwingungen zeigen sich deutlich als starke Oszillationen in Δg_x , und entsprechend schwächer in Δg_y . Lösungsmittelleffekte auf den g -Tensor wurden analysiert und wir fanden, dass mehr als 75 % des Lösungsmittelleffekts nur durch die erste Lösungsmittelschale simulierbar ist. Das Lösungsmittel wirkt aber nicht nur direkt auf die MOs des Semichinons, sondern auch indirekt durch den Einfluß auf die geometrische Struktur, besonders den C-O-Bindungsabstand.

In Kapitel sechs präsentiere ich Ergebnisse der CP-MD-Simulation von Ubisemichinonanion in 300 K wässriger Lösung (die Isoprenylgruppe wurde durch eine Ethylgruppe ersetzt). Wegen des Rechenaufwands ist die Simulationslänge kürzer als gewünscht; wir hoffen, dass wir in Zukunft die Simulation verlängern können.

Die Situation der H-Brückenbindungen ist für UQ^{•-} komplizierter als für BQ^{•-}. Die Anzahl an Wasserstoffbrücken zu Carbonyl-Sauerstoffatomen beträgt im Durchschnitt 4.6 - vergleichbar mit BQ^{•-}. Zum C₆-System werden aufgrund sterischer Hinderungen weniger H-Brückenbindungen ausgebildet (0.7 oder 0.5 - die Anzahl hängt von dem jeweiligen Erkennungskriterium ab). Hinzu kommen durchschnittlich 0.9 Wasserstoffbrücken der Methoxygruppen. Wegen sterischer Wechselwirkungen mit Nebengruppen sind H-Brückenbindungen zur Carbonylgruppe länger als die des BQ^{•-} - die RDF-Kurve ist breiter und ihr Maximum liegt bei 1.9-1.95 Å.

Anhand unserer Untersuchung zur Abhängigkeit der Wasserstoffbrückenbindungen von Winkelkriterien, können wir für UQ^{•-}, BQ^{•-} und neutrale BQ die Richtwirkung aller H-Bindungsarten graphisch darstellen. Dadurch lässt sich der Grad der Orientierung eines Protons verursacht durch eine Lewis-Säure ermitteln, so dass die jeweilige Richtwirkung der Lewis-Säure eine zusätzliche Methode zur Schätzung der Stärke einer H-Bindungsart darstellt. Wasserstoffbrücken zum Carbonylsauerstoffatom sind ungefähr gleich stark für UQ^{•-} und BQ^{•-} und etwas schwächer für neutrale BQ. H-Brücken zum Methoxysauerstoffatom des UQ^{•-} sind noch schwächer. "T-stacking" Wechselwirkungen sind im Fall des UQ^{•-} viel stärker als für BQ^{•-} (aufgrund einer

Verschiebung negativer Ladung von Methoxy-Sauerstoffatom zum C₆-Ring) und vergleichbar mit H-Brückenbindungen zu Methoxygruppen. Im neutralen BQ sind T-stacking Wechselwirkungen sehr schwach.

Die Anordnung der Methoxygruppen ist nicht ganz symmetrisch - eine Methoxygruppe (gegenüber einer Ethylgruppe) liegt meist senkrechter als die andere, vielleicht verursacht durch die kurzen Simulation. Wasserstoffbrücken zu einer MeO-Gruppe korrelieren mit deren Ausrichtung: die H-Brücken drehen die Methoxy-Gruppe so, dass ihre Me-Gruppe mehr in der Ebene (ausgerichtet nach der anderer MeO-Gruppe) liegt. Es gibt eine unerwartete und unverstandene Korrelation zwischen Wasserstoffbrücken zu Carbonylgruppen und der Orientierung der Methoxygruppe; es erfordert mehr Arbeit und eine längere Simulation, dies zu erklären. Die Ethylgruppe liegt senkrecht zur Ringebene.

In Kapitel sieben präsentiere ich *g*- und HFC-Tensordaten die auf die gleiche Art und Weise wie für BQ•⁻ aus der zuvor diskutierten MD Simulation des UQ•⁻s erhalten wurden. Der Einfluß von H-Brückenbindungen zu Carbonylsauerstoffatomen und dem π -System auf die *g*-Verschiebung sind dem Fall des BQ•⁻s ähnlich. Wasserstoffbrücken zur MeO-Gruppen weisen gegenwirkende Effekte auf, die vom Abstand zwischen wasserstoffverbrückenden Protonen und Carbonylsauerstoffen abhängig sind. Näher an der Carbonylgruppe dominiert die Wirkung des Lösungsmittelmoleküls auf die Carbonylgruppe. Wenn die H-Brückenbindung weiter entfernt ist, besitzt sie einen Effekt vergleichbar mit einer "T-stacked" Wechselwirkungen und Δg_x nimmt zu. Wie im Fall des BQ•⁻s, wird Δg_x um einige hundert ppm gegenüber dem Experiment überschätzt.

Die berechneten isotropen HFC-Konstanten stimmen im Vergleich zu BQ•⁻ mit den empirische Werten weniger gut überein (wobei die Simulationslänge bislang nicht ausreicht, um so genaue Aussagen treffen zu können). Wo experimentelle dipolare Daten verfügbar sind, ist die Übereinstimmung mit ihnen allgemein gut. Die Analyse der HFCs und Mulliken-Spindichten der Nebengruppen belegt signifikante Hyperkonjugation des SOMOs mit den Nebengruppenorbitalen. Diese führt zu größeren positiven Spindichten bei β -Kohlenstoffkernen als wir es nur anhand der Spinpolarisation erwarten würden - jedoch nur wenn die Gruppe senkrecht zur Ebene des Moleküls steht; wenn es in der Ebene liegt gibt es diese Effekte nicht. Für Lösungsmittelprotonen wird A_{iso} wieder unterschätzt und es gibt keinen Unterschied zwischen den berechneten A_{iso} -Werten für die verbrückenden H-Atome in HOH...BQ•⁻ und HOH...UQ•⁻, obwohl die experimentellen Werten sich um 0.8 MHz unterscheiden.

Abschließend kann zusammengefasst werden, dass *g*-Tensoren und Hyperfeinkopplungsdaten berechnet und analysiert worden sind, unter Berück-

sichtigung der Dynamik - nicht nur *ad hoc* sondern mit vollständiger Dynamik der MD. Es ist hervorzuheben, dass unsere Arbeit die erste ist, in der MD-Techniken für g -Tensorrechnungen angewendet wurden. Wir hoffen, unsere Simulationen von Ubisemichinon verlängern zu können und mehr Einblick in das System zu erhalten. Danach können wir die Techniken auf andere Semichinone oder größere Proteinsysteme anwenden. Unsere Ergebnisse in Kapitel vier zeigen, dass QM/MM vielleicht ein guter Ersatz für volles *ab initio* MD für diese Systeme ist. Weitere Vergleiche dazwischen wäre sinnvoll.

Wie in Kapitel eins diskutiert, wurde MD schon für HFC-Berechnungen für andere Radikale verwendet;⁵⁻⁷ aber dieser Forschungsbereich ist wegen des Rechenaufwands bislang verhältnismäßig klein. Seit Veröffentlichung unserer g -Tensoranalyse von BQ[•],^{66,67} (Kapital fünf), hat die Gruppe von V. Barone *et al.* diese Methode für g -Tensoren verbreitet, was die Nützlichkeit dieser MD-EPR Technik untermauert.

Bibliography

- [1] W. Pryor, K. Stone, L. Zang, and E. Bermúdez, *Chem. Res. Toxicol.* **11**, 441 (1998).
- [2] C. Brondino, M. Rivas, M. Romão, J. Moura, and I. Moura, *Act. Chem. Res.* **39**, 788 (2006).
- [3] M. Kaupp, M. Bühl, and V. Malkin (eds.), *Calculation of NMR and EPR Parameters* (Wiley VCH, 2005).
- [4] M. Pavone, P. Cimino, F. De Angelis, and V. Barone, *J. Am. Chem. Soc.* **128**, 4338 (2006).
- [5] H. Takase and O. Kikuchi, *Chem. Phys.* **181**, 57 (1994).
- [6] M. Igarashi, T. Ishibashi, and H. Tachikawa, *THEOCHEM* **594**, 61 (2002).
- [7] H. Tachikawa, M. Igarashi, and T. Ishibashi, *Chem. Phys. Lett.* **352**, 113 (2002).
- [8] R. Parr and W. Yang, *Density-Functional Theory of Atoms and Molecules* (Oxford University Press, New York, 1989).
- [9] W. Koch and M. Holthausen, *A Chemist's Guide to Density Functional Theory* (Wiley-VCH, Weinheim, 2002).
- [10] M. Allen and D. Tildesley, *Computer Simulation of Liquids* (Clarendon Press, Oxford, 1987).
- [11] D. Marx and J. Hutter, Ab initio molecular dynamics: Theory and implementation, in *NIC Series vol. 3: Modern Methods and Algorithms of Quantum Chemistry*, edited by J. Grotendorst, Forschungszentrum Jülich, 2000, Downloadable from <http://www.fz-juelich.de/nic-series/>.
- [12] P. Hohenberg and W. Kohn, *Phys. Rev.* **136**, 864 (1964).

- [13] T. Thomas, PCPS **23**, 542 (1927).
- [14] E. Fermi, Z. Phys. **48**, 73 (1928).
- [15] E. Teller, **34**, 627 (1962).
- [16] W. Kohn and L. Sham, Phys. Rev. **140**, A1133 (1965).
- [17] A. Becke, Phys. Rev. A **38**, 3098 (1988).
- [18] C. Lee, W. Yang, and R. Parr, Phys. Rev. B **37**, 785 (1988).
- [19] J. Slater, Phys. Rev. **81**, 385 (1951).
- [20] S. Vosko, L. Wilk, and M. Nusair, Can. J. Phys. **58**, 1200 (1980).
- [21] J. Perdew and Y. Wang, Phys. Rev. B **33**, 8822 (1986).
- [22] J. Perdew *et al.*, Phys. Rev. B **46**, 6671 (1992).
- [23] J. Perdew, S. Kurth, A. Zupan, and P. Blaha, Phys. Rev. Lett. **82**, 2544 (1999).
- [24] J. Perdew, S. Kurth, A. Zupan, and P. Blaha, Phys. Rev. Lett. **82**, 5179 (1999).
- [25] A. Becke, J. Comput. Phys. **98**, 5648 (1993).
- [26] A. Becke, J. Phys. Chem. **98**, 1372 (1993).
- [27] O. Malkina *et al.*, J. Am. Chem. Soc. **122**, 9206 (2000).
- [28] M. Kaupp *et al.*, J. Comput. Chem. **23**, 794 (2002).
- [29] B. Hess, C. Marian, U. Wahlgran, and O. Gropen, Chem. Phys. Lett. **251**, 365 (1996).
- [30] V. Barone, in *Recent Advances in Density Functional Methods*, edited by D. Chong, World Scientific Publishing, Singapore, 1995.
- [31] R. Car and M. Parrinello, Phys. Rev. Lett. **55**, 2471 (1985).
- [32] P. Tangney and S. Scandolo, J. Comput. Phys. **116**, 14 (2002).
- [33] H. Schlegel *et al.*, J. Comput. Phys. **114**, 9758 (2001).
- [34] S. Iyengar *et al.*, J. Comput. Phys. **115**, 10291 (2001).

- [35] H. Schlegel *et al.*, *J. Comput. Phys.* **117**, 8694 (2002).
- [36] P. Pulay, *Mol. Phys.* **17**, 197 (1969).
- [37] S. Boys and F. Bernandi, *Mol. Phys.* **19**, 553 (1970).
- [38] S. Nosé, *J. Comput. Phys.* **81**, 511 (1984).
- [39] W. Hoover, *Phys. Rev. A* **31**, 1695 (1985).
- [40] G. Martyna, M. Klein, and M. Tuckerman, *J. Comput. Phys.* **97**, 2635 (1992).
- [41] M. Kaupp, J. Asher, A. Arbuznikov, and A. Patrakov, *Phys. Chem. Chem. Phys.* **4**, 5458 (2002).
- [42] A. Bieniok and H.-B. Bürgi, *J. Phys. Chem.* **98**, 10735 (1994).
- [43] F. Feher, D. Newman, and J. Walzer, *J. Am. Chem. Soc.* **111**, 1741 (1989).
- [44] R. Laine, *J. Mater. Chem.* **15**, 3725 (2005).
- [45] R. Kannan, H. Salacinski, P. Butler, and A. Seifalian, *ACR* **38**, 879 (2005).
- [46] R. Sasamori, Y. Okaue, T. Isobe, and Y. Matsuda, *Science* **265**, 1691 (1994).
- [47] M. Päch and E. Stößer, *J. Phys. Chem. A* **101**, 8360 (1997).
- [48] A. Bassindale *et al.*, *Organometallics* **23**, 4400 (2004).
- [49] M. Frisch *et al.*, *Gaussian 98*, revision A.7, A.9.
- [50] W. Hehre, R. Ditchfield, and J. Pople, *J. Comput. Phys.* **56**, 2257 (1972).
- [51] P. Hariharan and J. Pople, *Theor. Chem. Acc.* **28**, 213 (1973).
- [52] M. Franci *et al.*, *J. Comput. Phys.* **77**, 3654 (1982).
- [53] A. Bergner, M. Dolg, W. Küchle, H. Stoll, and H. Preuss, *Mol. Phys.* **80**, 1431 (1993).
- [54] S. Huzinaga, editor, *Gaussian Basis Sets for Molecular Calculations* (Elsevier, New York, 1984).

- [55] D. Salahub *et al.*, Springer, New York, 1991.
- [56] A. St-Amant and D. Salahub, Chem. Phys. Lett. **169**, 387 (1990).
- [57] N. Godbout, D. Salahub, J. Andzelm, and E. Wimmer, Can. J. Chem. **70**, 560 (1992).
- [58] J. Perdew and Y. Wang, Phys. Rev. B **45**, 13244 (1992).
- [59] J. P. Perdew, in *Electronic Structure of Solids*, edited by P. Ziesche and H. Eischrig, Akademie Verlag, Berlin, 1991.
- [60] O. Malkina *et al.*, J. Am. Chem. Soc. **122**, 9206 (2000).
- [61] V. Malkin *et al.*, Mag-respect, v. 1.1, 2003.
- [62] B. Gross, H. Dilger, R. Scheuermann, M. Päch, and E. Roduner, J. Phys. Chem. A **105**, 10012 (2001).
- [63] W. Kutzelnigg, U. Fleischer, and M. Schindler, in *NMR - Basic Principles and Progress* Vol. 23, p. 165, Springer, Heidelberg, 1990.
- [64] M. Mattori, K. Mogi, Y. Sakai, and T. Isobe, J. Phys. Chem. A **104**, 10868 (2000).
- [65] P. Kusch, Phys. Rev. **100**, 1188 (1955).
- [66] J. Asher, N. Doltsinis, and M. Kaupp, J. Am. Chem. Soc. **126**, 9854 (2004).
- [67] J. Asher, N. Doltsinis, and M. Kaupp, Mag. Res. Chem. **43**, S237 (2005).
- [68] S. Patai, *Chemistry of Quinoid Compounds* (Interscience, New York, 1974).
- [69] B. Trumpower, editor, *Function of Quinones in Energy Conserving Systems* (Academic Press, New York, 1982).
- [70] R. Morton, editor, *Biochemistry of Quinones* (Academic Press, New York, 1965).
- [71] H. Levanon and K. Möbius, Annu. Rev. Biophys. Biomol. Struct. **26**, 495 (1997).
- [72] T. Prisner, M. Rohrer, and F. MacMillan, Annu. Rev. Phys. Chem. **52**, 279 (2001).

- [73] J. Hutter *et al.*, CPMD 3.5.2.
- [74] N. Trouiller and J. Martins, Phys. Rev. B **43**, 1993 (1991).
- [75] M. Frisch *et al.*, Gaussian 03, revision c.02.
- [76] A. Schäfer, C. Huber, and R. Ahlrichs, J. Comput. Phys. **100**, 5829 (1994).
- [77] M. Kaupp, Biochem. **41**, 2895 (2002).
- [78] T. Manojkumar, H. Choi, P. Tarakeshwar, and K. Kim, J. Comput. Phys. **118**, 8681 (2003).
- [79] S. Sinnecker, E. Reijerse, F. Nesse, and W. Lubitz, J. Am. Chem. Soc. **126**, 3280 (2004).
- [80] M. Flores, R. Isaacson, R. Calv, G. Feher, and W. Lubitz, Chem. Phys. **294**, 401 (2003).
- [81] J. A. Nilsson, A. Lyubartsev, L. A. Eriksson, and A. Laaksonen, Mol. Phys. **99**, 1795 (2001).
- [82] M. Nonella, G. Mathias, and P. Tavan, J. Phys. Chem. B **107**, 8638 (2003).
- [83] P. O'Malley, J. Phys. Chem. A **101**, 6334 (1997).
- [84] D. Chipman, J. Phys. Chem. A **104**, 11816 (2000).
- [85] M. Kaupp, C. Remenyi, J. Vaara, O. Malkina, and V. Malkin, J. Am. Chem. Soc. **123**, 2709 (2002).
- [86] S. Mattar, J. Phys. Chem. B **108**, 9449 (2004).
- [87] K. Raymond, A. Grafton, and R. A. Wheeler, J. Phys. Chem. B **101**, 623 (1997).
- [88] X. Shao and T. Kitagawa, J. Raman Spectrosc. **29**, 773 (1998).
- [89] M. Knüpling, J. Törring, and S. Un, Chem. Phys. **219**, 291 (1997).
- [90] I. Ciofini, R. Reviakine, A. Arbuznikov, and M. Kaupp, Theor. Chem. Acc. **111**, 132 (2004).
- [91] R. Hester and K. Williams, J. Chem. Soc. Faraday Trans. **78**, 573 (1982).

- [92] J. Asher and M. Kaupp, *ChemPhysChem*. **8**, 69 (2007).
- [93] S. Weissman, J. Townsend, D. Paul, and G. Pake, *J. Comput. Phys.* **21**, 2227 (1953).
- [94] T. Chu, G. Pake, D. Paul, J. Townsend, and S. Weissman, *J. Phys. Chem.* **57**, 504 (1953).
- [95] H. Jarrett and G. Sloan, *J. Comput. Phys.* **22**, 1783 (1954).
- [96] B. Venkataraman and G. Fraenkel, *J. Am. Chem. Soc.* **77**, 2707 (1955).
- [97] B. Venkataraman and G. Fraenkel, *J. Comput. Phys.* **23**, 588 (1955).
- [98] B. Venkataraman and G. Fraenkel, *J. Comput. Phys.* **24**, 737 (1956).
- [99] R. Hoskins, *J. Comput. Phys.* **23**, 1975 (1955).
- [100] H. McConnell, *J. Comput. Phys.* **24**, 764 (1956).
- [101] R. Bersohn, *J. Comput. Phys.* **24**, 1066 (1956).
- [102] H. Strauss and G. Fraenkel, *J. Comput. Phys.* **35**, 1738 (1961).
- [103] M. Das and B. Venkataraman, *J. Comput. Phys.* **35**, 2262 (1961).
- [104] J. Gendell, J. Freed, and G. Fraenkel, *J. Comput. Phys.* **37**, 2832 (1962).
- [105] E. Stone and A. Maki, *J. Am. Chem. Soc.* **87**, 454 (1965).
- [106] M. Das and G. Fraenkel, *J. Comput. Phys.* **42**, 1350 (1965).
- [107] J. W.M. Gulick and D. Geske, *J. Am. Chem. Soc.* **88**, 4119 (1966).
- [108] B. Hales, *J. Am. Chem. Soc.* **97**, 5993 (1975).
- [109] A. Stone, *Mol. Phys. A.* **6**, 509 (1963).
- [110] B. Prabhananda, *J. Comput. Phys.* **79**, 5752 (1983).
- [111] R. Angstl, *Chem. Phys.* **132** (1989).
- [112] J. Törring, S. Un, M. Knüpling, M. Plato, and K. Möbius, *J. Comput. Phys.* **107**, 3905 (3905).
- [113] F. Neese, *J. Comput. Phys.* **115**, 11080 (2001).

- [114] K. Neyman, D. Ganyushin, A. Matveev, and V. Nasluzov, *J. Phys. Chem. A* **106**, 5022 (2002).
- [115] M. Engström, O. Vahtras, and H. Ågren, *Chem. Phys.* **243**, 263 (1999).
- [116] K. Neyman, D. Ganyushin, Ž. Rinkevičius, and N. Rösch, *Int. J. Quant. Chem.* **90**, 1404 (2002).
- [117] A. Stone, *Proc. R. Soc. A.* **271**, 424 (1963).
- [118] S. Koseki, M. Schmidt, and M. Gordon, *J. Phys. Chem.* **96**, 10768 (1992).
- [119] S. Koseki, M. Gordon, M. Schmidt, and N. Matsunaga, *J. Phys. Chem.* **99**, 12764 (1995).
- [120] S. Koseki, M. Schmidt, and M. Gordon, *J. Phys. Chem. A* **102**, 10430 (1998).
- [121] S. Kacprzak, M. Kaupp, and F. MacMillan, *J. Am. Chem. Soc.* **128**, 5659 (2006).
- [122] B. Epel, J. Niklas, S. Sinnecker, H. Zimmermann, and W. Lubitz, *J. Phys. Chem. B* **110**, 11549 (2006).
- [123] O. Burghaus *et al.*, *J. Phys. Chem.* **97**, 7639 (1993).
- [124] S. Fiedler and J. Eloranta, *Mag. Res. Chem.* **43**, 231 (2005).
- [125] J. Cape, M. Bowman, and D. Kramer, *J. Am. Chem. Soc.* **127**, 4208 (2005).
- [126] R. Ahlrichs, M. Bär, M. Häser, H. Horn, and C. Kölmel, *Chem. Phys. Lett.* **162**, 165 (1989).
- [127] R. Ahlrichs and M. von Arnim, in *Methods and Techniques in Computational Chemistry: METECC-95*, edited by E. Clementi and G. Corongiu, chap. 13, p. 509, Club Européen MOTTECC, 1995.
- [128] K. Eichkorn, O. Treutler, H. Öhm, M. Häser, and R. Ahlrichs, *Chem. Phys. Lett.* **242** (1995).
- [129] A. Klamt and G. Schüürmann, *J. Chem. Soc. Perkin Trans.* **2**, 799 (1993).
- [130] M. Engström *et al.*, *J. Phys. Chem. A* **104**, 5149 (2000).

- [131] P. O'Malley, *J. Phys. Chem. A* **101**, 9813 (1997).
- [132] M. Langgård and J. Spanget-Larsen, *THEOCHEM* **431**, 173 (1998).
- [133] F. MacMillan, F. Lenzian, and W. Lubitz, *Mag. Res. Chem.* **33**, S81 (1995).
- [134] P. O'Malley, *Chem. Phys. Lett.* **291**, 367 (1998).
- [135] O. Burghaus, *Thesis* (Freie Universität Berlin (Germany), 1991).
- [136] F. Himo, G. Babcock, and L. Eriksson, *J. Phys. Chem. A* **103**, 3745 (1999).
- [137] M. Nonella, *J. Phys. Chem. B* **102**, 4217 (1998).
- [138] M. Nonella, G. Mathias, M. Eichinger, and P. Tavan, *J. Phys. Chem. B* **107**, 316 (2003).
- [139] A. Grafton and R. Wheeler, *J. Phys. Chem. B* **103**, 5380 (1999).
- [140] P. J. O'Malley, *Chem. Phys. Lett.* **285**, 99 (1998).
- [141] K. Möbius, *THEOCHEM* **632**, 287 (2003).
- [142] J. van den Brink *et al.*, *FEBS Lett.* **353**, 273 (1994).
- [143] T. Kropacheva, W. van Liemt, J. Raap, J. Lugtenburg, and A. Hoff, *J. Phys. Chem.* **100**, 10433 (1996).
- [144] J. Pederson, editor, *Handbook of EPR Spectra from Quinones and Quinols* (CRC Press, Boca Raton, Florida, 1985).
- [145] O. Nimz, F. Lenzian, C. Boullais, and W. Lubitz, *Appl. Magn. Res.* **14**, 255 (1998).
- [146] R. Isaacson *et al.*, in *The reaction centre of photosynthetic bacteria, structure and dynamics*, edited by M.-E. Michael-Beyerle, p. 353, Springer-Verlag, Berlin, 1996.
- [147] R. Samoilova *et al.*, *J. Chem. Soc. Perkin Trans.* **2**, 2063 (1995).
- [148] P. Lehtovuori and H. Joela, *J. Mag. Res.* **145**, 319 (2000).

Curriculum Vitae

James R. Asher

Born 07/07/1979, Bath, Avon, UK.

University studies

- August 2001 - December 2006: Doctoral studies and research at the Julius-Maximilians University of Würzburg. Qualifications gained: Doctor Rerum Naturalem.
- October 1997 - July 2001: Master degree studies in Chemistry at Durham University, Durham, UK. Qualifications gained: MSci (First-class honours).

College education

- September 1995 - July 1997: A (Advanced)-level studies at Lakeview College, Nottingham, UK. Qualifications gained: A-levels (grade A) in Chemistry, Physics, Mathematics and German.

High school education

- September 1990 - July 1995: Secondary education at Alderman White Comprehensive School, Beeston/Chilwell, Nottinghamshire, UK. Qualifications gained: GCSEs (General Certificate of Secondary Education) in: Science, Mathematics, German (A*); English, English Literature, Geography (A); Music, Art (C).

Language skills

- English (native tongue)

- German (conversational level)

Technical skills

- Programming skills in Fortran 77 and Bash shells scripting (used to create own utilities and basic data analysis tools)
- Word processing using MS Word or LaTeX (thesis written in the latter)
- Image processing using Adobe Photoshop
- Able to use the quantum chemical packages Gaussian, Turbomole, CPMD

List of Publications

- M. Kaupp, J. Asher, A. Arbouznikov and A. Patrakov, Phys. Chem. Chem. Phys. **4**, 5458 (2002)
- J.R. Asher, N.L. Doltsinis and M. Kaupp, J. Am. Chem. Soc. **126**, 9854 (2004)
- J.R. Asher, N.L. Doltsinis and M. Kaupp, Mag. Res. Chem. **43**, S237 (2005)
- J.R. Asher and M. Kaupp, ChemPhysChem. **8**, 69 (2007)
- J.R. Asher, Doctoral Thesis (Würzburg, 2006)